

**University of São Paulo
Polytechnic School
Graduate Program in Civil Engineering**

Vítor Oliveira Santos Vizini

**New methods for determining strength and fracture toughness of rock and
concrete**

São Paulo
2021

Vítor Oliveira Santos Vizini

**New methods for determining strength and fracture toughness of rock and
concrete**

Corrected version

(Original version is in the unit that hosts the Graduate Program)

Dissertation presented to the Polytechnic
School of University of São Paulo to obtain
the degree of Master of Science.

Concentration area: Geotechnical Engineering

Advisor: Prof. Dr. Marcos Massao Futai

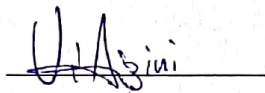
São Paulo
2021

Autorizo a reprodução e divulgação total ou parcial deste trabalho, por qualquer meio convencional ou eletrônico, para fins de estudo e pesquisa, desde que citada a fonte.

Este exemplar foi revisado e corrigido em relação à versão original, sob responsabilidade única do autor e com a anuência de seu orientador.

São Paulo, 4 de janeiro de 2021

Assinatura do autor:



Assinatura do orientador:



Catálogo-na-publicação

Vizini, Vitor

New methods for determining strength and fracture toughness of rock and concrete / V. Vizini -- versão corr. -- São Paulo, 2021.

99 p.

Dissertação (Mestrado) - Escola Politécnica da Universidade de São Paulo. Departamento de Engenharia de Estruturas e Geotécnica.

1.Ensaio de rochas 2.Ensaio de concreto 3.Ensaio de cisalhamento
4.Ensaio de tração 5.Fratura dos materiais I.Universidade de São Paulo. Escola Politécnica. Departamento de Engenharia de Estruturas e Geotécnica II.t.

AGRADECIMENTOS

Agradeço a Deus por tudo que tem preparado em minha vida.

Agradeço ao Prof. Dr. Marcos Massao Futai, pela oportunidade dada a mim, desde a iniciação científica e até agora no mestrado, pela orientação, suporte e confiança.

Agradeço aos Professores que participaram da banca de qualificação (Prof. Dr. José Luíz Antunes de Oliveira e Sousa e Prof. Dr. Túlio Nogueira Bittencourt) e da banca de defesa (Prof. Dr. Eurípedes do Amaral Vargas Júnior e Prof. Dr. Sérgio Persival Baroncini Proença), pela contribuição e disponibilidade.

Agradeço ao Dr. Pedro Pazzoto Cacciari e ao MSc. André Augusto Cepeda, pelas ajudas prestadas.

Agradeço à Prof.^a Maria Cristina Vidal Borba, pela revisão e correção de inglês desta dissertação.

Agradeço à minha noiva (Beatriz) e a minha família (Leonel, Elisabeth e Carina), por todo o apoio.

Agradeço aos meus colegas de pós-graduação, funcionários e Professores, pelas ajudas prestadas.

Agradeço à Escola Politécnica da Universidade de São Paulo pelo curso de Mestrado.

Agradeço à Coordenação de Aperfeiçoamento de Pessoal de Nível Superior (CAPES) pela bolsa de estudo.

Tudo fez formoso em seu tempo:
também pôs o mundo no coração
deles, sem que o homem possa
descobrir a obra que Deus fez
desde o princípio até o fim.

Eclesiastes 3.11.

ABSTRACT

VIZINI, V. O. S. New methods for determining strength and fracture toughness of rock and concrete. 2020. 99 p. Dissertation (Master of Science). Polytechnic School, University of São Paulo, São Paulo, Brazil, 2021.

This research addresses two new test methods for determining strength and fracture toughness of rock and concrete: Modified Direct Shear Test (MDST) and Pull-Off Test (POT). The MDST proposes a modification in the geometry of the Direct Shear Test (DST) to improve the boundary conditions of the test, avoiding undesirable tensile fractures and promoting a single horizontal shear fracture. The MDST basically consists of adding two inclined notches in the test specimen of the DST. An ideal geometry was proposed based on numerical analysis and experimental tests on concrete. Experimental tests on homogeneous rocks, for low normal stresses, were performed with the ideal geometry, and it was obtained for most of the cases studied: i) a single horizontal shear fracture (without tensile fractures); ii) striated surface appearance in the most sheared area and iii) force versus displacement curve approximately linear with abrupt rupture. A summary and guidance for performing and verifying the MDST was proposed. Through the proposed modification a better shear strength test method for rock and concrete was achieved. Moreover, the MDST was proposed for determining mode II fracture toughness (K_{IIc}) in function of confining pressure, of homogeneous rock and concrete. The study was carried out by numerical analysis and it allowed concluding that: i) MDST is suitable for K_{IIc} determination, since mode II prevails in the test; ii) the horizontal fracture pattern is due to shear; iii) the confining pressure must be determined at the fracture tip ($\sigma_{n(tip)}$) and iv) two equations were proposed for determining K_{IIc} in function of $\sigma_{n(tip)}$. A practical example was provided and K_{IIc} envelopes were obtained for some rocks and concrete. The POT fracture mechanism under different test conditions was studied using eXtended Finite Element Method to assess the factors influencing the tensile strength of homogeneous rock. The numerical results were validated with experimental data and a good agreement was obtained. An ideal test geometry was proposed (the depth and width of the partial core were equal to 2.5 cm and 0.4 cm, respectively). The POT can overestimate or underestimate the tensile strength of the rock, depending on the cohesive fracture energy and a correction equation was proposed. Moreover, the POT was proposed as a new method for determining mode I fracture toughness (K_{Ic}) of homogeneous rock and concrete in field application. A ratio between the POT dimensions was proposed to meet the requirements of Linear Elastic Fracture Mechanics and literature recommendations. The study was carried out by numerical analysis and it allowed concluding that the POT is suitable for K_{Ic} testing, since mode I prevails in the test, and an equation was proposed for determining K_{Ic} via POT. A practical example of the method application was provided and K_{Ic} was determined for some homogeneous rocks. A similar result was achieved between POT and Semi-Circular Bend test, indicating the first validation and correlation of the method.

Key words: Tensile strength. Shear strength. Mode I fracture toughness. Mode II fracture toughness. Pull-Off Test. Modified Direct Shear Test. Rock. Concrete.

RESUMO

VIZINI, V. O. S. Novos métodos para determinação de resistência e tenacidade à fratura de rocha e concreto. 2020. 99 p. Dissertação (Mestre em Ciências). Escola Politécnica, Universidade de São Paulo, São Paulo, Brasil, 2021.

Esta pesquisa aborda dois novos métodos experimentais para determinação de resistência e tenacidade à fratura de rocha e concreto: Ensaio de Cisalhamento Direto Modificado (ECDM) e Ensaio de Arrancamento (EA). O ECDM propõe uma modificação na geometria do Ensaio de Cisalhamento Direto (ECD) para melhorar as condições de contorno do ensaio, evitando indesejáveis fraturas de tração e promovendo uma única fratura de cisalhamento. O ECDM basicamente consiste em adicionar dois entalhes inclinados no corpo de prova do ECD. Uma geometria ideal foi proposta baseando-se em análise numérica e experimental em concreto. Testes experimentais em rochas homogêneas, para tensões normais baixas, foram realizados com a geometria ideal e foi obtido para a maioria dos casos estudados: i) uma única fratura de cisalhamento horizontal (sem fraturas por tração); ii) superfície com aparência estriada na maioria da área cisalhada e iii) curva força versus deslocamento aproximadamente linear com ruptura abrupta. Além disto, o ECDM foi proposto para se determinar tenacidade à fratura no modo II (K_{IIc}), em função da pressão confinante, de rocha visualmente homogênea e concreto. O estudo foi conduzido por meio de análise numérica e permitiu concluir que: i) o MDST é adequado para teste de K_{IIc} , visto que o modo II prevalece no ensaio; ii) o padrão de fratura horizontal é devido ao cisalhamento; iii) a pressão confinante deve ser determinada na ponta da fratura (σ_n (ponta)) e iv) duas equações foram propostas para determinar K_{IIc} em função da σ_n (ponta). Um exemplo prático foi fornecido e envoltórias de K_{IIc} foram obtidas para algumas rochas e um concreto. O mecanismo de fratura no EA foi estudado para diferentes condições de teste usando o Método dos Elementos Finitos Extendidos, para avaliar os fatores que influenciam a resistência à tração em rochas homogêneas. Os resultados numéricos foram validados com dados experimentais e uma boa aproximação foi obtida. Uma geometria ideal foi proposta (a profundidade e a largura do corte parcial foram iguais a 2,5 cm e 0,4 cm, respectivamente). O EA pode superestimar ou subestimar a resistência à tração da rocha, dependendo da energia de fratura coesiva e uma equação de correção foi proposta. Além disto, o EA foi proposto para se determinar tenacidade à fratura no modo I (K_{Ic}) de rocha homogênea e concreto, com aplicação em campo. Uma razão entre as dimensões do EA foi proposta, para atender aos requerimentos da Mecânica da Fratura Linear Elástica e às recomendações da literatura. O estudo foi conduzido por meio de análise numérica e permitiu concluir que o EA é adequado para teste de K_{Ic} , visto que o modo I prevalece no ensaio, e uma equação foi proposta para se determinar K_{Ic} via EA. Um exemplo prático de aplicação do método foi fornecido e K_{Ic} foi determinado para algumas rochas homogêneas. Resultados similares foram obtidos entre o EA com o Ensaio Semi-Circular de Flexão, indicando uma primeira validação e correlação do método.

Palavras chaves: Resistência à tração. Resistência ao cisalhamento. Tenacidade à Fratura no modo I. Tenacidade à Fratura no modo II. Ensaio de Arrancamento. Ensaio de Cisalhamento Direto Modificado. Rocha. Concreto.

CONTENTS

1	INTRODUCTION	11
1.1	OBJECTIVES	12
1.1.1	GENERAL OBJECTIVE	12
1.1.2	SPECIFIC OBJECTIVES	12
1.2	STRUCTURE OF THE DISSERTATION	12
2	MODIFIED DIRECT SHEAR TEST FOR DETERMINING SHEAR STRENGTH OF ROCK AND CONCRETE	15
2.1	INTRODUCTION	15
2.2	MODIFIED DIRECT SHEAR TEST	18
2.3	IDEAL GEOMETRY OF THE MDST	20
2.3.1	STRESS ANALYSIS OF MODELS	20
2.3.2	EXPERIMENTAL TESTS OF MODELS IN CONCRETE.....	24
2.4	EXPERIMENTAL TESTS ON ROCKS USING IDEAL GEOMETRY	30
2.5	METHOD SUMMARY AND GUIDANCE	35
2.6	CONCLUSION	37
3	MODE II FRACTURE TOUGHNESS DETERMINATION OF ROCK AND CONCRETE VIA MODIFIED DIRECT SHEAR TEST	39
3.1	INTRODUCTION	39
3.2	MDST GEOMETRY	43
3.3	NUMERICAL METHODS AND MODEL	44
3.3.1	NUMERICAL METHOD	44
3.3.2	NUMERICAL MODEL.....	46
3.3.3	SIFS COMPUTATION TECHNIQUE	47
3.4	FRACTURE ANALYSIS OF THE MDST	49
3.5	MECHANICAL PROPERTY PARAMETRIC STUDY.....	50
3.6	A SIMPLE WAY FOR K_{IIc} DETERMINATION	51
3.7	PRACTICAL EXAMPLE AND VALIDATION OF EQUATIONS	54
3.8	CONCLUSION	57
4	NUMERICAL ASSESSMENT OF FACTORS INFLUENCING THE TENSILE STRENGTH OF ROCKS VIA PULL-OFF TEST	59
4.1	INTRODUCTION	59
4.2	POT NUMERICAL MODEL AND METHOD.....	61

4.2.1	XFEM AND FRACTURE INITIATION AND PROPAGATION CRITERIA	61
4.2.2	GEOMETRY, MESH AND TYPE OF ANALYSIS.....	64
4.3	MECHANICAL PROPERTIES OF MATERIALS.....	64
4.4	GEOMETRICAL PARAMETRIC STUDY	67
4.5	MECHANICAL PROPERTIES PARAMETRIC STUDY	70
4.6	PRACTICAL EXAMPLE.....	72
4.7	CONCLUSIONS	73
5	MODE I FRACTURE TOUGHNESS DETERMINATION OF ROCK AND CONCRETE VIA PULL-OFF TEST	75
5.1	INTRODUCTION.....	75
5.2	NUMERICAL METHODS, MODEL AND SIFS COMPUTATION TECHNIQUE	78
5.2.1	NUMERICAL METHOD	78
5.2.2	NUMERICAL MODEL	80
5.2.3	SIFS COMPUTATION TECHNIQUE	81
5.2.4	VALIDATION OF THE NUMERICAL MODEL AND METHODS	82
5.3	POT GEOMETRY	84
5.4	FRACTURE ANALYSIS OF THE POT.....	85
5.5	MECHANICAL PROPERTY PARAMETRIC STUDY.....	87
5.6	A SIMPLE WAY FOR K_{IC} DETERMINATION VIA POT	87
5.7	PRACTICAL EXAMPLE.....	88
5.8	COMPARISON BETWEEN POT AND SCB.....	90
5.9	CONCLUSION	91
6	GENERAL CONCLUSION OF THIS DISSERTATION	92
	REFERENCES	93

1 INTRODUCTION

The determination of resistant properties of the materials is an essential task in engineering to ensure safety and to prevent hazards, material damage or interruption of activities. Geotechnical works, such as tunnels, gallery, shafts, dams and other foundations, often involve rock and concrete materials. Its failure mechanism is characterized by brittle or quasibrittle fractures, causing a rapid and abrupt rupture.

The classical approach to determining the failure of the materials in geotechnics is the strength-of-material approach. It is characterized by two components: tensile and shear strength. These components are determined by the average stress at the rupture and consider a homogeneous media. Another approach that is increasingly being used, which considers a previous fractured media, is the Linear Elastic Fracture Mechanics. Fracture toughness is the unique parameter to measure the resistance. It is separately in three particular modes of loading at the fracture tip: I (tensile), II (shear-sliding) and III (shear-tearing) (ATKINSON, 1987, WHITTAKER; SINGH; SUN, 1992).

This research addresses two new experimental test methods for determining strength and fracture toughness of rock and concrete: Modified Direct Shear Test (MDST) and Pull-Off Test (POT).

The Direct Shear Test (DST) is a shear strength test method widely used in rock mechanics (ASTM, 2016). Despite widely used, DST has a complex stress state that can lead a complex fracture mode, involving shear fractures and undesirable tensile fractures (CHO; MARTIN; SEGO, 2008, BEWICK et al., 2014, DIRGELIENË; SKUODIS; GRIGUSEVIČIUS, 2017). The MDST was studied in this work to improve the boundary conditions of the DST, to reduce or even to eliminate undesirable tensile fractures, resulting in a better shear strength test method. Moreover, the MDST is proposed for determining mode II fracture toughness (K_{IIc}), because there are few methods in the literature for determine K_{IIc} in function of the confining pressure.

The POT is a tensile strength testing method that is widely used in concrete and it was recently applied to rock mechanics (WENG et al., 2018, CACCIARI; FUTAI, 2018). The POT can be easily performed in both the field and the laboratory, but the major advantage is the possibility of in field execution. Due to the boundary conditions of the POT, its results are not the same as the Direct Tensile Test (CACCIARI; FUTAI, 2018). Only elastic linear

analyses of the POT have been reported in the literature and no theoretical studies have investigated the POT fracture mechanism or the effect of the boundary conditions on the tensile strength determination. In this study, POT fracture mechanism is analyzed under different test conditions, through the eXtended Finite Element Method (XFEM), to assess the factors influencing the tensile strength of homogeneous rock. Moreover, the POT is proposed for determining mode I fracture toughness (K_{Ic}), because the literature presents few test methods for K_{Ic} determination of rock and concrete in field.

1.1 OBJECTIVES

1.1.1 GENERAL OBJECTIVE

The main objective of this dissertation is to propose or contribute to the proposal of two experimental test methods for determining strength (tensile and shear) and fracture toughness (mode I and II) of rock and concrete.

1.1.2 SPECIFIC OBJECTIVES

The specific objectives of this dissertation are:

- a) to improve the DST boundary conditions (resulting in the MDST) to reduce or even to eliminate the undesirable tensile fractures and promoting a single horizontal shear fracture in homogeneous materials;
- b) to propose the MDST as a new method for determining mode II fracture toughness in function of the confining pressure in homogeneous rock and concrete;
- c) to analyze the POT fracture mechanism under different test conditions, to assess the factors influencing the tensile strength of homogeneous rock and concrete;
- d) to propose the POT as a new method for determining mode I fracture toughness in homogeneous rock and concrete.

1.2 STRUCTURE OF THE DISSERTATION

This dissertation was structured in the form of papers. Each paper generated has an introduction, literature review, justification, materials and methods, discussion and conclusion. The papers are listed below:

Chapter 2 - Modified Direct Shear Test for determining shear strength of rock and concrete.

Chapter 3 - Mode II fracture toughness determination of rock and concrete via Modified Direct Shear Test.

Chapter 4 - Numerical assessment of factors influencing the tensile strength of rocks via Pull-Off Test.

Chapter 5 - Mode I fracture toughness determination of rock and concrete via Pull-Off Test.

Finally, a general conclusion of the dissertation is shown in Chapter 6.

2 MODIFIED DIRECT SHEAR TEST FOR DETERMINING SHEAR STRENGTH OF ROCK AND CONCRETE

Abstract: This paper proposes a modification in the Direct Shear Test (DST) to improve the boundary conditions of the test, avoiding undesirable tensile fractures and promoting a single horizontal shear fracture. The Modified Direct Shear Test (MDST) basically consists of adding two inclined notches in the test specimen of the DST. An ideal geometry was proposed based on numerical analysis and experimental tests on concrete. Experimental tests on homogeneous rocks, for low normal stresses, were performed with the ideal geometry, and it was obtained for most of the cases studied: i) a single horizontal shear fracture (without tensile fractures); ii) striated surface appearance in the most sheared area and iii) force versus displacement curve approximately linear with abrupt rupture. A summary and guidance for performing and verifying the MDST were provided. Through the proposed modification, a better shear strength test method for rock and concrete was achieved.

Keywords: Modified Direct Shear Test. Shear strength. Rock. Concrete.

This chapter has been accepted for publication: VIZINI, V. O. S.; FUTAI, M. M. Modified Direct Shear Test for determining shear strength of rock and concrete. **Geotechnical Testing Journal**.

2.1 INTRODUCTION

Rock and concrete failure are usually predicted in geotechnical and structural engineering works. The classical approach to determine the failure of the materials is the strength-of-material approach, where the materials fail when the tensile or shear stress reaches the tensile or shear strength. Many civil engineering works, such as tunnels, shafts, galleries, dams, foundations and others, are solicited by compression stresses exerted by the weight of the rock mass or the structure itself, causing shear failure (MELIN, 1986; LAWN, 1993; BOBET; EINSTEIN, 1998; BROBERG, 1999) and the determination of shear strength in function of the confining pressure (normal stress) becomes extremely important. There are four test methods for determining shear strength in function of the confining pressure for rock and concrete: Triaxial Compression Test (ISRM, 1983), Direct Shear Test (DST) (ASTM, 2016), Compressive-Shear Test (RAO et al., 1999) and Punch-Through Shear with Confining Pressure Test (PTS-CP) (BACKERS; STEPHANSSON; RYBACKI, 2002; LEE, 2007).

The DST is widely used in geotechnical engineering for three main reasons: i) simplicity of execution; ii) normal and shear stress can be applied independently and iii) it can be performed for both intact materials strength and sliding friction tests, in homogeneous materials or with planes of weakness, including natural or artificial discontinuities (ASTM, 2016). Although DST is widely used, it has a complex stress state, that it can lead a complex fracture mode in homogeneous materials, involving tensile (mode I) and shear (mode II)

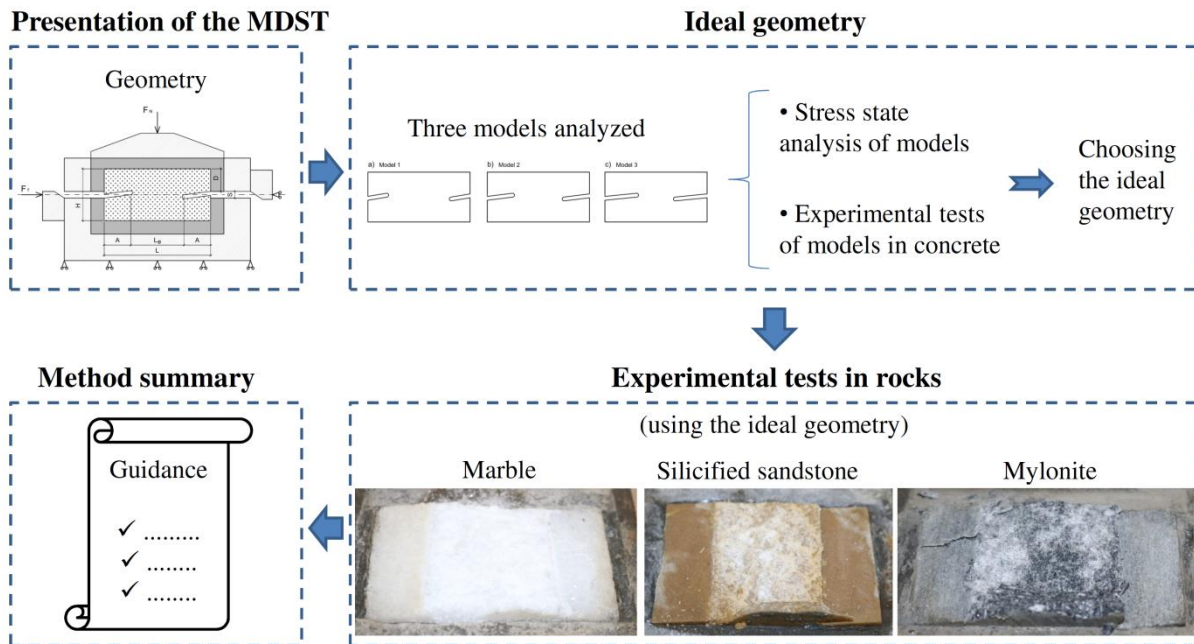
fractures, as observed by many authors, such as LAJTAI (1969); CRESSWELL; BARTON (2003); WONG et al. (2007); CHO; MARTIN; SEGO (2008); BEWICK et al. (2014); DIRGELIENĖ; SKUODIS; GRIGUSEVIČIUS (2017) and GONG et al. (2020). Materials with planes of weakness or discontinuities are less affected, because the fracture mode is highly dependent on those planes of weakness or discontinuities.

Based on the aforementioned authors, the typical fracture development process of homogeneous rock and concrete tested in the DST is as follows: a) for low average normal stresses (< 30 MPa, approximately), the first fractures develop in the test specimen (TS) by tensile (known as wing), starting at the upper or lower right extremity and upper left extremity, such as schematically represented in figure 2.1a. Sequentially, a tensile fracture (known as en echelon) develops in the center region of the TS. The final fractures occur linking the en echelon fracture to the ends of the TS, by shear and b) for high average normal stresses (> 30 MPa, approximately), the first fracture develops in the test are by tensile (wing), starting at the upper right extremity (fig. 2.1b). Sequentially, some tensile fractures (en echelon) develop in the center region of the TS. The final fractures occur linking the en echelons fractures to the ends of the TS, by shear. In short, for low normal stress, the specimen ruptures predominantly by tensile and, for higher normal stresses, the specimen ruptures progressively by shear (predominantly).

The formation of tensile fractures is undesirable in DST, since it is a shear strength test, but due to its geometry, it is inevitable (mainly at low normal stresses). A possible solution to solve the problem is to improve the boundary conditions of the test, changing its geometry. We here propose a modification in the DST to improve the boundary conditions of the test to avoid undesirable tensile fractures and promoting a single horizontal shear fracture, which is the ideal fracture pattern in shear tests, according to BAŽANT; PFEIFFER (1986), ENGELDER (1987) and PETIT (1988). The new method is named as Modified Direct Shear Test (MDST).

The MDST was presented in the next section. An ideal geometry study was carried out using numerical analysis and mainly by experimental tests on concrete. Experimental tests on homogeneous rocks (most problematic case), for low normal stresses (where tensile fractures are more pronounced), were performed with the ideal geometry, to demonstrate the effectiveness of the proposed test. Figure 2.2 illustrates the structure and overview of the paper.

Fig. 2.2. Structure and overview of the paper.



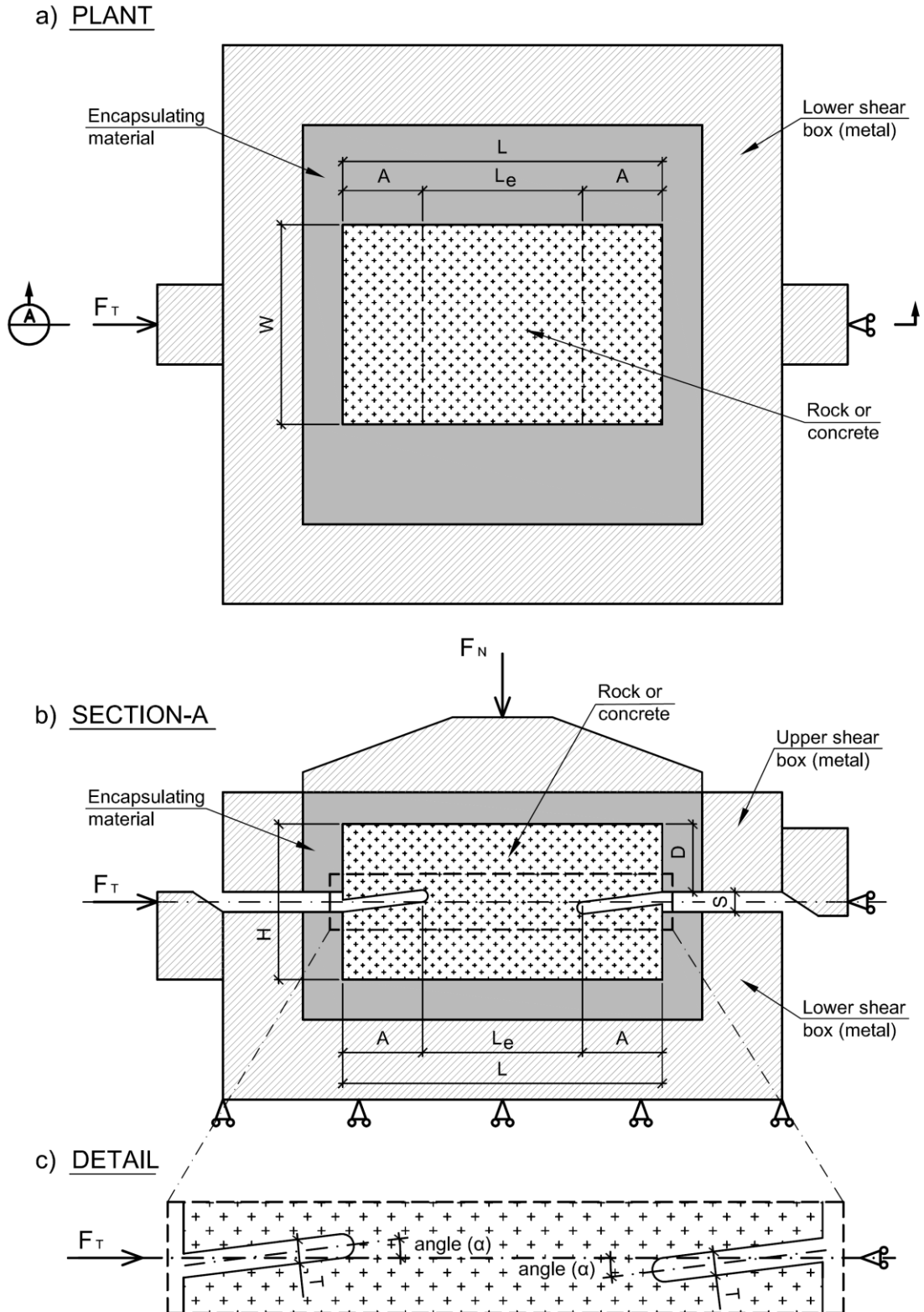
2.2 MODIFIED DIRECT SHEAR TEST

The MDST basically consists in adding two inclined notches in the TS of the DST, as shown in Fig. 2.3. Due to the notches being inclined, there will be no difference in level between the place where the fracture probably initiates and ends, providing a horizontal fracture (parallel to the tangential force (F_T) and normal to the normal force (F_N)).

MDST testing procedures are similar to DST procedures, as reported by ASTM D5607-16 (*Standard Test Method for Performing Laboratory Direct Shear Strength Tests of Rock Specimens Under Constant Normal Force*). The TS is cut smaller than the shear boxes, with the length (L), width (W) and height (H); the inclined notches are made with small angle (α), horizontal length (A) and thickness (T), altering the length to effective length (L_e), as shown in Fig. 2.3a and 2.3b. The TS is encapsulated with a stronger material and between the upper and the lower part of the encapsulating material, a free space (S) is formed. A constant normal force is applied normal to the shear area and, after stabilization, a tangential force or displacement is applied parallel to the shear area (the forces are applied independently). The bottom of the left notch tip is aligned to the top of the right notch tip, and both are aligned with the tangential force and the support reaction (as presented in the detail of Fig. 2.3b and 2.3c). The average normal stress (σ_n) is calculated as the ratio between the normal force

and the shear area ($Area = L_e \cdot W$) and the average shear stress at the rupture ($\tau_{(av)}$) is calculated as the ratio between the tangential force and the shear area.

Fig. 2.3. MDST geometry: a) plant; b) section-A and c) detail.



2.3 IDEAL GEOMETRY OF THE MDST

The ideal geometry of the MDST is a geometric model that promotes a single horizontal shear fracture (without tensile fracture propagation) and meets the ASTM D5607-16 (2016) recommendations for DST: i) the relationship between the dimensions L_e and W must be equal to or greater than 0.75 or equal to or less than 1.25; ii) the smallest free space between encapsulating materials must be equal or greater than 0.5 cm; iii) the smallest shear area is 19 cm² and iv) the smallest vertical encapsulated dimension of the TS (D) must be at least 20 % of the length of the TS (Fig. 2.3).

Considering the direct shear machine's dimensions and the ASTM D5607-16 recommendations, three models were analyzed in the two next sections (through numerical analysis and experimental tests in concrete) to determine the ideal geometry. Table 1 shows the geometrical parameters of the models. These models differ in notch length, angle and effective length (the effective lengths adopted were considered whole numbers and the angles of the notches were obtained geometrically). The length was adopted at 8.0 cm, because the maximum dimension of the shear box utilized was 10.0 cm, remaining 1.0 cm for each side. The width was fixed at 4.0 cm, to results in $0.75 \leq L_e / W \leq 1.25$ in all models. The free space between encapsulating materials was fixed at 0.5 cm. Only Model 1 meets the recommendation of the minimum area, but this question will be considered later.

Table 2.1 - MDST models

Model	Geometrical parameters									
	L (cm)	A (cm)	L_e (cm)	W (cm)	α (°)	S (cm)	D (cm)	T (cm)	L_e / W	Area (cm ²)
1	8.00	1.50	5.00	4.00	10.00	0.50	1.70	0.30	1.25	20.00
2	8.00	2.00	4.00	4.00	7.00	0.50	1.70	0.30	1.00	16.00
3	8.00	2.50	3.00	4.00	5.00	0.50	1.70	0.30	0.75	12.00

The three models were analyzed in the two next sections (through numerical analysis and experimental tests in concrete) to determine the ideal geometry.

2.3.1 STRESS ANALYSIS OF MODELS

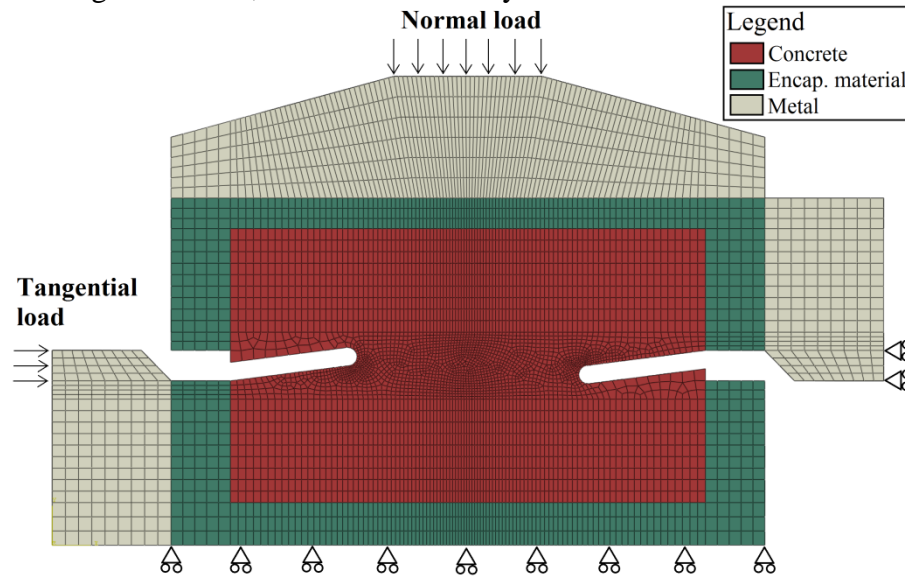
A linear elastic analysis was performed to assess the stresses occurring in the models in its pre-peak stage (before the rupture) and to check which of the models promotes less tensile stress in the TS, to avoid tensile fractures. The Finite Element Method was used through the Abaqus 6.14 program, developed by Dassault Systèmes Simulia Corp.

The numerical models were created with geometry, loads and boundary conditions, as shown in Fig. 2.4 (Model 2 – intermediate model). The plane strain was simulated using the mesh with 8-node linear brick, reduced integration and hourglass control elements. The analysis was linear elastic, the applied loads were static and the test is performed in two steps (the normal stress was applied first and the shear stress was applied later). Three $\sigma_{n(av)} = 1.0$, 5.0 and 10.0 MPa and three $\tau_{(av)} = 8.85$, 12.20 and 16.40 MPa were considered, respectively. Typical mechanical properties of the materials were adopted for the analysis and they are shown in Table 2.2.

Table 2.2 - Mechanical properties of materials

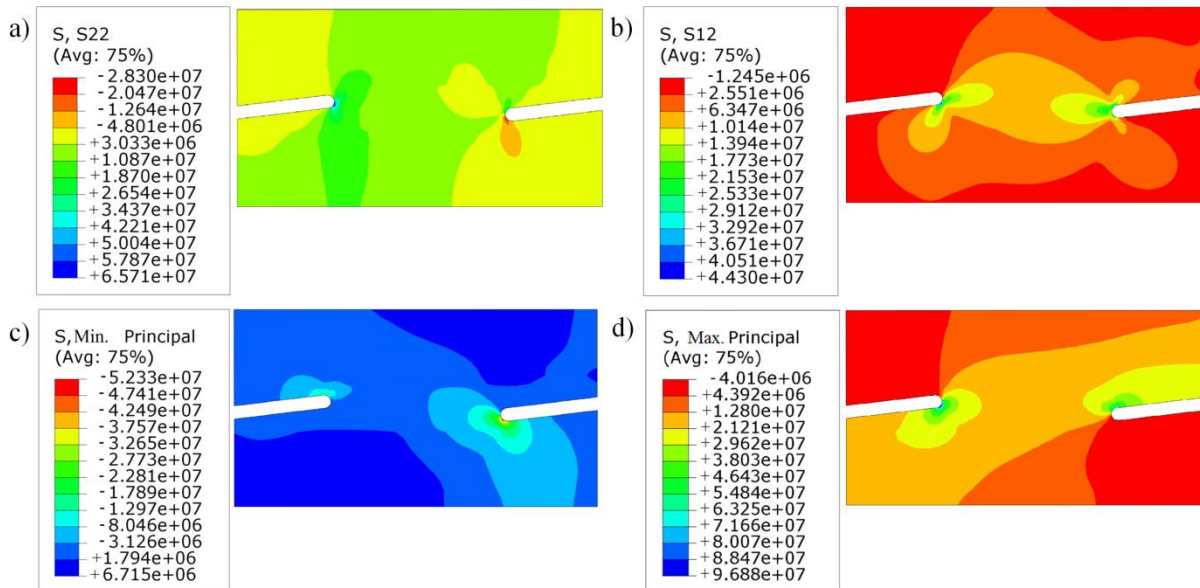
Materials	Elastic modulus (E) (GPa)	Poisson's ratio (ν)
Concrete	30.00	0.20
Metal (steel 304)	193.00	0.27
Encapsulating material	35.00	0.20

Fig. 2.4. Mesh, loads and boundary conditions of the MDST.



The normal stress (S_{22}), shear stress (S_{12}), minimum principal stress (S_{min}) and maximum principal stress (S_{max}) were analyzed. This work follows the geotechnical convention, that is, positive signs refer to compression and negative signs refer to tensile. Fig. 2.5 shows the result of Model 2 (intermediate model) for $\sigma_{n(av)} = 5.0$ MPa (intermediate stress) as a visual example. The stress state of all models and for all average normal stresses was analyzed in a straight line connecting the two notches (L_e (path)) located in center of the TS (Fig. 2.6).

Fig. 2.5. Visual example of the MDST stress state (Model 2) for $\sigma_{n(av)} = 5$ MPa: a) normal stress; b) shear stress; c) minimum principal stress and d) maximum principal stress. Values in Pa.

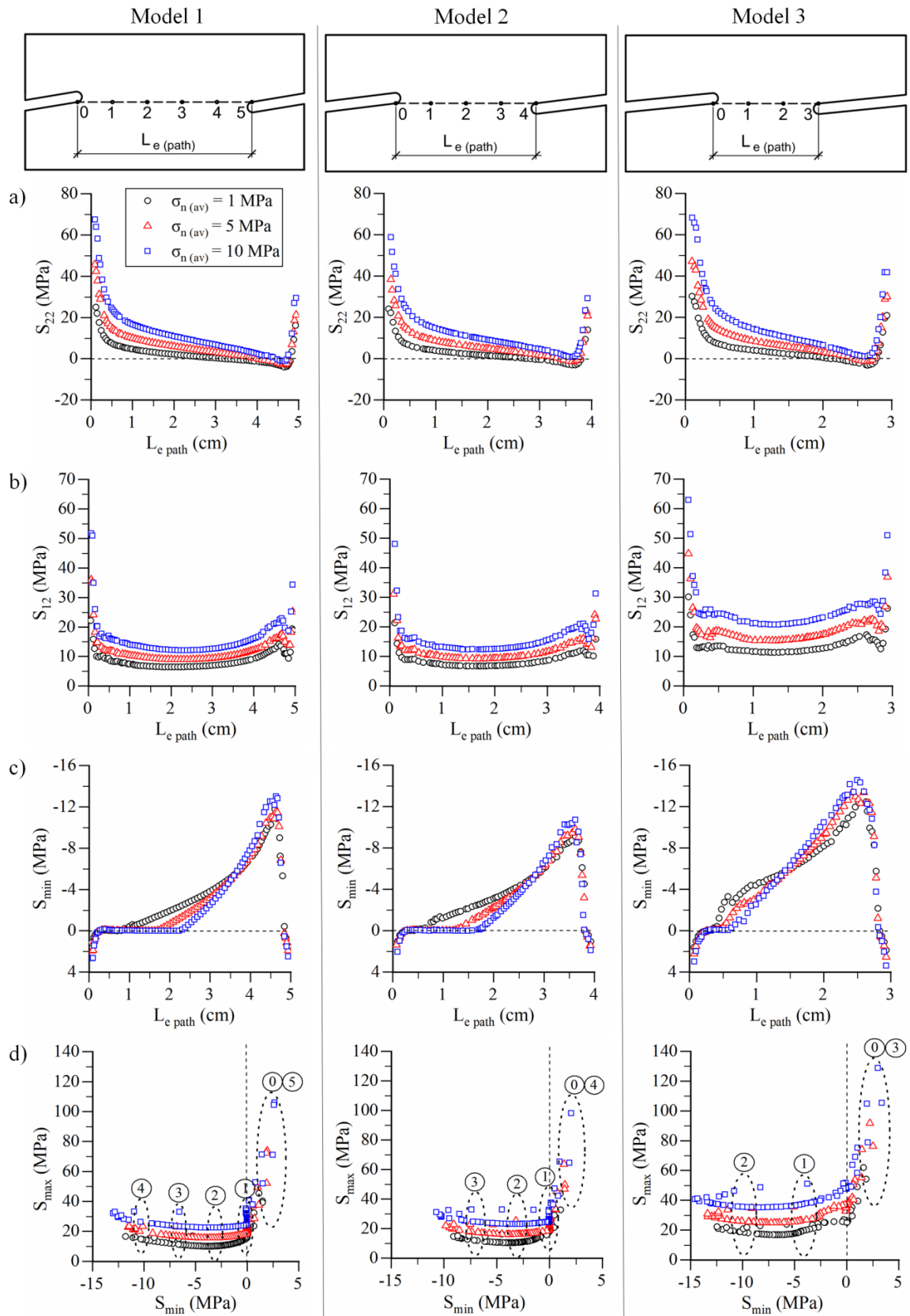


For all models, the following typical behaviors are noted:

- normal and shear stresses are heterogeneous along the shear area and concentrate on the notches;
- significant principal tensile stresses occur above the left notch tip and below the right notch tip, where tensile fracture (wing) may occur;
- along the L_e (path) it is noted that: i) confined tensile (S_{min} negative and S_{max} positive) occurred around the center to the right of the TS, where tensile fracture (en echelon) may occur and ii) confined compression (S_{min} positive and S_{max} positive) occurred below the left notch tip and above the right notch tip, where shear fracture may occur.

Comparing the models, Model 2 presented lower maximum tensile stress and confined tensile than the other models, which prevents tensile fractures (wing and en echelon).

Fig. 2.6. Stress state in a straight line connecting the two notches placed in center of TS for the three models: a) normal stress; b) shear stress; c) minimum principal stress and d) minimum versus maximum principal stress.



Obs: the numbers that appear in the figures in the letter *d* are the L_e ($_{\text{path}}$) distances.

2.3.2 EXPERIMENTAL TESTS OF MODELS IN CONCRETE

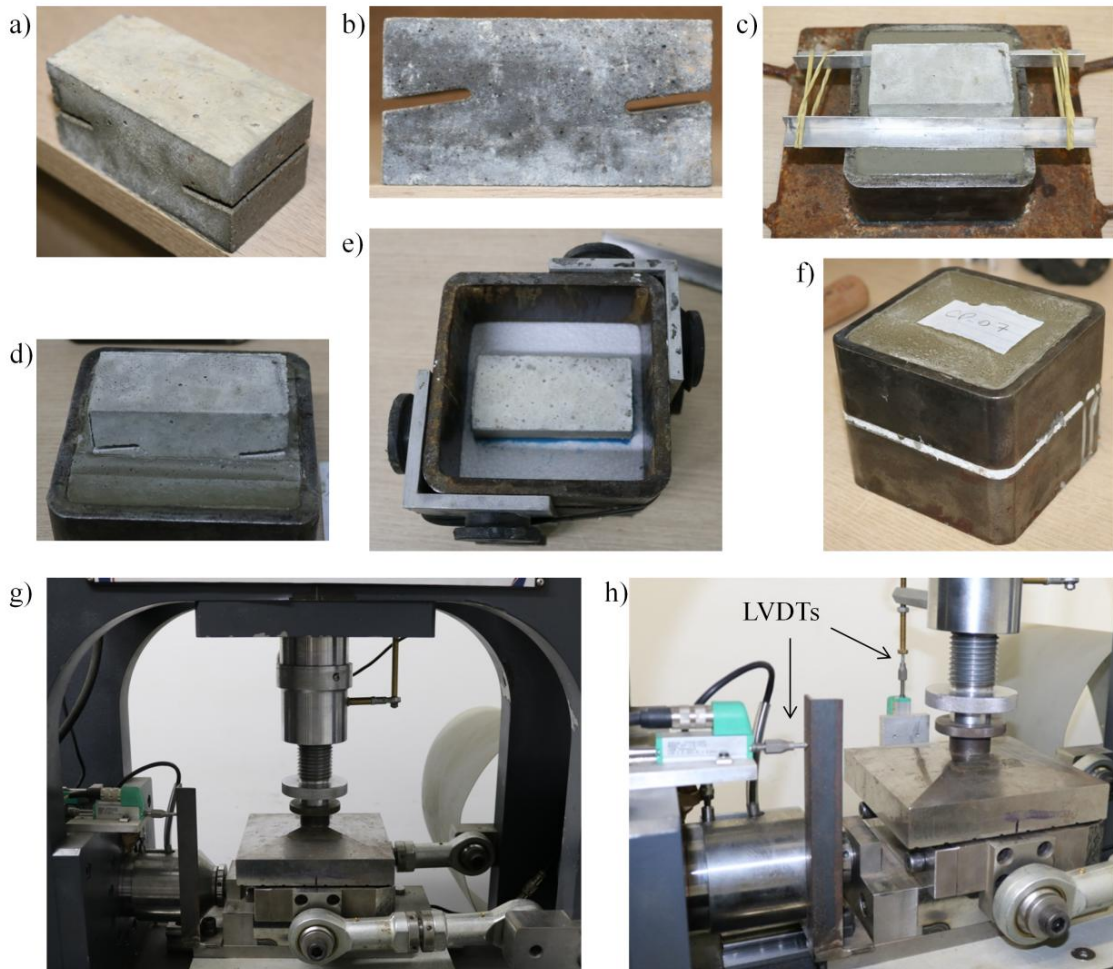
Experimental tests were performed in concrete to analyze the fracture pattern of the three models. The ideal geometry should promote a single horizontal shear fracture without tensile fractures.

A concrete (micro-concrete) was used as a material model to prevent large variations in the material due to the natural formation process. The concrete was prepared with 28-day moist curing with the ingredients: i) fine sand (775 kg/m^3), ii) coarse sand (775 kg/m^3); iii) cement – type 5 (500 kg/m^3); iv) water-cement ratio (0.5) and v) plasticizer (1 %). The uniaxial compressive strength of this concrete was determined by four compression tests with an DL-10000™ hydraulic machine, manufactured by Emic SA (São José dos Pinhais, Brazil), with a 100 kN load cell (loading rate of 0.04 MPa/s), resulting in 46.12 MPa with standard deviation equal to 1.12 MPa.

The procedures for performing the MDST are: i) the TS is molded with L , W and H dimensions; ii) the notches are made with a inclined circular saw (Fig. 2.7a and 2.7b); iii) the TS is encapsulated with cement paste (cement – type 5, 25% of water and 1% of plasticizer) in the lower metallic form (Fig. 2.7c and 2.7d); iv) after 1-day of moist curing of the cement paste, a styrofoam sheet (0.5 cm thick) is placed on the top of the lower encapsulating material to make a free space between the lower and the upper encapsulating materials (Fig. 2.7e); modeling paste was used to cover some spaces formed between the styrofoam and the TS; v) the upper metallic form is positioned and fixed with angle supports, and the TS is encapsulated with cement paste (Fig. 2.7f); and vi) after 7-day moist curing of the cement paste, the angle supports and the styrofoam sheet are removed and the TS is placed in the machine (Fig. 2.7g and 2.7h).

A servo-controlled direct shear machine, with a 300 kN load cell and linear variable differential transformers (LVDTs) in both vertical (normal) and horizontal (shear) directions, was used in this study. The test had two steps: i) the normal force was applied with constant rate of 1.0 kN/min and ii) the tangential displacement was applied with constant rate of 0.05 mm/min.

Fig. 2.7. Procedures for performing the MDST: a) dimensions of TS and notches; b) length and angle of notches; c) and d) lower encapsulating; e) styrofoam sheet; f) upper encapsulating; g) direct shear machine and h) LVDTs.



The first experimental tests were carried out for $\sigma_n (av) = 2.0$ MPa. The dimensions and results of the tests are presented in Table 2.3, the force versus displacement curves are presented in Fig. 2.8 and the visual results of the fracture pattern of the tests are presented in Fig. 2.9. The fracture pattern of the tests analyzed in this work is from the mesoscopic point of view and the classification of the fracture in horizontal or inclined is approximate.

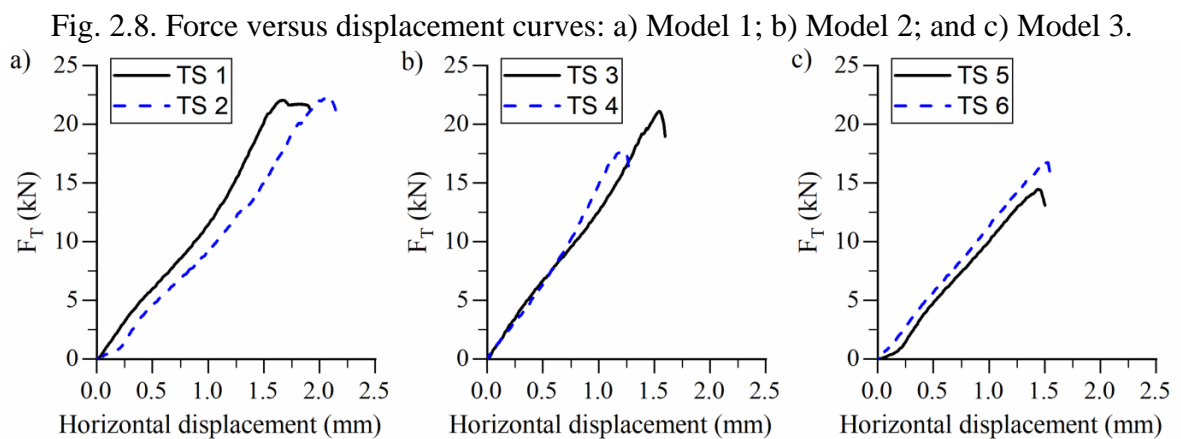


Table 2.3 - Experimental tests of models

TS	$\sigma_n^{(av)}$ (MPa)	Model	Geometrical parameters										
			L (cm)	L_e (cm)	A (cm)	W (cm)	H (cm)	α (°)	S (cm)	D (cm)	T (cm)	Area (cm ²)	L_e / W
1	2.00	1	8.11	5.04	1.53	4.05	4.03	10.00	0.50	1.71	0.30	20.41	1.24
2	2.00	1	8.08	5.00	1.54	3.99	4.02	10.00	0.50	1.71	0.30	19.95	1.25
3	2.00	2	8.19	4.16	2.01	4.10	4.07	7.00	0.50	1.73	0.30	17.08	1.01
4	2.00	2	8.20	4.18	2.01	4.06	3.99	7.00	0.50	1.70	0.30	16.93	1.03
5	2.00	3	8.09	3.12	2.49	4.05	4.07	5.00	0.50	1.74	0.30	12.64	0.77
6	2.00	3	8.02	3.15	2.43	4.07	4.07	5.00	0.50	1.73	0.30	12.83	0.77

Model 1 (TS 1 and TS 2) showed a single inclined tensile (en echelon) followed by shear fracture. The TS 1 fracture goes over the right notch and the TS 2 fracture goes under the left notch. The force versus displacement curve of the TS 1 was approximately linear with non-abrupt rupture and the TS 2 was approximately linear with abrupt rupture. Model 2 (TS 3 and TS 4) showed a single horizontal shear fracture, connecting the top of the right notch with the bottom of the left notch (where the shear stress was concentrated). The force versus displacement curve showed an approximately linear behavior with abrupt rupture. Model 3 presented the same behavior as Model 2.

Comparing the models, Models 2 and 3 presented better results (single horizontal shear fracture) than Model 1. Comparing Models 2 and 3, Model 2 presented fewer tensile stresses in the numerical analyses and it allows testing materials with grains sizes up to 4 mm (considering the 1:10 ratio between grain size and TS length, due to the size effect). Therefore, Model 2 was selected for a second experimental verification for different average normal stresses.

The second experimental study analyzed the Model 2 for six normal stresses (starting at 0.5 MPa to 20.0 MPa). The dimensions and results of the tests are presented in Table 2.4, the force versus displacement curves and the peak shear strength envelope are presented in Fig. 2.10 and the visual results of the fracture pattern are presented in Fig. 2.11.

For all normal stresses, Model 2 presented a single horizontal shear fracture and the force versus displacement curve showed an approximately linear behavior with abrupt rupture. Concluding the analysis of the models and choosing an ideal geometry, Model 2 presented excellent results and advantages over the others models.

Fig. 2.9. Visual results of fracture pattern: a) TS 1; b) TS 2; c) TS 3; d) TS 4; e) TS 5 and f) TS 6.

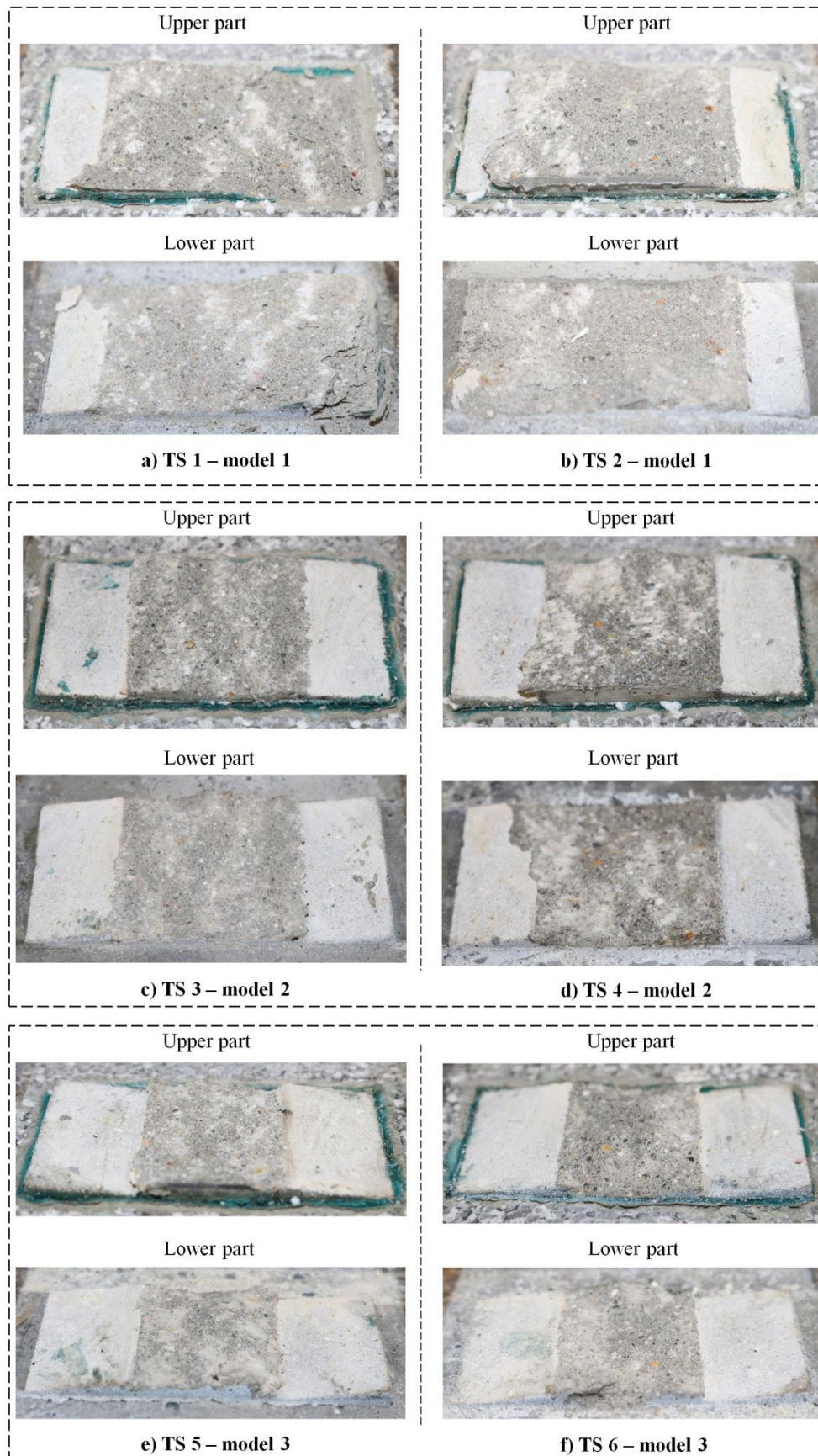


Table 2.4 - Experimental tests with Model 2

TS	$\sigma_{n(av)}$ (MPa)	Geometrical parameters										
		L (cm)	L_e (cm)	A (cm)	W (cm)	H (cm)	α ($^\circ$)	S (cm)	D (cm)	T (cm)	Area (cm 2)	L_e / W
7	0.50	8.06	3.97	2.05	4.06	4.06	7.00	0.50	1.73	0.30	16.10	0.98
8	0.50	8.09	3.73	2.18	4.09	4.05	7.00	0.50	1.72	0.30	15.25	0.91
9	1.00	8.03	3.79	2.12	3.98	4.04	7.00	0.50	1.72	0.30	15.10	0.95
10	1.00	8.06	4.17	1.94	4.08	4.08	7.00	0.50	1.74	0.30	17.01	1.02
11	5.00	8.05	4.14	1.96	4.09	4.01	7.00	0.50	1.70	0.30	16.90	1.01
12	5.00	8.02	3.98	2.02	4.08	4.03	7.00	0.50	1.72	0.30	16.24	0.98
13	10.00	8.04	3.92	2.06	4.03	3.97	7.00	0.50	1.69	0.30	15.81	0.97
14	10.00	8.11	3.85	2.13	4.15	3.98	7.00	0.50	1.69	0.30	15.97	0.93
15	20.00	8.02	4.10	1.96	4.04	4.01	7.00	0.50	1.70	0.30	16.58	1.01
16	20.00	8.10	3.99	2.05	4.10	4.01	7.00	0.50	1.70	0.30	16.35	0.97

Fig. 2.10. Force versus displacement curves of Model 2: a) $\sigma_{n(av)} = 0.5$ MPa; b) $\sigma_{n(av)} = 1.0$ MPa; c) $\sigma_{n(av)} = 5.0$ MPa; d) $\sigma_{n(av)} = 10.0$ MPa; e) $\sigma_{n(av)} = 20.0$ MPa and f) peak shear strength envelope.

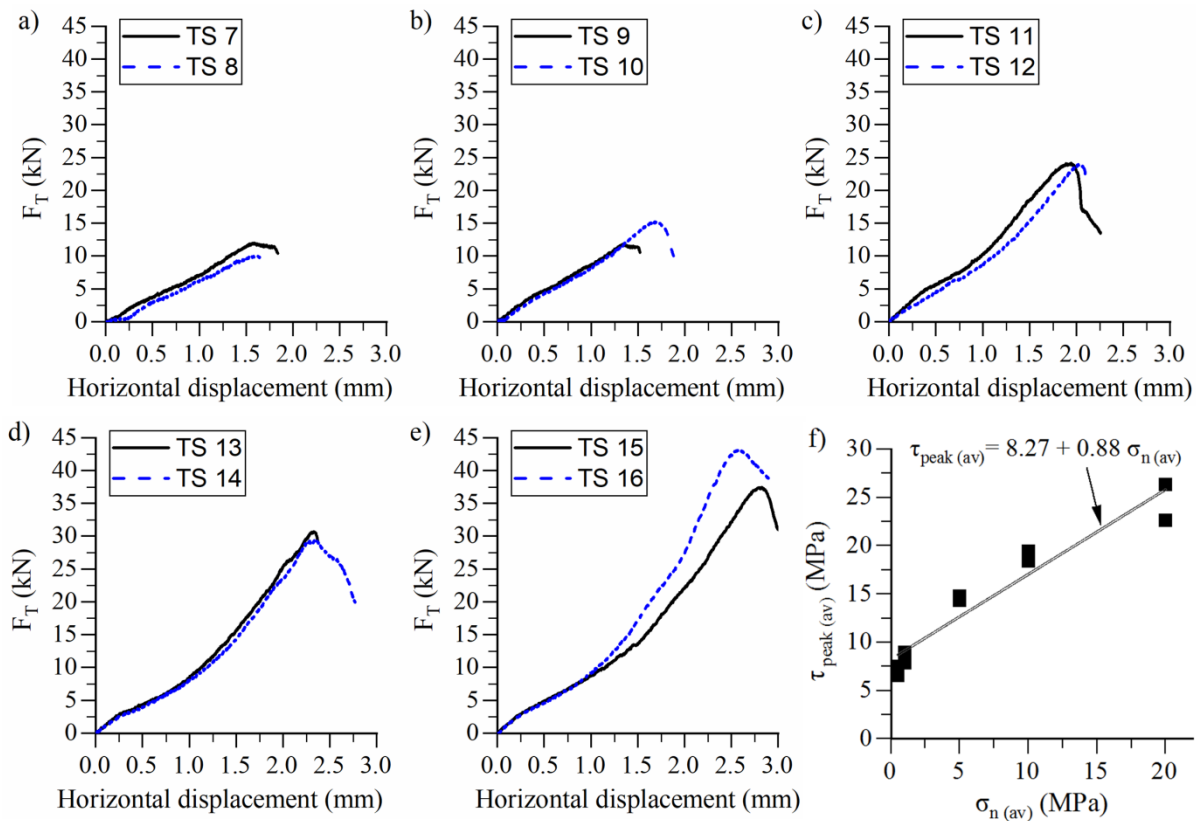


Fig. 2.11. Visual result of Model 2 fracture pattern: a) TS 7; b) TS 8; c) TS 9; d) TS 10; e) TS 11 and f) TS 12.

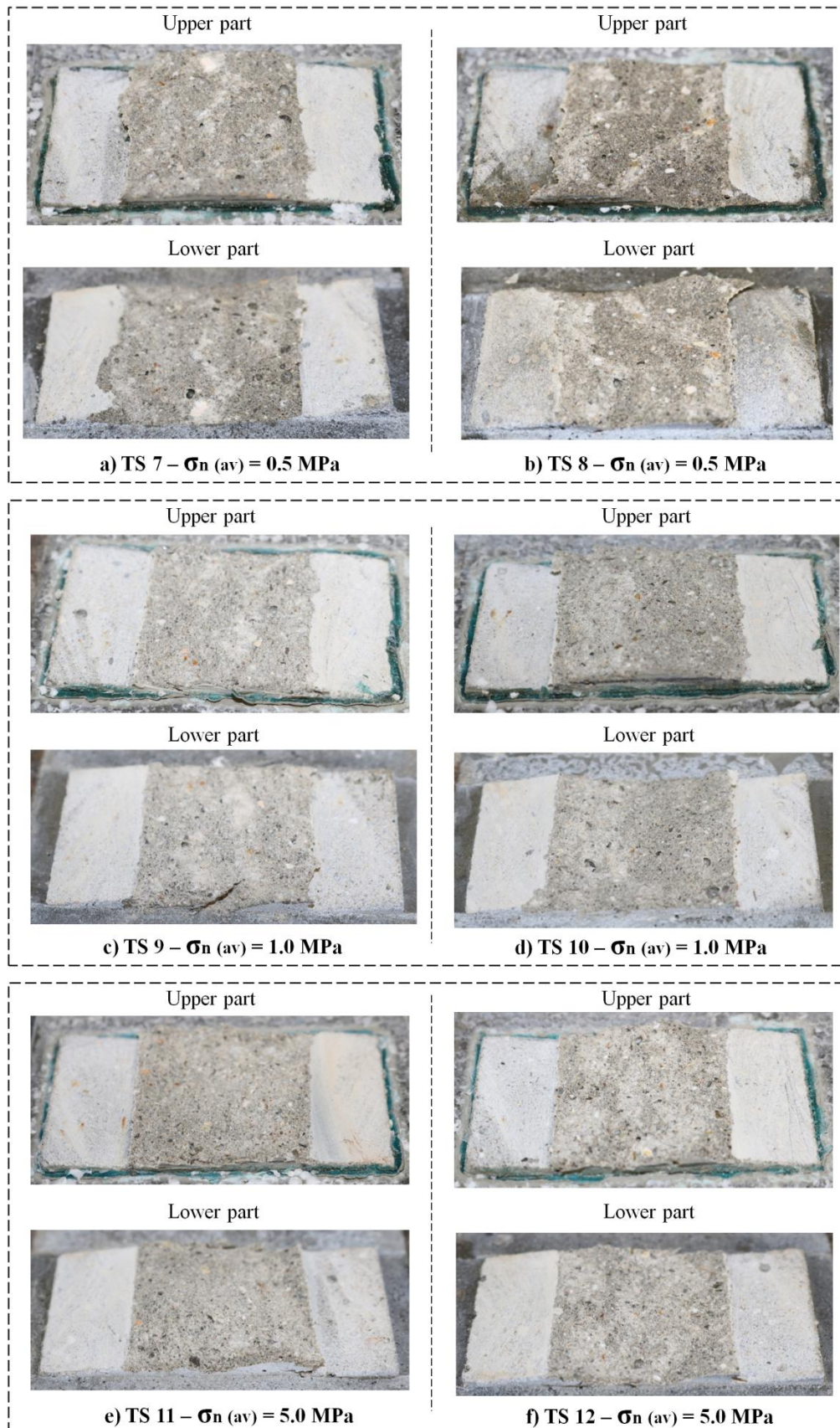
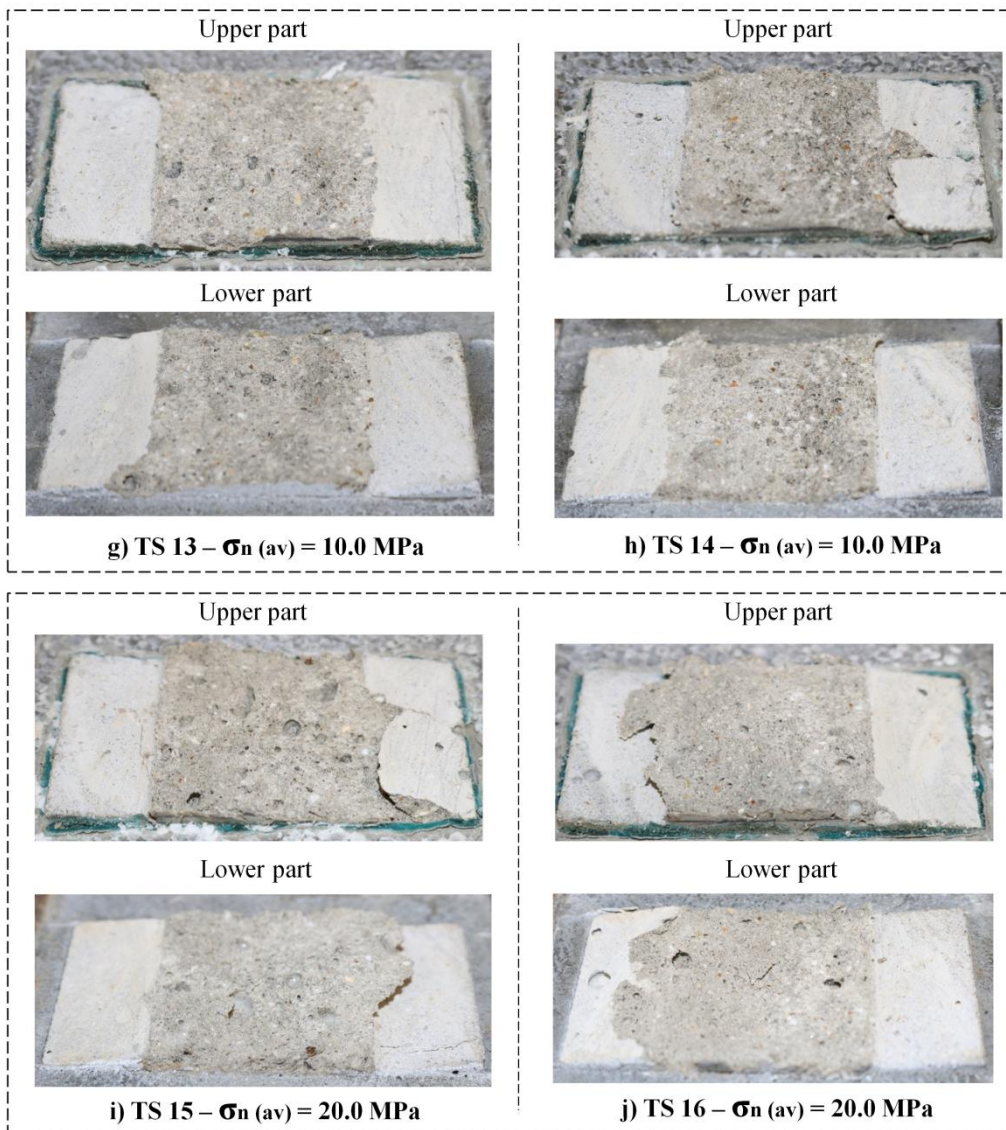


Fig. 2.11 (cont.). Visual results of fracture pattern: g) TS 13; h) TS 14; i) TS 15 and j) TS 16.



2.4 EXPERIMENTAL TESTS ON ROCKS USING IDEAL GEOMETRY

MDST experimental tests using the ideal geometry (Model 2) were performed in three homogeneous rocks: marble, silicified sandstone and mylonite (Fig. 2.12). The dimensions of the TSs are presented in Table 2.5. The dimension W of the ideal geometry was modified to approximately 5.0 cm to meet the ASTM D5607-16 (2016) recommendation of the minimal area (19 cm²).

The encapsulated material used was stronger than that used in concrete, and the ingredients are: i) cement – type 5; ii) water (25 %); iii) silica concentrate in suspension (10

); iv) plasticizer (1 %) and v) hydration reaction accelerator (1 %). The curing time was 28 days approximately.

Fig. 2.12. Rocks tested in MDST: a) marble; b) silicified sandstone and c) mylonite.



Table 2.5 - Experimental tests on rocks

Rock	Abrevi- ation	Geometrical parameters										
		L (cm)	L_e (cm)	A (cm)	W (cm)	H (cm)	D (cm)	T (cm)	α (°)	S (cm)	Area (cm ²)	L_e / W
Marble	M1	8.00	4.01	1.99	5.08	6.34	2.87	0.30	7.00	0.50	20.38	0.79
Marble	M2	8.29	4.23	2.03	5.00	6.19	2.74	0.30	7.00	0.50	21.17	0.85
Marble	M3	7.94	3.97	1.99	5.04	5.87	2.76	0.30	7.00	0.50	20.01	0.79
Marble	M4	7.95	4.08	1.93	5.03	6.16	2.82	0.30	7.00	0.50	20.53	0.81
Sandstone	S1	8.08	3.89	2.10	5.10	5.33	2.47	0.30	7.00	0.50	19.84	0.76
Sandstone	S2	8.05	3.84	2.11	5.08	5.43	2.49	0.30	7.00	0.50	19.48	0.76
Sandstone	S3	7.97	3.78	2.10	5.04	5.41	2.46	0.30	7.00	0.50	19.05	0.75
Sandstone	S4	7.93	4.19	1.87	4.95	4.89	2.27	0.30	7.00	0.50	20.73	0.85
Mylonite	My1	7.98	4.38	1.80	4.92	5.54	2.54	0.30	7.00	0.50	21.52	0.89
Mylonite	My2	8.08	4.13	1.97	4.72	5.99	2.80	0.30	7.00	0.50	19.52	0.87
Mylonite	My3	8.28	4.08	2.10	4.99	5.89	2.66	0.30	7.00	0.50	20.33	0.82
Mylonite	My4	8.31	4.18	2.07	4.57	6.38	2.80	0.30	7.00	0.50	19.09	0.92

The rock tests were performed in three steps: i) the peak test was carried out; ii) TS was removed from the machine and the photograph was taken; and iii) only for tests that presented a single horizontal shear fracture, the TS was returned to the machine, and the subsequent residual test was carried out. The direct shear machine used and the rock test setups were the same as those used for concrete tests.

Table 2.6 and Fig. 2.13 show the results of the tests. For each rock, the peak friction angle (ϕ_{peak}), cohesion (c') and residual friction angle (ϕ_{res}) was calculated. Fig. 2.14 shows the fracture pattern after the peak test (only the lower part of the TS is shown, to reduce the document size).

Table 2.6 - Results of experimental tests of rocks

TS	$\sigma_n (av)$ (MPa)	Results recorded		Results calculated			c' (MPa)	ϕ_{peak} (°)	ϕ_{res} (°)	Fracture type
		$F_T (peak)$ (kN)	$F_T (residual)$ (kN)	$\tau_{peak (av)}$ (MPa)	$\tau_{residual (av)}$ (MPa)					
M1	1.00	18.95	2.46	9.30	1.21				Shear	
M2	5.00	34.38	9.11	16.24	4.30				Shear	
M3	10.00	50.27	14.56	25.13	7.28	7.92	58.8	33.8	Shear	
M4	15.00	66.29	18.94	32.28	9.22				Shear	
S1	1.00	23.76	-	11.97	-				Tensile and shear	
S2	5.00	52.26	9.79	26.83	5.03	14.21	52.2	37.9	Shear	
S3	10.00	46.90	18.19	24.62	9.55				Shear	
S4	15.00	69.22	20.99	33.39	10.12				Shear	
My1	1.00	23.40	-	10.87	-				Tensile and shear	
My2	5.00	52.15	9.5	26.72	4.87	10.55	70.5	39.7	Shear	
My3	10.00	84.37	28.62	41.50	14.08				Shear	
My4	15.00	96.17	15.76	50.39	8.26				Shear	

All tests (marble, silicified sandstone and mylonite) presented a single horizontal shear fracture and the force versus displacement curve showed an approximately linear behavior with abrupt rupture, with the exception of tests S1 and My1, which presented an inclined tensile (en echelon) followed by shear fracture and the force versus displacement curve showed non-linear behavior with non-abrupt rupture.

In tests in which there was horizontal shear fracture and the force versus displacement curve was approximately linear with abrupt rupture, a striated surface in much of the sheared area (whitish appearance) was observed. PETIT (1987, 1988) interpreted that the striated surfaces in shear ruptures were due to the breaking of the grains of the rock.

In tests in which there was inclined tensile followed by shear fracture and the force versus displacement curve showed non-linear behavior with non-abrupt rupture (S1 and My1), striated surface was not observed. The fact that en echelon fractures occurs is related to the stress state of the test and the relationship between the tensile and shear strength of the material. The stress state of the test is inherent in the MDST, but the MDST has a better stress state than the DST, since wing fractures did not propagate and only en echelon fractures propagated for very low average normal (1 MPa) in silicified sandstone and mylonite.

The fracture pattern of the TS is not perfectly the same across the sheared area due to two factors: a) the material is not perfectly homogeneous it and may have differences in

strength, voids or microfractures and b) at the borders, some differences in the fracture inclination are noted (as in S3, S4, M2, My2, My3 and My4), probably due to the change from plane strain to plane stress state.

Fig. 2.13. Results of peak and residual tests: a) marble; b) sandstone and c) mylonite.

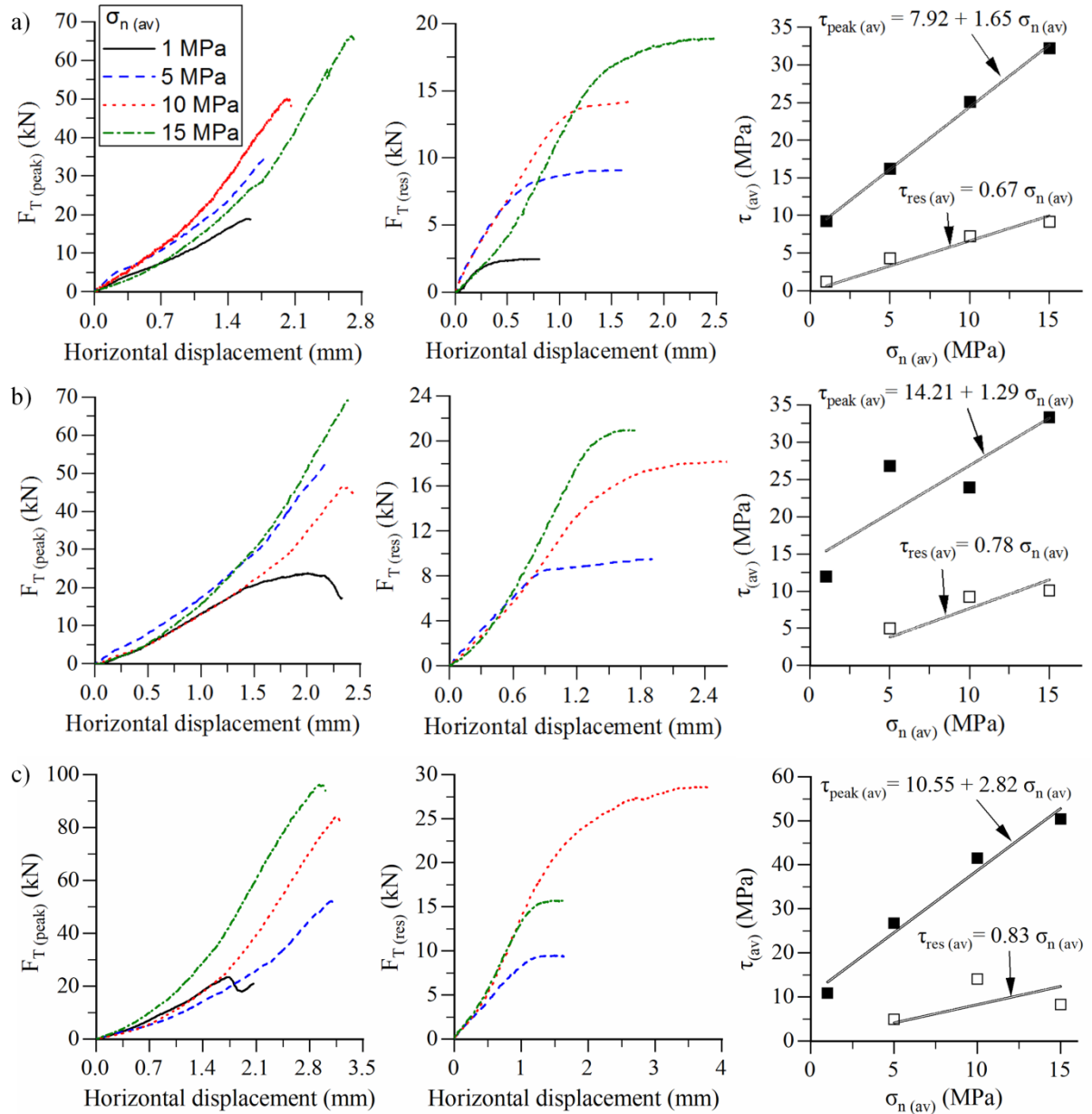
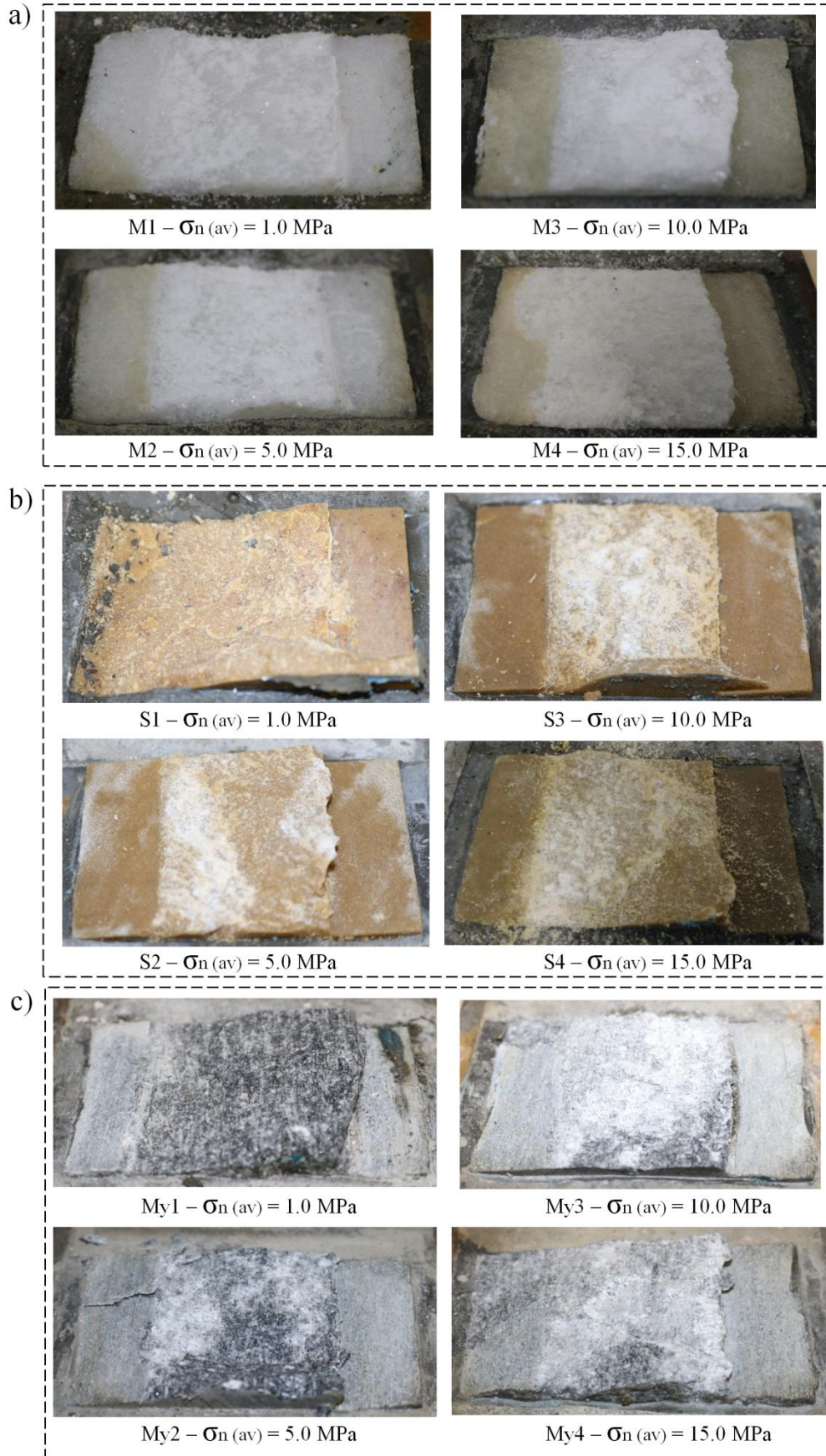


Fig. 2.14. Visual results of fracture pattern of rocks: a) marble; b) silicified sandstone and c) mylonite.

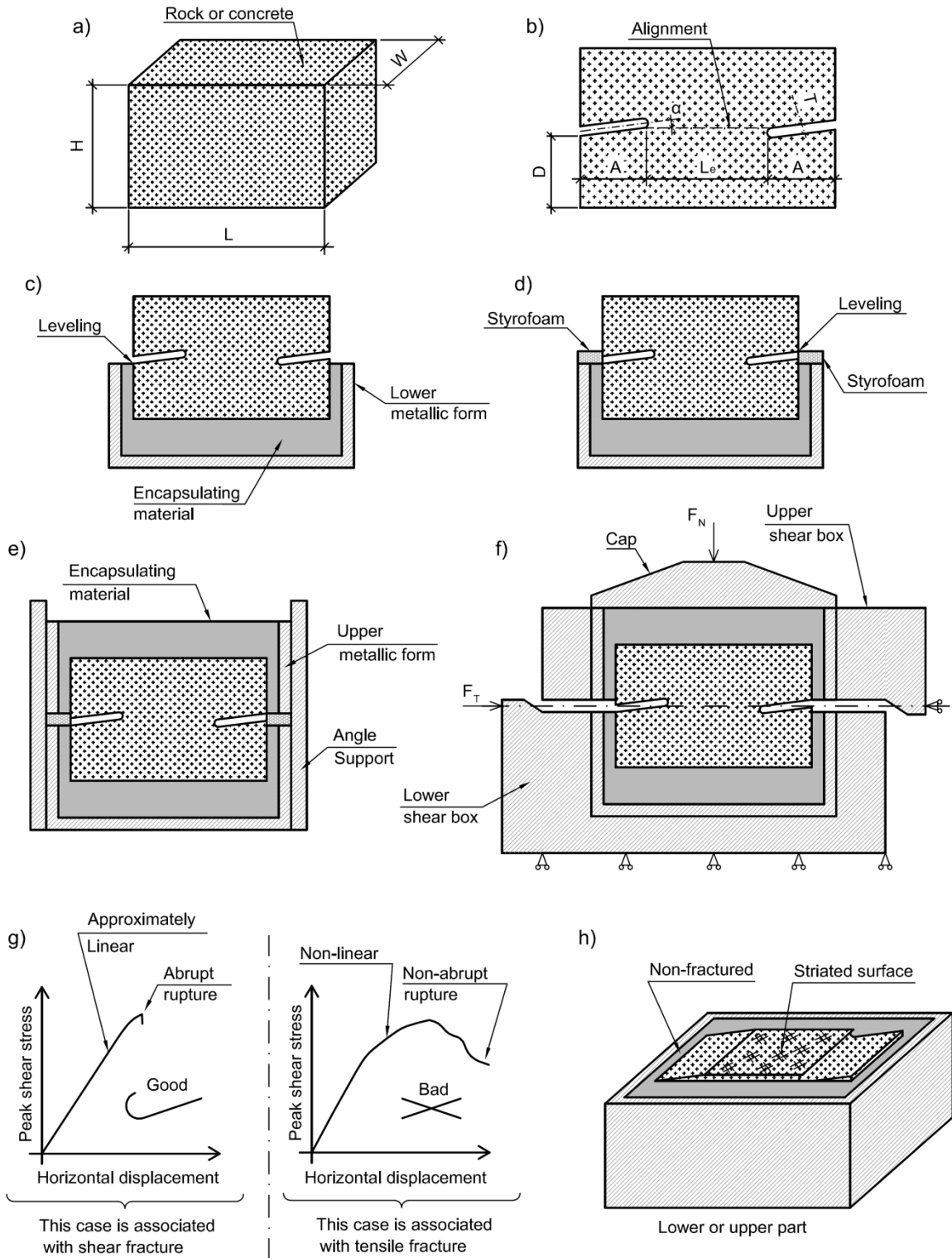


2.5 METHOD SUMMARY AND GUIDANCE

A summary and guidance for performing and verifying the MDST for homogeneous materials are providing below:

- a) the material is cut with $L = 8.00$ cm, $W = 5.00$ cm and $H \approx 5.00$ cm ($D \geq 0.2 L$) (Fig. 2.15a);
- b) the notches are made with $A = 2.00$ cm, $\alpha = 7.00^\circ$ and $T = 0.3$ cm, aligning the bottom of the left notch tip with the top of the right notch tip (Fig. 2.15b). The notch angle (α) can be made with an inclined circular saw;
- c) the TS is encapsulated in the lower metallic form, leveling the beginning of the left notch with the top of the lower metallic form (Fig. 2.15c). After 1-day of moist curing, a styrofoam (0.5 cm thick) is placed around the TS to form the free spacing between the encapsulating materials (Fig. 2.15d). Modeling paste can be used to cover some spaces formed between the styrofoam and the TS. The upper metallic form is placed on the styrofoam, fixed with angle supports and encapsulated (Fig. 2.15e). After 28-days of moist curing (approximately), the angle supports and the styrofoam are removed, and the TS is positioned in the machine. The tangential force (F_T) and the support reaction must be aligned with the center of the TS (Fig. 2.16f);
- d) the peak test is performed; the $\sigma_n (av)$ and $\tau_{peak (av)}$ are recorded and the peak friction angle and cohesion are calculated. The test must be presented:
 - force versus displacement curve approximately linear with abrupt rupture (Fig. 2.15g);
 - single horizontal shear fracture, connecting the top of the right notch tip with the bottom of the left notch tip, in the most sheared area (Fig. 2.15h). The fracture pattern must be analyzed in the entire sheared area (it should not be analyzed from an external lateral view);
 - striated surface in the most shear area (Fig. 2.15h);
 - non-fractured encapsulating material (Fig. 2.15h).
- e) residual subsequent test is performed; the $\sigma_n (av)$ and $\tau_{res (av)}$ are recorded and the residual friction angle is calculated.

Fig. 2.15. Steps for performing and verifying the MDST for homogeneous materials: a) cut of the material; b) notches; c) lower encapsulation; d) styrofoam; e) upper encapsulation; f) test; g) stress versus displacement curve and h) fracture pattern verification.



2.6 CONCLUSION

This paper proposes a modification in the DST to improve the boundary conditions of the test. It was possible to reduce or even to eliminate the undesirable tensile fractures, resulting in a better shear strength test method. The MDST can be performed for both intact materials strength and sliding friction tests, in homogeneous materials or with planes of weakness, including natural or artificial discontinuities, as prescribed in ASTM (2016). This study was carried out for homogeneous rock (most problematic case) and for low and very low normal stresses (where tensile fractures are more pronounced). The main conclusions of this study are listed below:

- a) the wing fractures did not propagate;
- b) an echelon fracture followed by shear fracture propagated only for very low normal stress (1 MPa) for silicified sandstone and mylonite;
- c) in the concrete and marble studied, all the TS and for all confining pressure ranging studied (1 to 15 MPa) show horizontal shear fracture without tensile fractures. In silicified sandstone and mylonite, for very low normal stress (1 MPa), the tests presented an echelon fracture followed by shear fracture, and for low normal stresses (5 to 15 MPa), the tests presented horizontal shear fractures without tensile fractures;
- d) the horizontal shear fracture propagated in the tests connected the top of the right notch tip with the bottom of the left notch tip and the fracture pattern of the TS is not perfect across the sheared area, due to the heterogeneities and probably due to the change from plane stress to plane strain state at the borders;
- e) an ideal geometry was proposed: $L = 8.00$ cm, $A = 2.00$ cm, $L_e = 4.00$, $W = 5.00$ cm, $\alpha = 7.00^\circ$, $T = 0.3$ cm, $S = 0.50$ cm and $D \geq 0.20 L$. In this study, a 10.00 cm shear box was used, remaining 1.00 cm on each side of the TS, which it was filled with encapsulating material and its metallic form. For the case where the shear box is larger than 10.00 cm, the same size of the TS can be maintained and the remaining distance of the encapsulating material is increased. Another alternative is to increase the size of the TS, keeping the same proportion. The dimensions ratio is: $A = L / 4$, $L_e = L / 2$, $0.75 \leq L_e / W \leq 1.25$, $\alpha = 7.00^\circ$, $T = L / 26.7$, $S = L / 16$ and $D \geq 0.20 L$. Sizes smaller than the proposed ideal geometry (even keeping the dimensions ratio) are not recommended, as they may not meet ASTM D5607-16 recommendations;

- f) the encapsulating material must not fracture during the test; otherwise it may influence the fracture mode, invalidating the test;
- g) in the tests whereby horizontal shear fracture occurred, the force versus displacement curve showed an approximately linear behavior with abrupt rupture and the striated surface was observed in much of the sheared area (whitish appearance). These experimental evidences characterize the shear rupture;
- h) in the tests whereby inclined tensile (en echelon) followed by shear fracture occurred, the force versus displacement curve showed non-linear behavior with non-abrupt rupture and the striated surface was not observed. These experimental evidences characterize the significant influence of tensile fractures (which is undesirable in the test);
- i) the MDST is intended for testing material with grain size up to 4 mm. For materials with grains sizes larger than 4 mm, larger TS must be performed, keeping the dimensions ratio proposed;
- j) the stress state of the MDST is heterogeneous and the shear strength of the material determined in this study was an average result.

It is recommended for future studies to perform the MDST: i) for materials that have planes of weakness, including natural or artificial discontinuities (the planes of weakness or discontinuities must be aligned with the top of the right notch tip and the bottom of the left notch tip); ii) for high normal stresses and iii) for larger sizes of the TS, using the dimensions ratio proposed (ideal geometry) and iv) for different geometrical parameters, to confirm the ideal geometry.

3 MODE II FRACTURE TOUGHNESS DETERMINATION OF ROCK AND CONCRETE VIA MODIFIED DIRECT SHEAR TEST

Abstract: The Modified Direct Shear Test (MDST) was proposed for determining K_{IIc} in function of confining pressure of homogeneous rock and concrete. The study was carried out by numerical analysis and the main conclusions are as follows: i) MDST is suitable for K_{IIc} determination, since mode II prevails in the test; ii) horizontal fractures in the MDST is due to shear; iii) the confining pressure must be determined at the fracture tip ($\sigma_n (tip)$) and iv) two equations were proposed for determining K_{IIc} in function of $\sigma_n (tip)$. A practical example was provided and K_{IIc} envelopes were obtained for some rocks and concrete.

Keywords: Mode II fracture toughness. Modified Direct Shear Test. Rock. Concrete.

3.1 INTRODUCTION

Rock and concrete failure prediction is an important step in the design and analysis of geotechnical works to ensure their stability and safety. In recent decades, fracture mechanics concepts have been increasingly used by different authors and with different numerical methods, as could be seen in different literature reviews (JING; HUDSON, 2002; JING, 2003; BOBET et al., 2009; RABCZUK, 2013; NIKOLIĆ; ROJE-BONACCI; IBRAHIMBEGOVIĆ, 2016; MOHAMMADNEJAD et al., 2018). The determination of fracture resistance becomes extremely important, since it is the basis of any method.

The Linear Elastic Fracture Mechanics (LEFM) is usually applied to predict the fracture propagation in brittle materials, such as rocks and concretes. LEFM concepts are based on three modes of loading at the fracture tip: I (tensile), II (shear-sliding) and III (shear-tearing). The principal parameter of this approach is the stress intensity factors (SIFs) for a particular mode (K_I , K_{II} and K_{III}). SIFs were proposed by IRWIN (1958), based on previous studies by INGLIS (1913) and GRIFFITH (1920), representing the magnitude of the fracture tip stress field in a homogeneous linear elastic material. They depend on the material type, geometry, displacement constraints and external load applications. Fracture propagation occurs when SIFs reach a critical value (K_{Ic} , K_{IIc} and K_{IIIc}), called fracture toughness. Fracture toughness is an intrinsic parameter of the material that represents its fracture resistance (ATKINSON, 1987; WHITTAKER; SINGH; SUN, 1992).

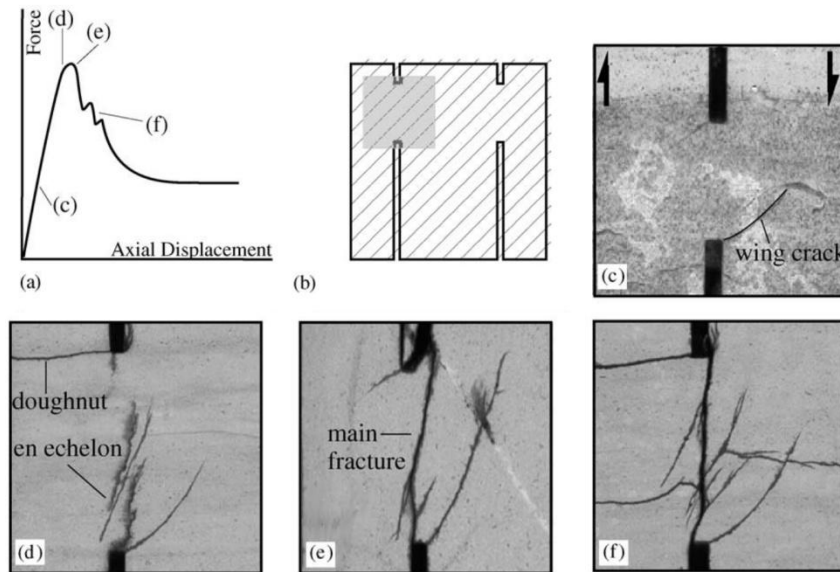
K_{IIc} is a very important property in rock mechanics, since the rock mass is solicited by compression stresses exerted by its own weight, causing shear failure by consequence, as observed in geological structures and engineering works (MELIN, 1986; ATKINSON, 1987; LAWN, 1993; BROBERG, 1999). Moreover, K_{IIc} strongly depends on the frictional resistance and must be determined in function of the confining pressure (RAO et al., 1999).

There are three experimental test methods proposed in the literature to determine K_{IIc} in function of the confining pressure for rock and concrete: i) Compressive-Shear Test (RAO et al., 1999), ii) Punch-Through Shear with Confining Pressure test (PTS-CP) (BACKERS; STEPHANSSON; RYBACKI, 2002) and iii) Modified Punch-Through Shear with Confining Pressure Test (MPTS-CP), which is a rectangular version of PTS-CP (LEE, 2007). One restriction of the Compressive-Shear Test is that the confining pressure depends on the applied shear stress, limiting the application of the confining pressure (BACKERS, 2004).

The International Society of Rock Mechanics and Rock Engineering (ISRM) suggested PTS-CP for determining K_{IIc} in function of the confining pressure for rocks (BACKERS; STEPHANSSON, 2012). Some authors performed PTS-CP tests on rock and concrete (BACKERS; STEPHANSSON; RYBACKI, 2002; BACKERS et al., 2004; YAO et al., 2017; WU; KEMENY; WU, 2017). The aforementioned authors indicated the following complications in PTS-CP: i) for “low” confining pressure (< 30 MPa), tensile fractures (wing, doughnut and en echelon) developed in the tests (Fig. 3.1a, 3.1b, 3.1c and 3.1d); ii) the shear fracture (main fracture) is inclined, starting on the left side of the bottom notch and arriving on the right side of the upper notch, and vice-versa for another notch (Fig. 3.1e and 3.1f), and; iii) the confining pressure causes bending stress at the fracture tip.

Tensile fractures (en echelon, wing and doughnut) are undesirable in the test, where a perfect mode II experimental test method should lead to a single flat fracture without any influence of tensile fractures (ENGELDER, 1987). The Modified Direct Shear Test (MDST) was proposed in Chapter 2 for determining shear strength of rock and concrete and it was possible to reduce or even to eliminate undesirable tensile fractures and a single horizontal (flat) shear fracture was achieved for most of the cases studied. The MDST basically consists in adding two inclined notches in the test specimen (TS) of the direct shear test, improving the boundary conditions of the test (Fig. 3.2a). In the concrete and marble studied, all the TS and for all confining pressure ranging studied (1 to 15 MPa) show horizontal shear fracture without tensile fractures. In silicified sandstone and mylonite, for very low normal stress (1 MPa), the tests presented en echelon fracture followed by shear fracture, and for low normal stresses (5 to 15 MPa), the tests presented horizontal shear fractures without tensile fractures (Fig. 3.2b). Moreover, the force versus displacement curves was approximately linear with abrupt rupture and striated surface is observed in much of the sheared area (whitish appearance) (Fig. 3.2b), which indicates the typical shear rupture, according to PETIT (1987, 1988).

Fig. 3.1. Fractures evaluation in Rudersdorf limestone at different stages of axial loading (confining pressure 5 MPa).



Source: BACKERS; STEPHANSSON; RYBACKI (2002).

This paper proposes the MDST for determining K_{IIc} in function of the confining pressure of homogeneous rock and concrete. The principal differences between MDST and PTS-CP are: i) the tangential load (F_T) is aligned with the shear area; ii) the notches are inclined (not having a level difference between the places where the fracture initiates and ends) providing a horizontal fracture (parallel to the shear force and normal to the normal force); iii) the confining pressure is applied with a normal force (F_N) concentrated at the center of TS, reducing the bending moment generated at the notches tips and iv) the direct shear machine is used.

This study used the numerical method for computing SIFs of the MDST. The structure and overview of the paper is as follows (Fig. 3.3): i) the geometric parameters of the MDST are presented and the ideal geometry proposed in Chapter 2 is analyzed based on the recommendations reported in the literature for mode II fracture toughness tests; ii) the numerical methods and models are presented; iii) a fracture analysis of the MDST was performed to analyze the typical SIFs and fracture pattern of the test; iv) a mechanical property parametric study was carried out to evaluate the effects of the parameters on K_{IIc} determination; v) a simple way to determine K_{IIc} via MDST was proposed through two equations and vi) a practical example of the method application was provided and K_{IIc} envelopes were determined for some rocks.

Fig. 3.2. Example of MDST for rocks and concrete with confining pressure 5 MPa: a) geometry and b) experimental fracture pattern (lower part of the TS) and c) force versus horizontal displacement curves.

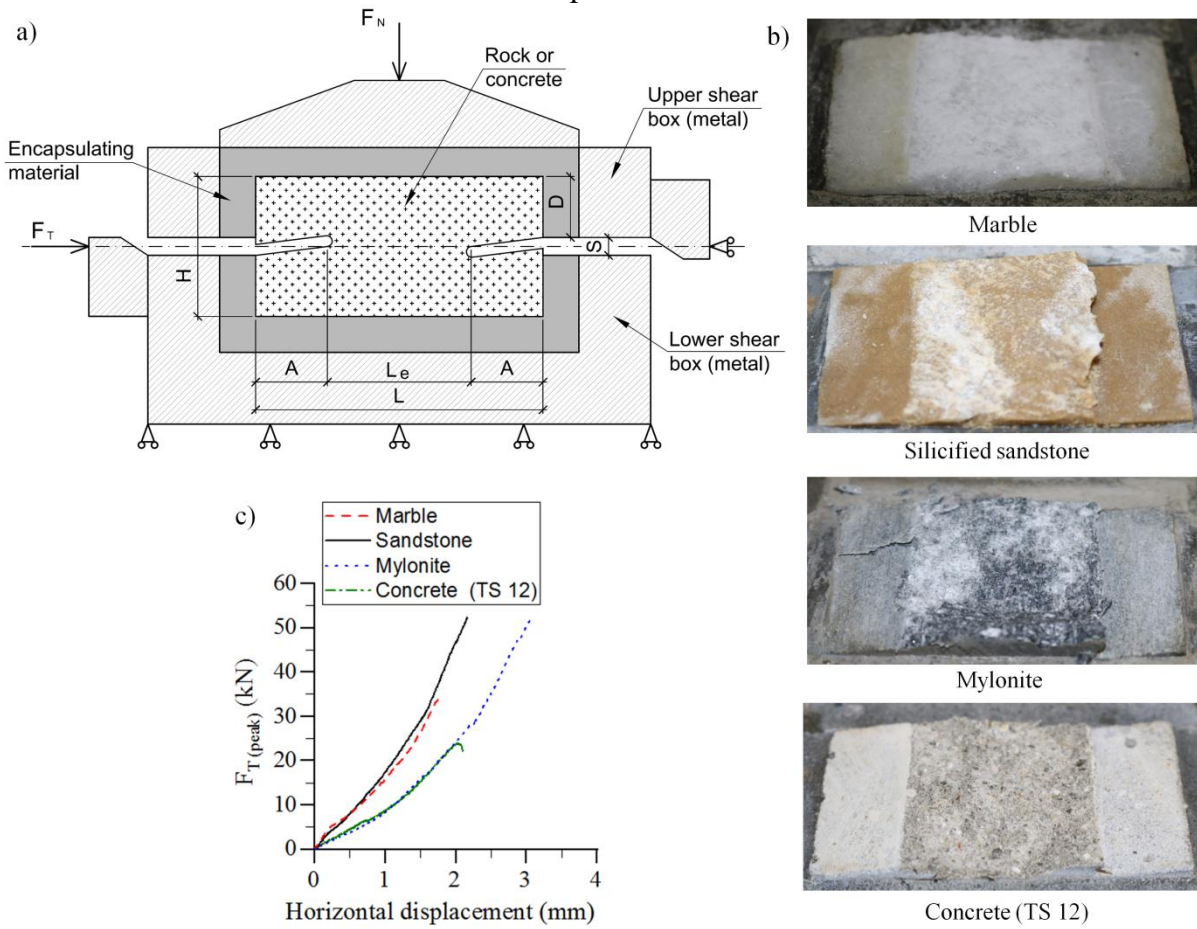
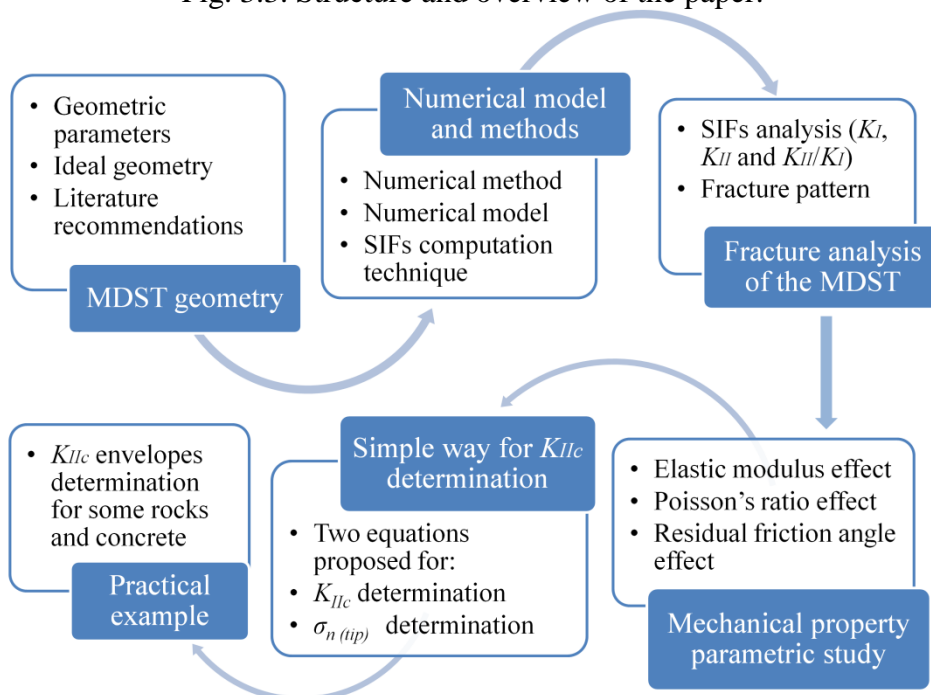


Fig. 3.3. Structure and overview of the paper.



3.2 MDST GEOMETRY

The geometric parameters of the MDST are illustrated in Fig. 3.2a, where: L is the length, W is the width H is the height, α is the small angle of the inclined notches, A is the horizontal length, T is the thickness, L_e is the effective length and S is the free space formed between the upper and the lower part of the encapsulating material.

The ideal geometry of the MDST was proposed in Chapter 2, as shown in Table 3.1. These parameters meet the recommendations of the ASTM D5607-16 (2016), *Performing Laboratory Direct Shear Strength Tests of Rock Specimens Under Constant Normal Force*.

Table 3.1 - Ideal geometry of the MDST

Geometrical parameters										
L	A	L_e	W	H	α	S	D	T	L_e / W	Area
(cm)	(cm)	(cm)	(cm)	(cm)	(°)	(cm)	(cm)	(cm)		(cm ²)
8.00	2.00	4.00	5.00	5.00	7.00	0.50	1.70	0.30	0.80	20.00

Analyzing the ideal geometry against the recommendations for mode II fracture toughness tests reported in the literature, we note:

- a) specimen size (L_e): the measured K_{IIc} is not so strongly dependent on the specimen size (LAQUECHE; ROUSSEAU; VALENTIN, 1986; SUN; WHITTAKER; SINGH, 1990) and the specimen size requirements seem to be unnecessary for mode II measurements (WHITTAKER; SINGH; SUN, 1992). Traditionally in rock mechanics, a simple ratio between the specimen size and the grain size of 10:1 has usually been deemed sufficient to guarantee the representativeness of the bulk material (ATKINSON; MEREDITH, 1987);
- b) specimen thickness (W): the measured K_{IIc} is not affected for $W \geq 4$ cm (ATKINSON, 1987);
- c) relationship between specimen size and thickness: the measured K_{IIc} is not affected for $L_e / W < 1.0$ (RAO et al., 1999).

Hence, the ideal geometry of the MDST meets these recommendations published in the literature for mode II fracture toughness test.

The MDST test procedures follow the ASTM D5607-16 (2016) recommendations and are detailed in Chapter 2.

3.3 NUMERICAL METHODS AND MODEL

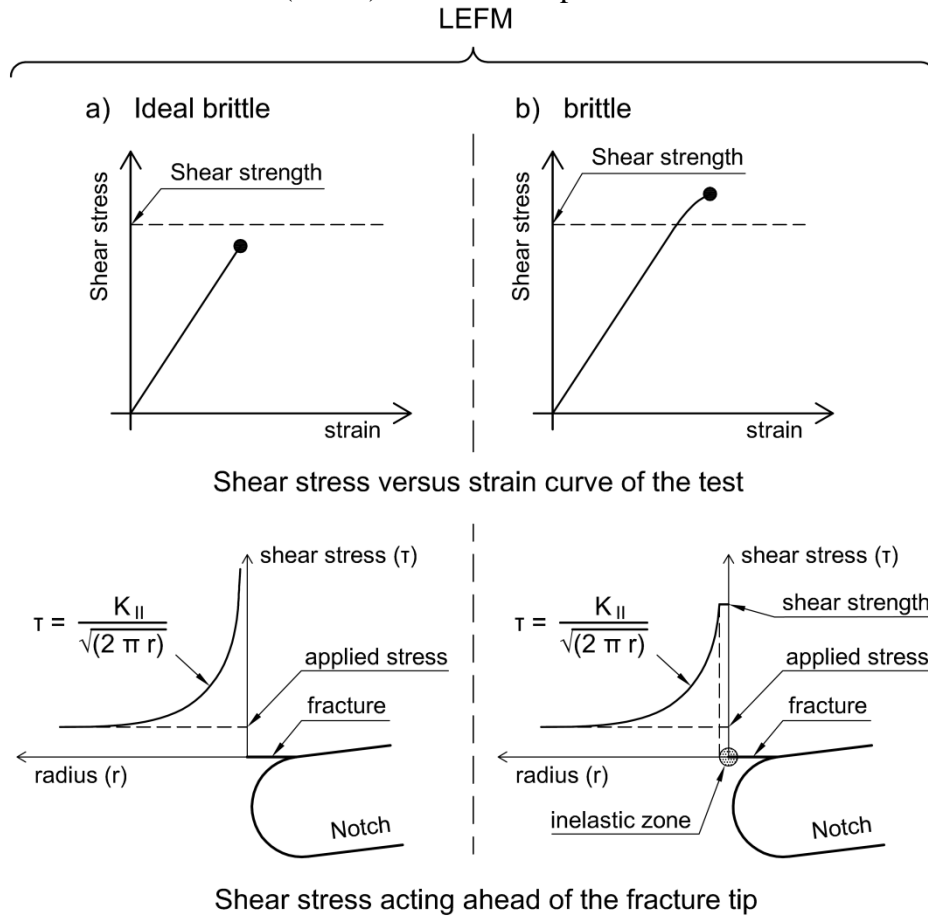
The numerical methods, model and SIFs computation technique used in this research are presented in this section.

3.3.1 NUMERICAL METHOD

The numerical analysis was performed using the Finite Element Method through the Abaqus 6.14 program, developed by Dassault Systèmes Simulia Corp., coupled with the FRANC3D program, developed by Fracture Analysis Consultants, Inc. The function of FRANC3D is to include the initial fracture into the model created in the Abaqus, to compute the SIFs, through the LEFM and to propagate the fracture using the re-meshing technique.

LEFM is ideally formulated to describe the ideally brittle fracture, where the stress, strain and displacement can be uniquely characterized by the SIFs (K_{II} in this example), as shown in Fig. 3.4a. However, it can be applied to brittle fractures (Fig. 3.4b) when the nonlinear behavior of the material is limited to a zone near the mesofracture tip and it is considered small compared to the specimen size (often referred to as small-scale yielding). Therefore, the nonlinear behavior can be ignored and the material is considered linear elastic (WHITTAKER; SINGH; SUN, 1992). For mode II fracture analysis, there are no analytical criteria in the literature to check the small-scale yielding to guarantee the validity of the LEFM, therefore, the validation of the LEFM was based on the typical force versus displacement curves of the MDST, which presented an approximately linear behavior with abrupt rupture (see again Fig. 3.2b).

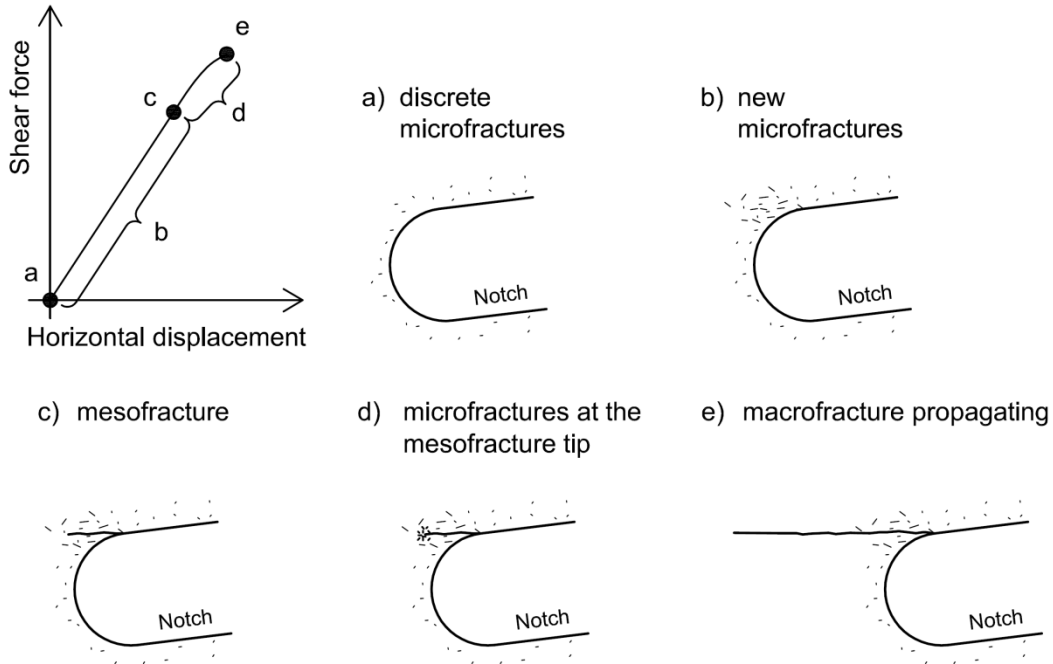
Fig. 3.4. Applicability of the LEFM: a) ideal brittle and b) brittle behavior. Schematic illustration of shear stress versus strain curves of the test (MDST) and shear stress acting ahead ($\theta = 0^\circ$) the fracture tip for mode II.



The fracture formation process for the MDST can be inferred based on previous studies in the literature with others fracture modes, such as mode I, mixed mode I+II or mode II without normal stresses, since there are no studies of the fracturing process for mode II with normal stress application (LIN; LABUZ, 2013; LIN et al., 2018; LI; REN; YU, 2020; MOAZZAMI; AYATOLLAHI; AKHAVAN-SAFAR, 2020 and others). Initially, the material contains discrete microfractures (about 10^{-6} m) naturally formed or caused by the notch cutting process (Fig. 3.5a). The specimen is loaded and new microfractures are formed, starting the fracture process zone (FPZ) (Fig. 3.5b). At a high load level, reaching the material strength, microfractures extend and link to the other adjacent microfractures, forming a mesofracture (about 10^{-3} m) (Fig. 3.5c). LEFM can be applied at this stage, when there is a stable mesofracture formed and the SIFs can be computed. Increasing the load, new microfractures are formed at the mesofracture tip (in a very small region), that can be ignored (Fig. 3.5d). The mesofracture is stable until the SIFs reach the fracture toughness of the material; after this, the mesofracture propagates in an unstable manner (abrupt rupture)

forming a macrofracture (about 10^{-1} m) (Fig. 3.5e). The fracture toughness of the material is the SIFs computed at the moment of transition from the stable to the unstable condition (usually occurring at the peak of the force versus displacement curve, approximately).

Fig. 3.5. Schematic illustration of the development of the fracture process zone in brittle materials applied to the MDST.

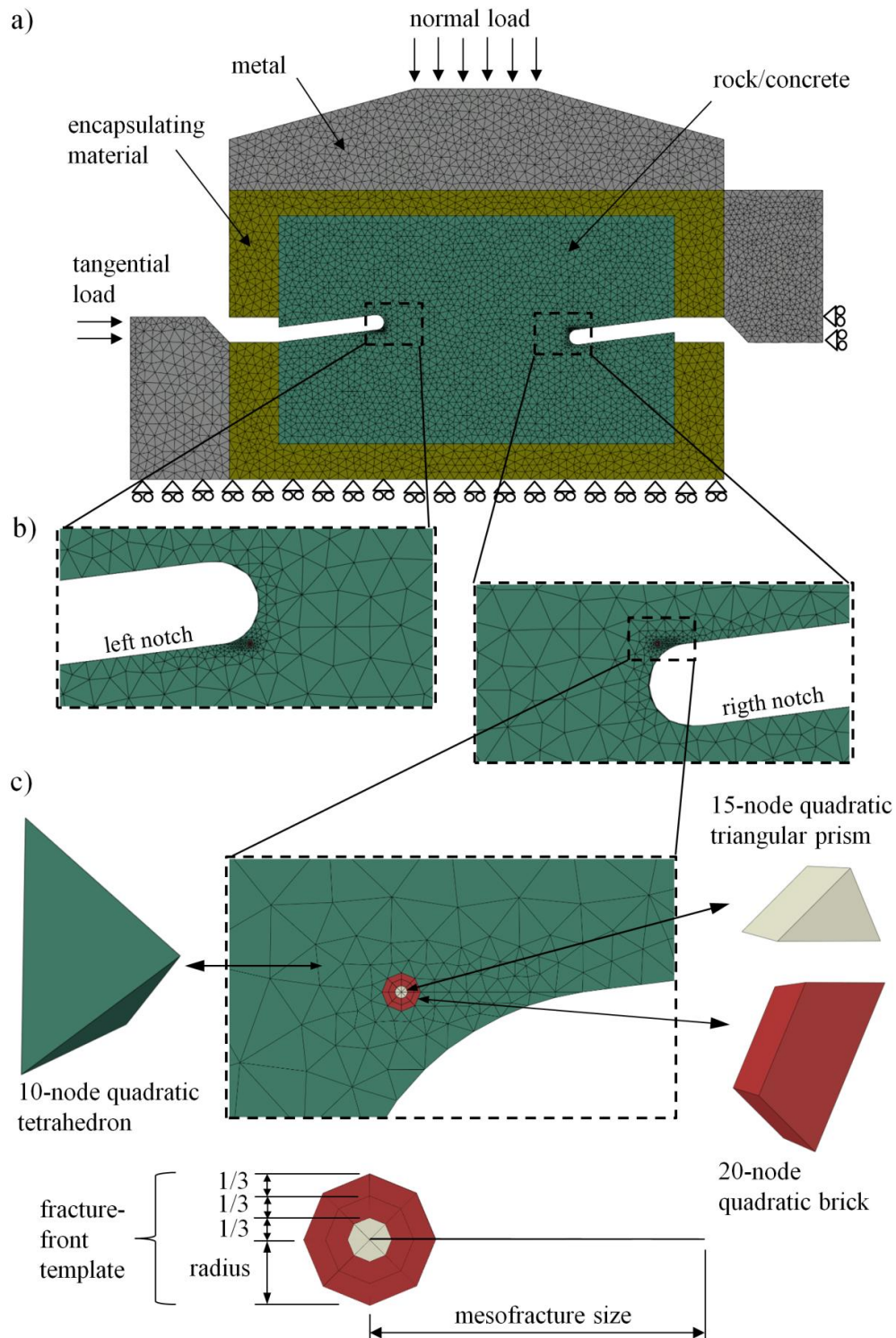


3.3.2 NUMERICAL MODEL

The geometry, loads, boundary conditions and mesh of the MDST models are shown in Fig. 3.6a. The models were created with reduced thickness ($W = 0.5$ cm), to reduce the computational cost. Displacements in direction 3 (perpendicular to the drawing) were restricted throughout the model to simulate the plane strain occurring in the central region of the specimen (where the fracture propagation is pronounced). The analyses were static and they were carried out in two steps (normal stress application and shear stress application).

Two mesofractures were inserted in the model to simulate the FPZ, one below the left notch tip and other above the right notch tip (Fig. 3.6b). In these places, the shear stress and confined compression concentrate and fracture occurs (see Chapter 2). The FPZ is dependent on the geometry of the TS, the material and the type of loading performed, so it is a difficult phenomenon to predict in new tests (BROOKS, 2013; MOAZZAMI; AYATOLLAHI; AKHAVAN-SAFAR, 2020). The mesofracture size was adopted at 1 mm, and the fracture-front template radius was 10% of its size (0.1 mm). Different mesh elements were used to model the fracture and fracture-front template (Fig. 3.6c).

Fig. 3.6. MDST numerical model: a) geometry, loads, boundary conditions and mesh; b) mesofracture places and c) details of the mesofracture.



3.3.3 SIFs COMPUTATION TECHNIQUE

The Virtual Crack Closure Technique (VCCT), proposed by RYBICKI; KANNINEN (1977), was chosen to compute the stress intensity factors. The VCCT consists of a modification of Irwin's closure integral (IRWIN, 1958). Irwin's proposal is based on the

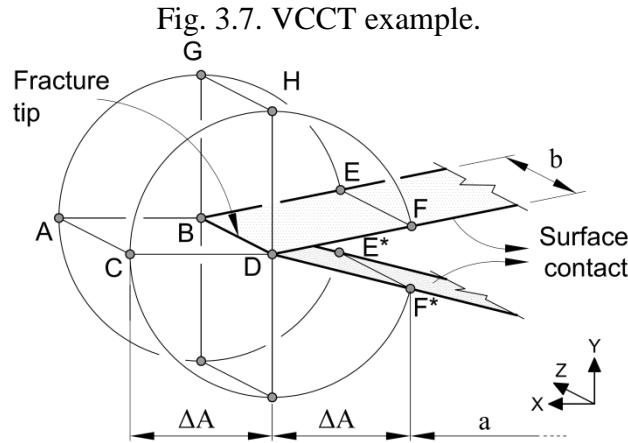
hypothesis that the released energy during fracture extension is the same as the amount of work required to close the fracture in the same extension and the stress field behind the fracture tip can be approximated with the stress field ahead of the fracture tip for an infinitesimal value of extended fracture.

The strain energy release rate (also called fracture energy) is obtained in mode I and II components separately, with a single step of analysis, multiplying the fracture face displacements behind the fracture tip by stress resultants ahead of the fracture tip, dividing by 2 and the element area (Fig. 3.7):

$$G_I = \frac{1}{2b\Delta a} \int_0^b \int_0^{\Delta a} \sigma_{yy} u_y dx dz \quad (3.1)$$

$$G_{II} = \frac{1}{2b\Delta a} \int_0^b \int_0^{\Delta a} \sigma_{xy} u_x dx dz \quad (3.2)$$

where Δa is the length of the element, b is the width of the element, σ_{xy} and σ_{yy} are the stresses in ABCD surface (in front of the fracture tip), u_x and u_y are the relative displacements between BDEF and BDE*F* surfaces (behind of the fracture tip), as shown in Fig. 3.7.



The stress intensity factors for each mode can be obtained by the relationship proposed by IRWIN (1958):

$$K_I = \sqrt{G_I E^*} \quad (3.3)$$

$$K_{II} = \sqrt{G_{II} E^*} \quad (3.4)$$

where $E^* = E$ for plane stress and $E^* = E/(1-\nu^2)$ for plane strain. E is the elastic modulus and ν is the Poisson's ratio.

The surface contact of the fracture (gray hatched region of Fig. 3.7) is governed by hard contact (normal behavior), which does not allow penetration of surfaces, and residual friction coefficient (tangential behavior).

The Maximum Shear Stress (MSS) criterion was chosen to define the kink angle of fracture propagation. The MSS criterion states that the crack will grow in the direction that maximizes the resolved shear stress (FRACTURE ANALYSIS INC., 2015).

3.4 FRACTURE ANALYSIS OF THE MDST

The fractures analysis of the MDST comprises a first understanding of the typical stress intensity factors and fracture pattern of the MDST.

Some numerical models are generated with the ideal geometry of the MDST and using typical stress state and mechanical properties of the materials. Three models were simulated with average normal stresses ($\sigma_n (av) = 1.0, 5.0$ and 10.0 MPa) and average peak shear stresses ($\tau_{peak (av)} = 8.85, 12.20$ and 16.40 MPa), respectively. The mechanical properties of the materials are shown in Table 3.2. Obs.: This work follows the geotechnical convention, that is, positive signs refer to compression and negative signs refer to tensile.

Table 3.2 - Mechanical properties of materials

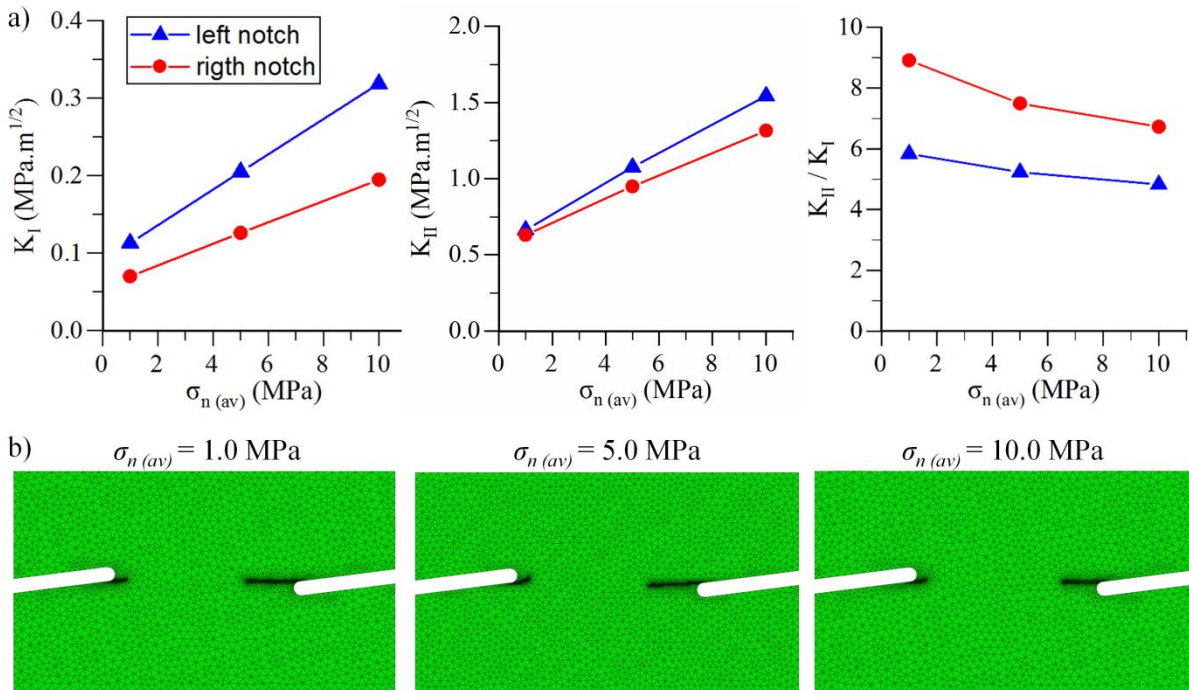
Materials	E (GPa)	ν	Residual friction angle (ϕ_{res}) (°)
Rock	30.00	0.20	30.00
Metal (steel 304)	193.00	0.27	-
Encapsulating material	35.00	0.20	-

Fig. 3.8a shows the SIFs results (K_I , K_{II} and K_{II} / K_I ratio). The right notch showed lower K_I and the left notch showed slightly higher K_{II} . In the right notch, K_{II} / K_I ratio is higher, around 7 to 9, which is equivalent to $G_{II} / G_I = 60$ to 80 . In other words, mode II fracture energy is about 70 times greater than mode I fracture energy, indicating that the fracture probably propagates in this notch and predominantly in mode II (shear fracture).

The confirmation of the fracture propagation place (left or right notch) is essential for computing fracture toughness, because the stress intensity factor is different in each notch. In addition, an important information is the direction of the fracture propagation. Therefore, the fracture was propagated in the model for the three average normal stresses (Fig. 3.8b). In the three models, the fracture did not propagate until the end of the TS because there was a numerical error; however, it can be observed that: a) in the left notch, the fracture presents

upward inclination (due to the tensile influence) and did not propagate and b) in the right notch, the fracture propagates horizontally (where the highest G_{II} / G_I ratio). At this point, two important conclusions can be drawn: a) the K_{IIc} must be determined in the right notch where the fracture has propagated and b) the horizontal fracture in MDST is due to shear, because the kink angle of fracture propagation criterion used was the MSS criterion. Thus, the next studies in this work considered the mesofracture located only at the top of the right notch tip and K_{IIc} was obtained in this place.

Fig. 3.8. Fracture analysis of MDST: a) K_I , K_{II} and K_{II} / K_I ratio and b) fracture propagation for: $\sigma_{n(av)} = 1.0$ MPa, $\sigma_{n(av)} = 5.0$ MPa and $\sigma_{n(av)} = 10.0$ MPa.



3.5 MECHANICAL PROPERTY PARAMETRIC STUDY

A parametric study was carried out to investigate the influence of the mechanical properties on K_{IIc} determination. The mechanical properties involved in the simulation depend only on the elastic properties and residual friction angle of the material. Thus, the elastic modulus, Poisson's ratio and residual friction coefficient, were varied (Table 3.3). The stresses applied were $\sigma_{n(av)} = 5.0$ MPa and $\tau_{peak(av)} = 12.2$ MPa. Fig. 3.9 shows the results.

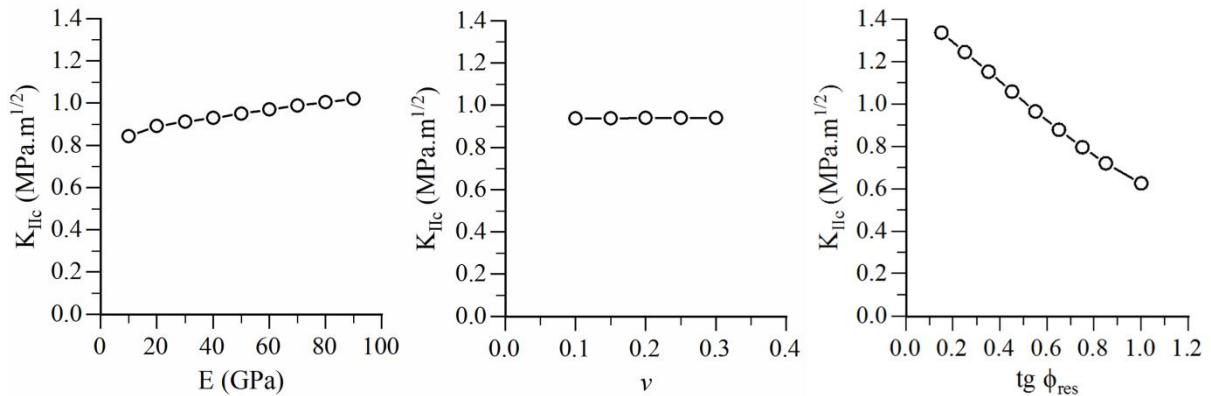
Analyzing Fig. 3.9, it is noted that for this particular study: a) K_{IIc} increases little as E increases; b) K_{IIc} does not depend on Poisson's ratio and c) K_{IIc} greatly reduces as ϕ_{res} increases. The significant influence of the ϕ_{res} is due to the microstructural asperities, where the frictional work acts as an additional energy sink, reducing the amount of energy available

to drive the fracture tip (PETROVIC, 1985; LI, 1987). Therefore, only E and ϕ_{res} were used in the next study.

Table 3.3 - Mechanical properties of parametric studie

Elastic modulus effect			Poisson's ratio effect			Residual friction coefficient effect		
E (GPa)	ν	$\text{tg}(\phi_{res})$	E (GPa)	ν	$\text{tg}(\phi_{res})$	E (GPa)	ν	$\text{tg}(\phi_{res})$
10.00	0.20	0.58	45.00	0.10	0.58	45.00	0.20	0.15
20.00	0.20	0.58	45.00	0.15	0.58	45.00	0.20	0.25
30.00	0.20	0.58	45.00	0.20	0.58	45.00	0.20	0.35
40.00	0.20	0.58	45.00	0.25	0.58	45.00	0.20	0.45
50.00	0.20	0.58	45.00	0.30	0.58	45.00	0.20	0.55
60.00	0.20	0.58				45.00	0.20	0.65
70.00	0.20	0.58				45.00	0.20	0.75
80.00	0.20	0.58				45.00	0.20	0.85
90.00	0.20	0.58				45.00	0.20	1.00

Fig. 3.9. Mechanical property parametric study: a) elastic modulus effect; b) Poisson's ratio effect and c) residual friction coefficient effect.



3.6 A SIMPLE WAY FOR K_{IIc} DETERMINATION

In this section, a simple way was proposed for determining K_{IIc} in function of the confining pressure through two equations based on numerical analysis.

To compose a large number of numerical analysis, some variables were selected to encompass typical rock and concrete mechanical properties and strength: i) 4 peak shear strength envelopes (the shear strength envelopes are used only to define the average peak shear stress at the rupture for each average normal stress), as shown in Table 3.4; ii) 7 average normal stresses (1, 5, 10, 20, 30, 60 and 120 MPa); iii) 4 elastic modulus (10, 35, 60 and 85 GPa); and iv) 3 residual friction angle (20, 35 and 50°). A combination is made with these variables resulting in 336 numerical models.

Table 3.4 - Shear strength envelopes

Envelopes	Cohesion (c') (MPa)	Peak friction angle (ϕ_{peak}) (°)
1	5.00	35.00
2	10.00	50.00
3	15.00	65.00
4	20.00	80.00

The results are plotted in Fig. 3.10, where K_{IIc} is normalized with $\sigma_{n(av)}$ and $\tau_{peak(av)}$ with $\sigma_{n(av)}$. A single potential function can be observed for all peak shear strength envelopes and a different potential function for each E and ϕ_{res} . Eq. 3.5 ($R^2 = 0.998$) was proposed to determine K_{IIc} interpolating all cases. The equation is function of $\sigma_{n(av)}$, $\tau_{peak(av)}$ and ϕ_{res} obtained in the experimental tests of the MDST (as shown in Chapter 2) and the E estimated in the literature. The equation can be applied for $\tau_{peak(av)} / \sigma_{n(av)} < 30$.

$$K_{IIc} = \sigma_{n(av)} A \left(\frac{\tau_{peak(av)}}{\sigma_{n(av)}} \right)^B \quad (3.5)$$

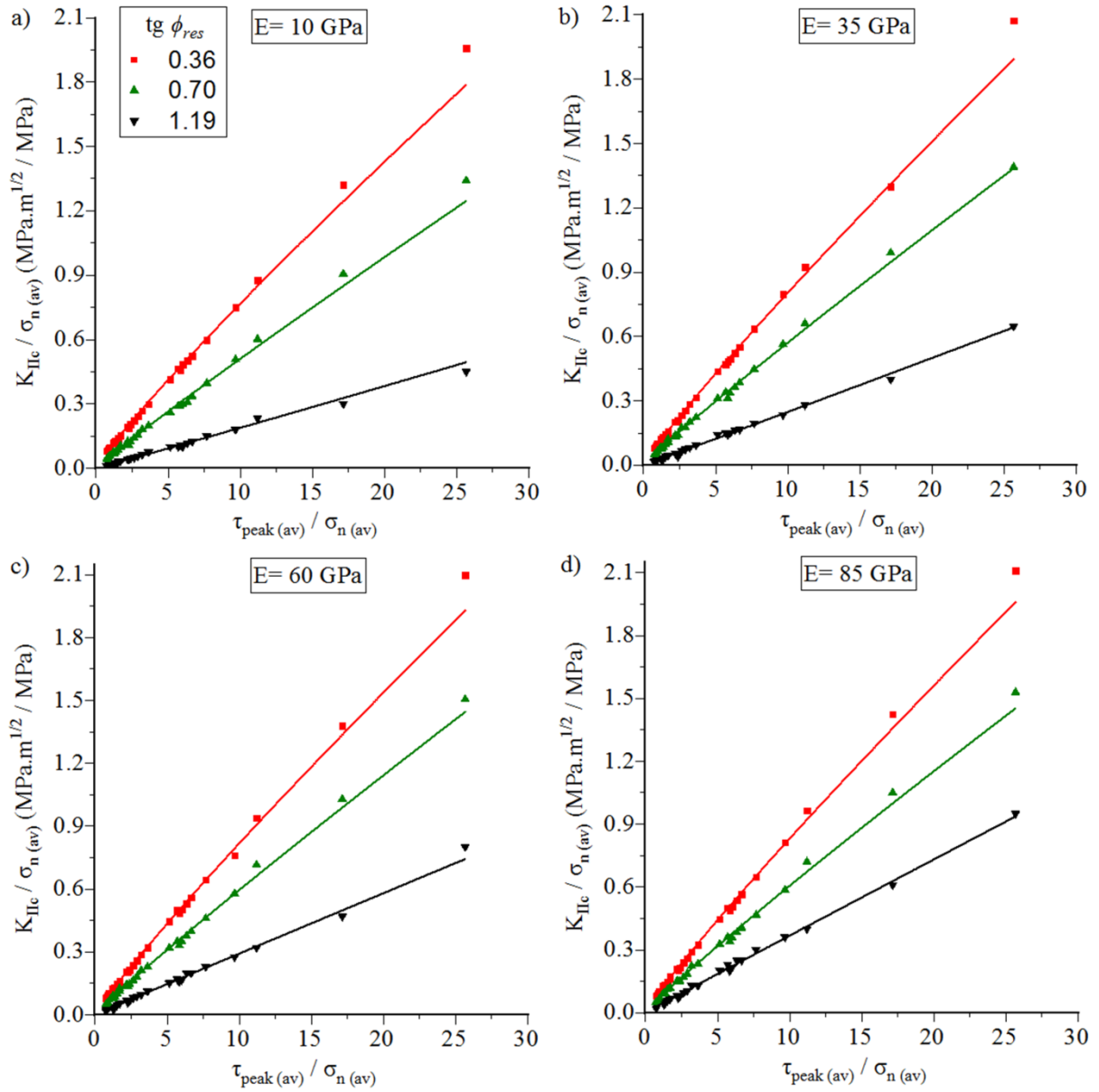
$$A = [(0.0002 E - 0.0849)(tg \phi_{res}) + 0.1189]$$

$$B = [0.9542 - 0.0624(tg \phi_{res})]$$

where K_{IIc} is in $\text{MPa}\cdot\text{m}^{1/2}$, $\tau_{peak(av)}$ and $\sigma_{n(av)}$ are in MPa, E is in GPa and ϕ_{res} is in degree/radians.

As mentioned in the introduction, K_{IIc} strongly depends on the confining pressure. All studies present in the literature of K_{IIc} determination consider the confining pressure as the average normal stress ($\sigma_{n(av)}$), even if the normal stress is heterogeneous across the shear area of the TS. However, we believe that it is right to consider the normal stress acting on the right notch, and more specifically, at the fracture tip, where K_{IIc} is computed. Therefore, the confining pressure was considered here the vertical stress acting in front of the mesofracture tip (centroid of ABCDGH volume of Fig. 3.7) in the right notch ($\sigma_{n(tip)}$).

Fig. 3.10. K_{IIc} determination for: a) $E = 10$ GPa; b) $E = 35$ GPa; c) $E = 60$ GPa and d) $E = 85$ GPa.



Using the same numerical models, $\sigma_n(tip)$ was obtained for all models and are shown in Fig. 3.11. The same observations made for K_{IIc} apply to $\sigma_n(tip)$. Eq. 3.6 ($R^2 = 0.997$) was proposed to determine $\sigma_n(tip)$. The equation can be applied for $\tau_{peak(av)} / \sigma_n(av) < 30$.

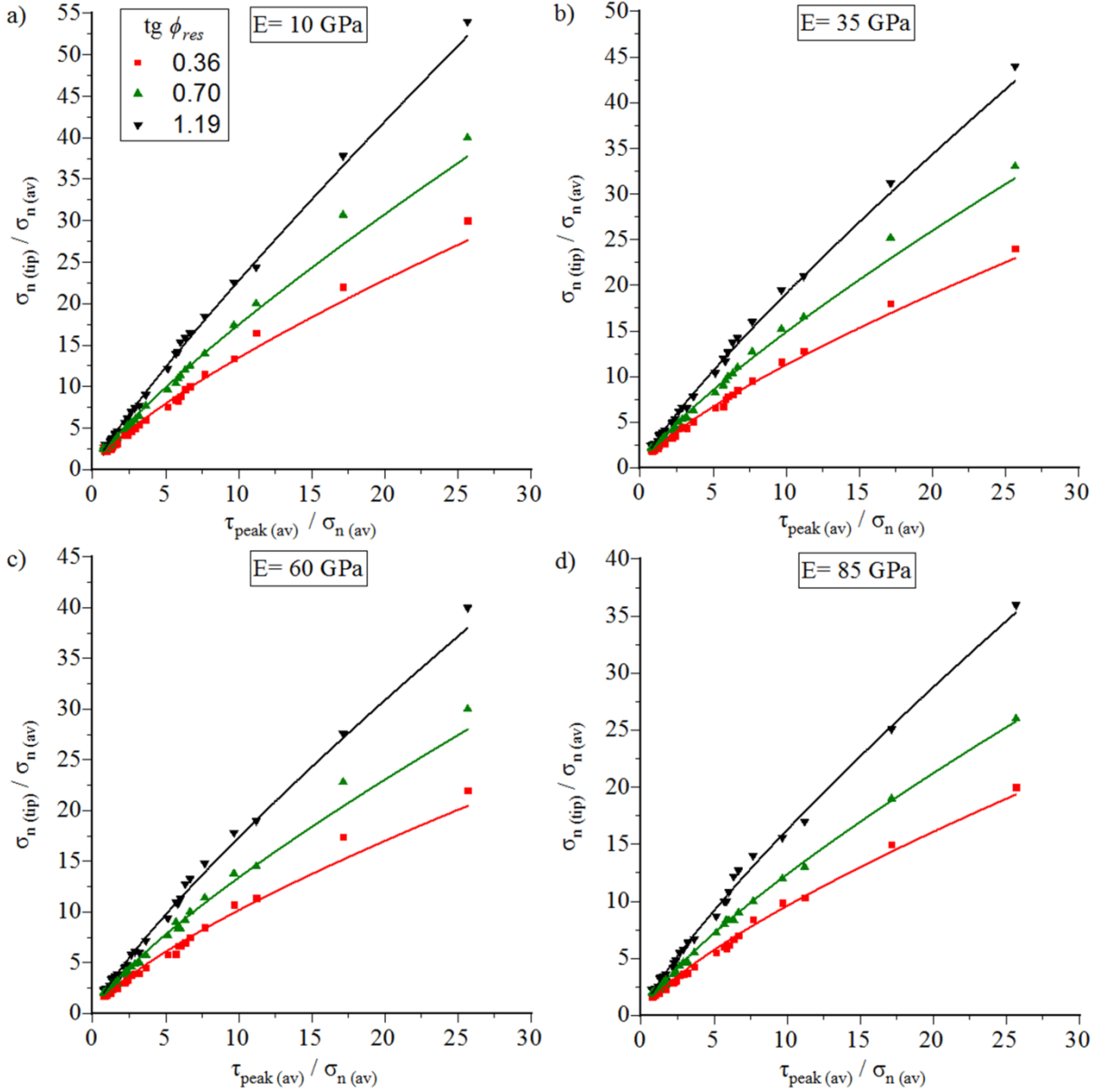
$$\sigma_n(tip) = \sigma_n(av) A \left(\frac{\tau_{peak(av)}}{\sigma_n(av)} \right)^B \quad (3.6)$$

$$A = [(2.028 - 0.0054 E) + 0.7915(tg \phi_{res})]$$

$$B = [(0.7244 - 0.0014 E) + 0.1461(tg \phi_{res})]$$

where $\sigma_n(tip)$, $\sigma_n(av)$ and $\tau_{peak(av)}$ are in MPa, E is in GPa and ϕ_{res} is in degree/radians.

Fig. 3.11. $\sigma_n (tip)$ determination for: a) $E = 10$ GPa; b) $E = 35$ GPa; c) $E = 60$ GPa and d) $E = 85$ GPa.



Therefore, using Eq. 3.5 and 3.6, K_{IIc} and $\sigma_n (tip)$ can be obtained for each test and K_{IIc} envelope of the material can be obtained performing some tests.

3.7 PRACTICAL EXAMPLE AND VALIDATION OF EQUATIONS

A practical example of the method application was provided using the experimental testes performed in Chapter 2 in homogeneous rocks (marble, silicified sandstone and mylonite) and concrete. Only experimental tests that showed shear ruptures were used. Table 3.5 shows the TSs and their experimental results ($\sigma_n (av)$, $\tau_{peak (av)}$ and ϕ_{res}). Only five concrete TSs were used, as there is no need to use all those tested. The elastic modulus of the rocks and

concrete were estimated based on the literature. K_{IIc} and $\sigma_n (tip)$ were calculated by Eq. 3.5 and 3.6.

Table 3.5 - K_{IIc} and $\sigma_n (tip)$ determination using Eq. 3.5 and 3.6

Material	Experimental results					K_{IIc} (MPa.m ^{1/2})	$\sigma_n (tip)$ (MPa)
	TS	$\sigma_n (av)$ (MPa)	$\tau_{peak (av)}$ (MPa)	ϕ_{res} (°)	E (GPa)		
Marble	M1	1.00	9.30			0.49	15.15
	M2	5.00	16.24			0.93	32.29
	M3	10.00	25.13			1.48	52.65
	M4	15.00	32.28			1.92	69.68
Silicified sandstone	S2	5.00	26.83			1.26	50.58
	S3	10.00	24.62	37.9	15.00	1.25	53.51
	S4	15.00	33.39			1.71	73.93
Mylonite	My2	5.00	26.72			1.42	37.62
	My3	10.00	41.50	39.7	85.00	2.26	62.61
	My4	15.00	50.39			2.80	80.55
Concrete	7	0.50	7.47			0.44	8.9
	9	1.00	7.83			0.49	10.91
	12	5.00	14.76	30.0*	36.00	1.00	26.03
	13	10.00	19.45			1.36	37.94
	16	20.00	26.37			1.91	56.5

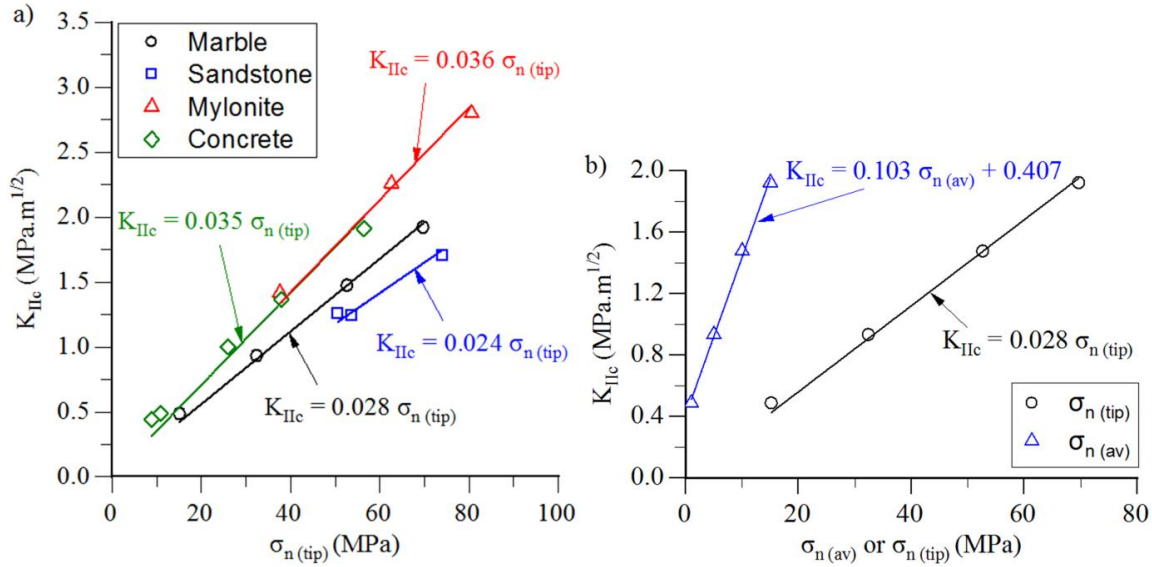
* The residual friction coefficient was adopted

Plotting K_{IIc} in function of $\sigma_n (tip)$, K_{IIc} envelopes were obtained (Fig. 3.13a). A linear equation that goes through the origin represents very well all materials. This means to infer that there is no K_{IIc} for $\sigma_n (tip)$ equal to zero. All studies in the literature present K_{IIc} for confining pressure equal to zero (e.g. RAO et al. (1999) and BACKERS; STEPHANSSON; RYBACKI (2002)). However, these studies consider the confining pressure as $\sigma_n (av)$, as previously mentioned. Considering the confining pressure as $\sigma_n (tip)$, there is probably no K_{IIc} for $\sigma_n (tip)$ equal to zero or there is a very small value. It is very difficult (or practically impossible) to obtain a experimental result for low or zero $\sigma_n (tip)$ to confirm this question, because even if normal stress is not applied at the beginning of the test, when shear stress is applied, normal stresses at the fracture tip are generated indirectly.

An example, using marble results, presents the difference between K_{IIc} envelopes considering $\sigma_n (tip)$ and $\sigma_n (av)$ (Fig. 3.13b). Due to the geometry of the MDST, the existence of the mesofracture and the application of shear stress, the $\sigma_n (tip)$ is much higher than the $\sigma_n (av)$. Note that the envelope is shifted to the right. Due to this, we cannot consider that the envelope based on $\sigma_n (tip)$ is less "resistant" than the envelope based on $\sigma_n (av)$, because it depends on the analysis method considered. Considering the confining pressure as $\sigma_n (av)$, there is a intercept

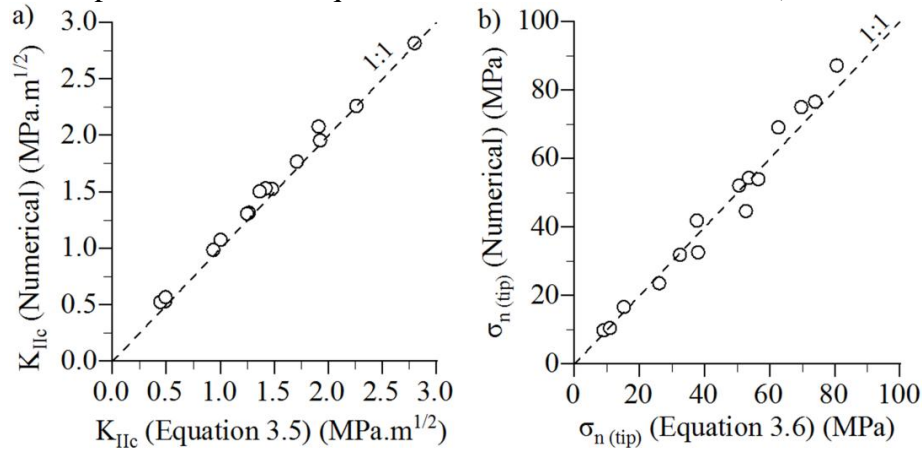
in K_{IIc} axis and a highest angular coefficient. Considering the confining pressure as $\sigma_n (tip)$, there is probably no intercept in K_{IIc} axis and a lower angular coefficient.

Fig. 3.13. a) K_{IIc} envelopes of the rocks and concrete and b) example of difference between marble K_{IIc} envelope considering $\sigma_n (tip)$ and $\sigma_n (av)$.



In order to validate the Eq. 3.5 and 3.6, the same experimental tests were used to calculate K_{IIc} and $\sigma_n (tip)$ by numerical analysis and their results were compared with the results of the equations. In the numerical analysis, the real geometries of the TSs were used. Fig. 3.12 shows a visual comparison between the results from numerical analysis e equations. Note that there is a small difference for K_{IIc} and for $\sigma_n (tip)$, were the maximum relative error was 16 % for K_{IIc} and 18 % for $\sigma_n (tip)$. The relative error is due to two aspects: a) the numerical results are not precise and b) the real geometry of the TS differs from the ideal geometry and causes small differences in the results. Although the real geometry of the TS is not considered directly in the equations, the geometry is considered indirectly when using the shear stress input instead of shear force, because the area is taken into account. However, small errors were expected and it can be concluded that the equations are valid.

Fig. 3.12. Comparison between equation and numerical results for: a) K_{IIc} and b) $\sigma_{n(tip)}$.



3.8 CONCLUSION

This paper proposed the MDST for determining K_{IIc} in function of the confining pressure of homogeneous rock and concrete. The MDST is a promising method because mode II prevails in the test, as observed experimentally and proved here numerically. The MDST uses the direct shear machine and it is intended for testing homogeneous material (with grain size up to 4 mm) in which there should be no plans of weakness or discontinuities. The following are the main conclusions:

- the MDST is suitable for determining K_{IIc} , since mode II prevails in the test (G_{II} was about 70 times of G_I in the right notch);
- Maximum Shear Stress criterion provided a good representativeness of the fracture pattern of the test and allowed us to conclude that the horizontal fracture in the MDST is due to shear (mode II). The fracture propagated from the right notch to the left;
- the ideal geometry of the MDST ($L = 8.00$ cm, $A = 2.00$ cm, $L_e = 4.00$, $W = 5.00$ cm, $\alpha = 7.00^\circ$, $T = 0.3$ cm, $S = 0.50$ cm and $D \geq 0.20 L$) meets the mode II fracture toughness test recommendations published in the literature;
- two equations were proposed to determine K_{IIc} and $\sigma_{n(tip)}$. The equations variables are the experimental results (peak and residual strength) and elastic modulus of the material. The equations must be applied only for the ideal geometry. Geometries larger than these cannot be used, even keeping the same proportion. For these cases, future works must be developed generating other constants in the equations;

- e) a practical example of the method application was provided. The K_{IIc} envelopes were obtained for some rocks and concrete. A linear equation that goes through the origin represents very well all materials. K_{IIc} for σ_n (tip) equal to zero probably does not exist or there is a very small value.
- f) the proposed equations were validated with numerical analysis for some tests in rocks and concrete and presented small relative errors.

Experimental analysis of the FPZ of the MDST is recommended for future studies to improve the numerical models for determining K_{IIc} and σ_n (tip). Methods that use an external image are not recommended, as Chapter 2 shows a difference between the fracture pattern of the borders with the central region of the TS.

4 NUMERICAL ASSESSMENT OF FACTORS INFLUENCING THE TENSILE STRENGTH OF ROCKS VIA PULL-OFF TEST

Abstract: The pull-off test (POT) is a tensile strength testing method that is widely used in concrete/mortar and was recently applied to rock mechanics. The POT can be easily performed in both the field and the laboratory. This study uses the eXtended Finite Element Method to analyze the POT fracture mechanism under different test conditions and to assess the factors influencing the tensile strength of homogeneous rock. The numerical results were validated with experimental data and a good agreement was obtained. An ideal test geometry was proposed (the depth and width of the partial core were equal to 2.5 cm and 0.4 cm, respectively). The POT can overestimate or underestimate the tensile strength of the rock, depending on the cohesive fracture energy and a correction equation was proposed for visually homogeneous rocks and concrete.

Keywords: Pull-Off Test fracture mechanism. Tensile strength. POT ideal geometry. Rock. Concrete.

This chapter has been published: VIZINI, V. O. S.; CACCIARI, P. P.; FUTAI, M. M. Numerical assessment of factors influencing the tensile strength of rocks via pull-off test. **International Journal of Geomechanics**, v. 20, n. 7, p. 1–9, 2020. doi: 10.1061/(ASCE)GM.1943-5622.0001714.

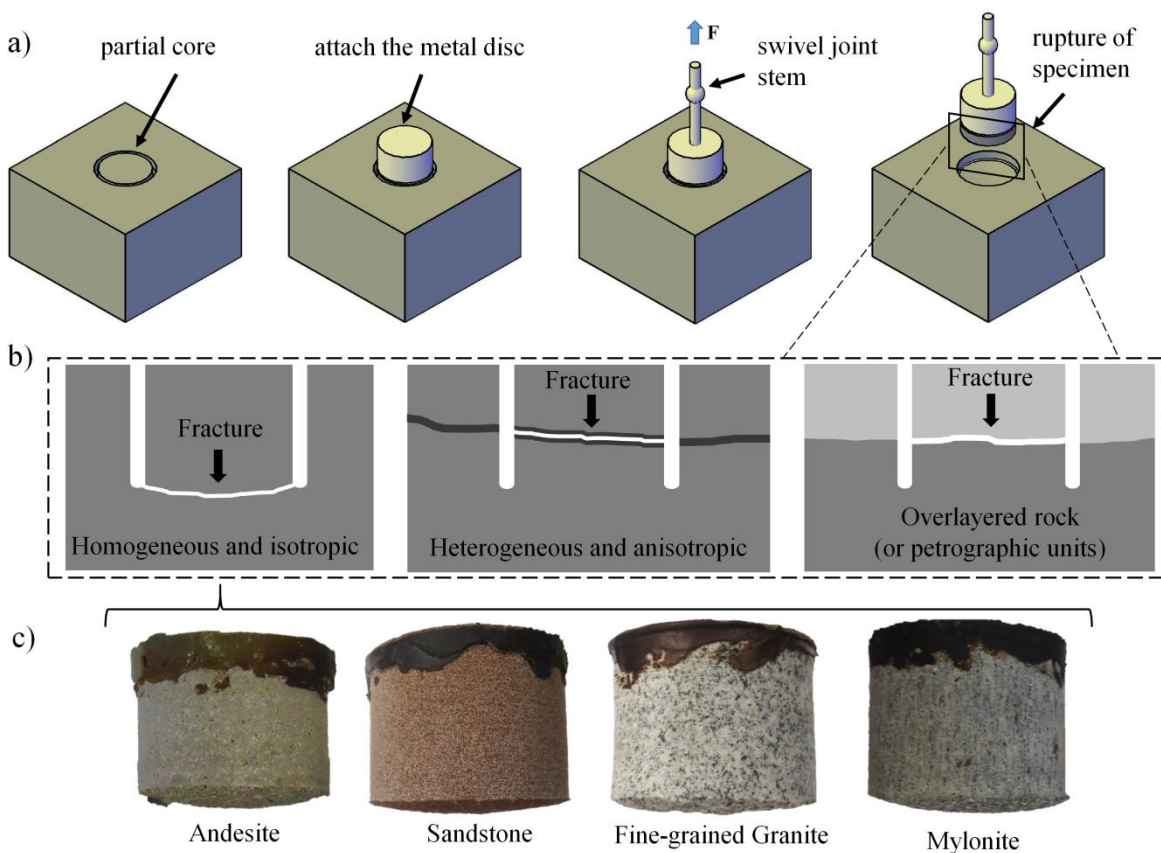
4.1 INTRODUCTION

The tensile strength of rocks is important information for many types of geotechnical projects because tensile fracture is common in most cases of rupture (HOBBS, 1964; DIEDERICHS; KAISER, 1999; and others). In addition, tensile strength is correlated with other fracture parameters, such as fracture toughness and fracture initiation (XU et al., 2018). There are some experimental test methods for determining the tensile strength of rocks, such as the direct tensile test (DTT), the Brazilian test, and so forth (PERRAS; DIEDERICHS, 2014). The pull-off test (POT) is a tensile strength testing method that is widely used in concrete/mortar and building material interfaces and was recently introduced into rock mechanics (WENG et al., 2018; CACCIARI; FUTAI, 2018). The POT can be easily performed in both the field and the laboratory, but the major advantage of the POT is its applicability in the field. The POT consists of the following steps: i) create a partial core using a circular drill bit; ii) attach a metal disc onto the top of the test specimen (TS) with an epoxy adhesive; and iii) couple a swivel joint metal stem to apply the tensile force until rupture occurs (Fig. 4.1a). The POT tensile strength (σ_t^{POT}) is calculated as the ratio between the rupture force and the cross-sectional area of the TS (ASTM, 2004).

Previous studies evaluated some factors that influence the POT. BUNGEY; MADANDOUST (1992) noted that the partial core concentrates the tensile stress at the base,

and the tensile strength decreases with increasing depth of the partial core to 2.0 cm; moreover, disc material with a thickness greater than 20 mm and diameter of 50 mm does not affect the tensile stress at the base of the partial core. AUSTIN; ROBINS; PAN (1995) verified that the stress concentration at the partial core peripheries is significantly reduced at approximately 10–15 mm above the core base. COURARD et al. (2014) evaluated the misalignment of the partial core and concluded that at up to 4° (detectable by the human eye), there was no significant change in the stress field and failure mode. CACCIARI; FUTAI (2018) performed experimental tests and concluded that in homogeneous and isotropic rock, most surface fractures occur at the base of the partial core in a concave surface (Fig. 4.1b); in addition, the POT underestimates the tensile strength by approximately 12% compared with the DTT. In heterogeneous and anisotropic rock and overlayered rock (or petrographic units), most surface fractures occur in the weakest region or along the contact between rock units (Fig. 4.1b), and the POT does not significantly underestimate the tensile strength, unless the fracture surface is close to the base of the partial core (approximately 1.0 cm).

Fig. 4.1. a) POT execution steps, b) modes of rupture (adapted from CACCIARI; FUTAI (2018)) and c) examples of concave fracture surfaces in homogeneous rocks.



Based on previous studies, there is a consensus that the partial core influences the POT results, especially in homogeneous materials in which the fracture surface occurs at the

base of the partial core, forming a concave fracture shape. There are other experimental examples for homogeneous rocks with concave fracture surfaces, such as andesite, sandstone, fine-grained granite and mylonite (Fig. 4.1c).

However, only elastic linear analyses of the POT have been reported in the literature, and no theoretical studies have investigated the POT fracture mechanism or the effect of the partial core on the determination of the tensile strength.

The aim of the present work is to analyze the POT fracture mechanism under different test conditions, through the eXtended Finite Element Method (XFEM), to assess the factors influencing the tensile strength of homogeneous rock. Parametric studies were carried out on geometrical and mechanical properties to evaluate the effects of the POT variables, and the simulations were validated with the experimental data provided by CACCIARI; FUTAI (2018).

4.2 POT NUMERICAL MODEL AND METHOD

Numerical simulations of the POT fracture process were performed using the XFEM implemented in the Abaqus 6.12 program, developed by Dassault Systèmes Simulia Corp.

4.2.1 XFEM AND FRACTURE INITIATION AND PROPAGATION CRITERIA

The XFEM was first introduced by BELYTSCHKO; BLACK (1999) by joining the concepts of the finite element method with the partition of unity theorem, which was developed by MELENK; BABUŠKA (1996), to solve differential equations with discrete functions intended for simulating fracture initiation and propagation along an arbitrary path without remeshing. There are many recent applications of XFEM in geomechanics, from laboratory test (XU et al., 2018; XIE et al., 2017; FERESTADE; HOSSEINI TEHRANI; HEIDARY, 2017; and others) to construction (FU et al., 2019; WANG et al., 2018; DEB; GUJJALA, 2018; and others).

As shown in Eq. 4.1, the approximation of the vector displacement function (δ) is composed of the terms T1 and T2, which refer to the continuous part, and the terms T3 and T4, which refer to the discontinuous part, or enriched terms (MOËS; DOLBOW; BELYTSCHKO, 1999).

$$\delta = \sum_{I=1}^N \overbrace{N_I(x)}^{T1} \left[\overbrace{\delta_I}^{T2} + \overbrace{H(x)a_I}^{T3} + \overbrace{\sum_{\alpha=1}^4 F_{\alpha}(x)b_I^{\alpha}}^{T4} \right] \quad (4.1)$$

$$H(x) = \begin{cases} 1 & \text{if } (x - x^*)n \geq 0 \\ -1 & \text{if } (x - x^*)n < 0 \end{cases} \quad (4.2)$$

where $N_I(x)$ is the usual nodal shape function; δ_I is the usual nodal displacement vector associated with the continuous part; $H(x)$ is the discontinuous jump function across the fracture surfaces (Eq. 4.2); a_I is the product of the nodal enriched degree of freedom vector; $F_{\alpha}(x)$ are the elastic asymptotic fracture-tip functions; b_I^{α} is the product of the nodal enriched degree of freedom vector; x is the Gaussian point; x^* is the point on the fracture closest to x ; and n is the unit outward normal to the fracture at x^* (SYSTÈMES, 2012).

To describe the initiation and propagation of a fracture, the cohesive zone model (CZM) (BARENBLATT, 1959; DUGDALE, 1960; BARENBLATT, 1962) is adopted in this study. The CZM is a highly recommended approach for investigating the fracturing of quasibrittle materials that have not been previously fractured (ELICES et al., 2002).

The elements and nodes enriched by the CZM do not depend on the T4 term, because the approach does not calculate the displacement at the crack tip; instead, they use only terms T1 through T3 of Eq. 4.1, as illustrated in Fig. 4.2a. The fracturing of a cohesive element is divided into four phases: 1st - elastic; 2nd - fracture initiation; 3rd - fracture propagation; and 4th - rupture (Fig. 4.2b).

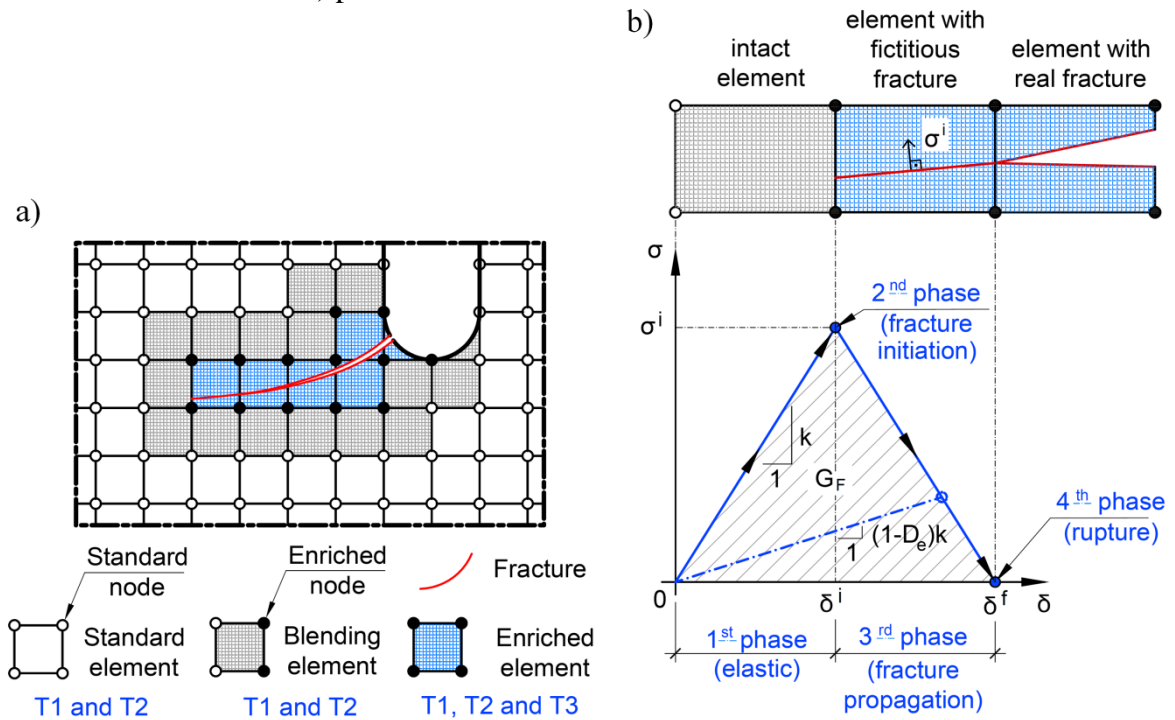
The first phase is based on the stress versus separation behavior, which applies to the linear elastic regime up to the point at which the material does not display fractures (remains an intact element), as expressed by Eq. 4.3 and illustrated in Fig. 4.2b.

$$\sigma = \begin{Bmatrix} \sigma^n \\ \sigma^s \\ \sigma^t \end{Bmatrix} = \begin{bmatrix} k^{nn} & 0 & 0 \\ 0 & k^{ss} & 0 \\ 0 & 0 & k^{tt} \end{bmatrix} \begin{Bmatrix} \delta^n \\ \delta^s \\ \delta^t \end{Bmatrix} = k\delta \quad (4.3)$$

where σ is the stress, k is the stiffness of the material, and δ is the displacement. The subscript n refers to the normal direction, and s and t refer to the two tangential directions.

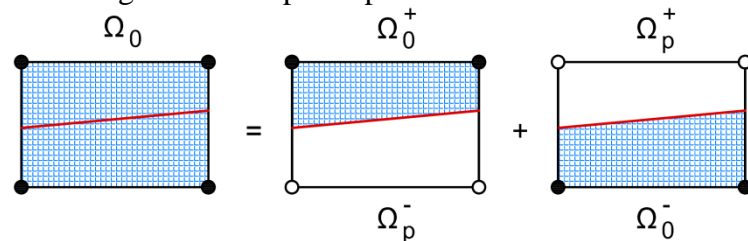
In the second phase, the fracture initiates. When the acting maximum principal stress reaches the fracture initiation stress (σ^i), a fictitious fracture is created that crosses the entire element in a direction orthogonal to the maximum principal stress (Fig. 4.2b). The value of σ^i for a brittle and quasibrittle material is often considered equal to the tensile strength obtained in the DTT (σ_t^{DTT}).

Fig. 4.2. a) Example of XFEM elements and nodes based on the CZM applied to the POT and b) phases in which a cohesive element fractures.



In the third phase, the fracture propagates (Fig. 4.2b), and the CZM requires the use of a second method to calculate the displacements (the T3 term); this method is called the phantom nodes method (RABCZUK et al., 2008). This technique represents the discontinuity of the fractured element through the creation of a phantom domain (Ω_p) and an original domain (Ω_0), in which the phantom nodes and original nodes are superimposed and mutually constrained when the element is intact and free to separate when a fracture splits the element (Fig. 4.3). The magnitude of this separation is governed by the cohesion of the material until the cohesive strength of the fractured element is zero; thereafter, the phantom nodes and the original nodes move independently.

Fig. 4.3. Principle of phantom nodes method.



The criterion for fracture propagation is defined as the cohesive fracture energy (G_F), which is numerically equal to the area under the stress versus separation curve (Fig. 4.2b), as in Eq. 4.4. In quasibrittle fracture materials, the fracture propagation behavior is frequently described using a triangular model (linear involution).

$$G_F = \int_0^{\delta^f} \sigma(\delta) d\delta = \frac{1}{2} \sigma^i \delta^f \quad (4.4)$$

where δ^f is the final displacement of the fractured element.

Fracture propagation is achieved through the degradation (or damage) process. Based on the concepts of damage mechanics, which are characterized by the damage variable (D_e) (Eq. 4.5), the stiffness of the element is progressively reduced, thereby affecting the stresses on the element (Fig. 4.2b) (PEERLINGS et al., 2001).

$$D_e = \frac{\delta^f(\delta - \delta^i)}{\delta(\delta^f - \delta^i)} \quad (4.5)$$

where δ^i is the displacement at the initiation of the fracture and δ is the displacement at the time of analysis.

In the fourth phase, the stiffness and stresses in the element reach zero, and the element ruptures, generating a real fracture (Fig. 4.2b).

4.2.2 GEOMETRY, MESH AND TYPE OF ANALYSIS

An axisymmetric numerical POT model was created with the geometry, load, and boundary conditions presented in Fig. 4.4a. The mesh was created with bilinear axisymmetric quadrilateral 4-node elements, and the enriched part was created at the base of the partial core (the location of probable fracturing), as shown in Fig. 4.4b. The analysis was static.

4.3 MECHANICAL PROPERTIES OF MATERIALS

Andesite (basic mineralogical composition: plagioclase, pyroxene, chlorite and quartz) was chosen as the material model to represent homogeneous rocks because POT experimental data were reported by CACCIARI; FUTAI (2018). The mechanical properties of the disc, adhesive and andesite are shown in Table 4.1. The properties with an asterisk (*) were determined in this work and are described in detail below.

The elastic modulus (E) of the andesite was obtained through the DTT in accordance with the ASTM D 2936–95 (1995). A DL-10000™ universal machine (maximum load of 100 kN), manufactured by Emic SA (São José dos Pinhais, Brazil), was used at a constant loading rate of 0.04 MPa/s with a clip-gauge displacement meter. The TSs were attached to the metal discs and strained by a swivel joint stem. Three TSs were tested (their geometric parameters are shown in Table 4.2), and the value of E was obtained through the stress versus strain

curves of the DTT (Fig. 4.5) in the range from 3.0 to 6.0 MPa (approximately linear), resulting in an average of 78.14 GPa (Table 2).

Fig. 4.4. a) Geometry (in centimeters), load and boundary conditions and b) mesh of the POT.

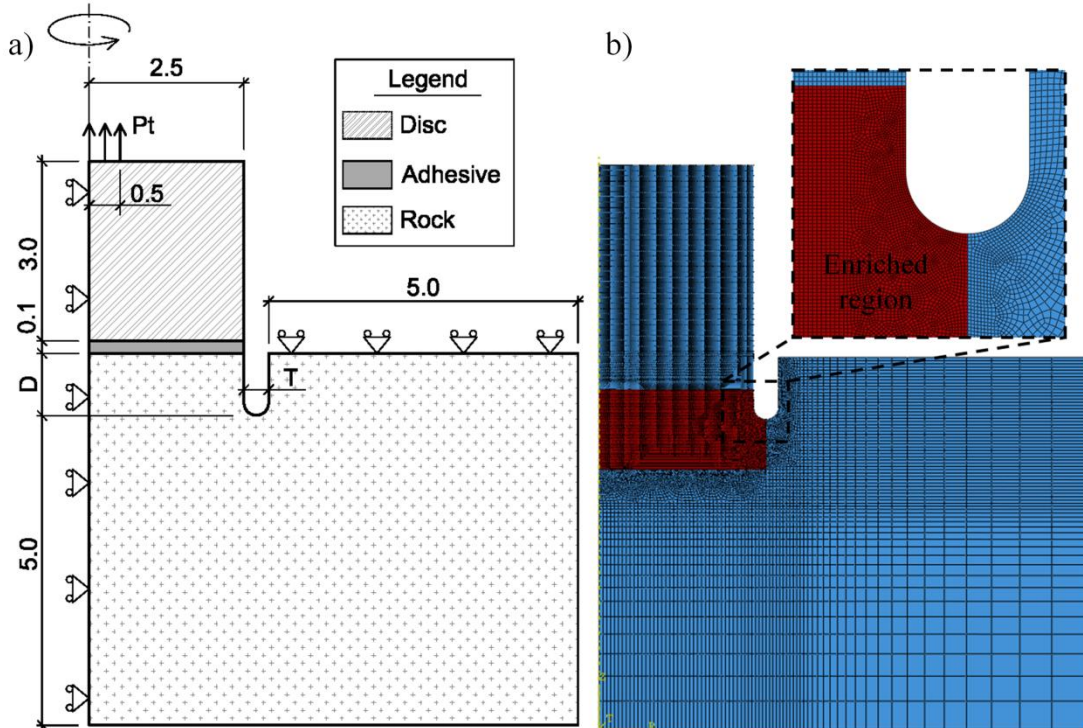


Table 4.1. Mechanical properties of materials

Materials	Elastic mechanical properties		Fracture mechanical properties	
	Elastic modulus (E) (GPa)	Poisson's ratio (ν)	Fracture initiation stress (σ^i) (MPa)	Cohesive fracture energy (G_F) (Pa.m)
Epoxy adhesive - Araldite® AV138™ (HUNTSMAN, 2004)	4.70	0.30	-	-
Metal disc - steel 304 (HIBBELER, 2012)	193.00	0.27	-	-
Rock - andesite	*	0.26 ^I	13.91 ^{II}	*

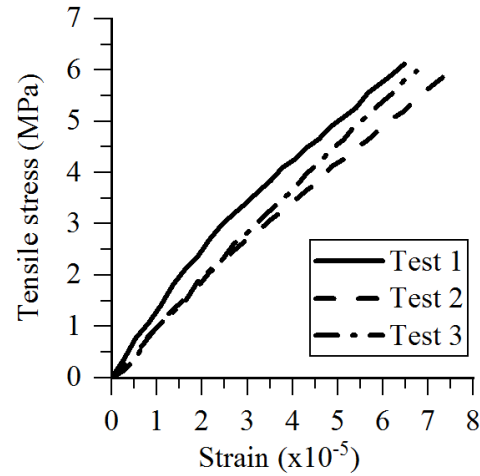
^I Average Poisson's ratio obtained by SCHULTZ (1995) for different basalts.

^{II} Average tensile strength obtained by DTT in CACCIARI; FUTAI (2018).

Table 4.2. Geometrical parameters and results of the elastic modulus tests

Test	Geometrical parameters		Results
	H (cm)	D (cm)	
1	10.62	4.93	77.34
2	10.60	4.93	73.32
3	10.61	4.93	83.75
Average:			78.14

Fig. 4.5. Stress versus strain curve of the DTT.



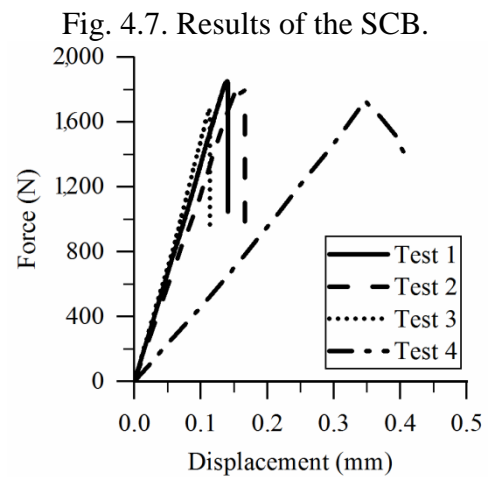
The G_F was obtained through the semicircular bend (SCB) test proposed by CHONG; KURUPPU (1984) and suggested by the International Society of Rock Mechanics and Rock Engineering (ISRM) (KURUPPU et al., 2014). Four TSs were performed in the following steps: the TSs were cut into discs with a radius of r and a thickness of t ; the discs were cut in half; the notches were made with a length of a ; a linear variable differential transformer was attached at the lower end of the notch with metal sheets to obtain the fracture opening; and the TSs were positioned on their support at a distance of s . Fig. 4.6a shows the geometric variables of the TS, and Table 4.3 contains the values of these variables. Fig. 4.6b shows one TS as an example. The compressive force (F) was applied with a 5569TM universal machine (maximum load of 50 kN), manufactured by Instron SA (São José dos Pinhais, Brazil), at a constant displacement rate of 0.06 mm/min. Fig. 4.7 shows the force versus displacement curves of the SCB tests, and Table 4.3 shows the rupture forces (F_{rup}) obtained through those tests. Based on the obtained F_{rup} values and knowing the tensile strength, elastic modulus and Poisson's ratio of the andesite, the G_F was determined using numerical back analysis. Four SCB numerical models related to the tests were generated, as shown in Fig. 4.6c. The numerical method, the fracture criteria, the element types and the type of analysis were the same as those used in the numerical POT model. The G_F results for each test are shown in Table 4.3, resulting in an average of 70.67 Pa.m.

Fig. 4.6. a) Geometry; b) experimental specimen and c) numerical model of the SCB (plane stress).



Table 4.3. Geometrical parameters and SCB test results

Tests	Geometrical parameters					Results	
	r (cm)	t (cm)	a (cm)	d (cm)	s (cm)	F_{rup} (kN)	G_F (Pa.m)
1	5.00	2.43	2.90	0.20	8.00	1.73	92.80
2	5.00	2.37	2.80	0.20	8.00	1.83	90.40
3	5.00	2.33	2.70	0.20	8.00	1.68	53.65
4	5.00	2.33	2.50	0.20	8.00	1.85	45.84
Average:						70.67	



4.4 GEOMETRICAL PARAMETRIC STUDY

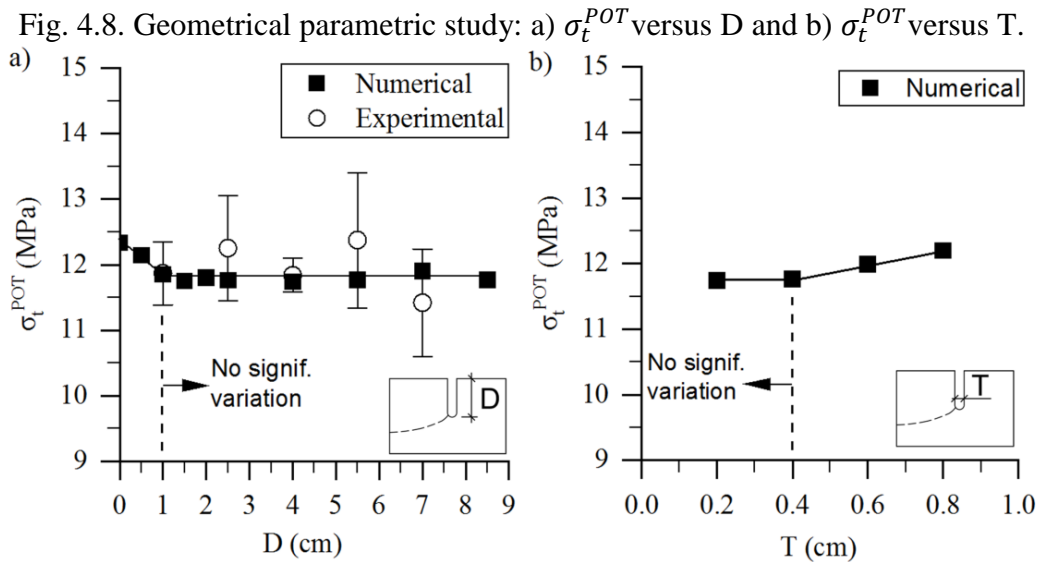
To analyze the POT fracture mechanism under different test conditions, a geometrical parametric study was conducted by varying the depth (D) and width (T) of the partial core (see Fig. 4.4a), and the models are shown in Table 4.4. Depth is a test variable because it depends on the site conditions for drilling, and width is associated with the initial thickness and wear of the circular drill bit used to make the partial core. Model A represents the conditions of a surface POT. The mechanical properties of the materials were used in the models.

Table 4.4. Models of the geometrical parametric study

Models	A	B	C	D	E	F	G	H	I	J	K	L	M
D (cm)	0.0	0.5	1.0	1.5	2.0	2.5	4.0	5.5	7.0	8.5	2.5	2.5	2.5
T (cm)	0.0	0.4	0.4	0.4	0.4	0.4	0.4	0.4	0.4	0.4	0.2	0.6	0.8

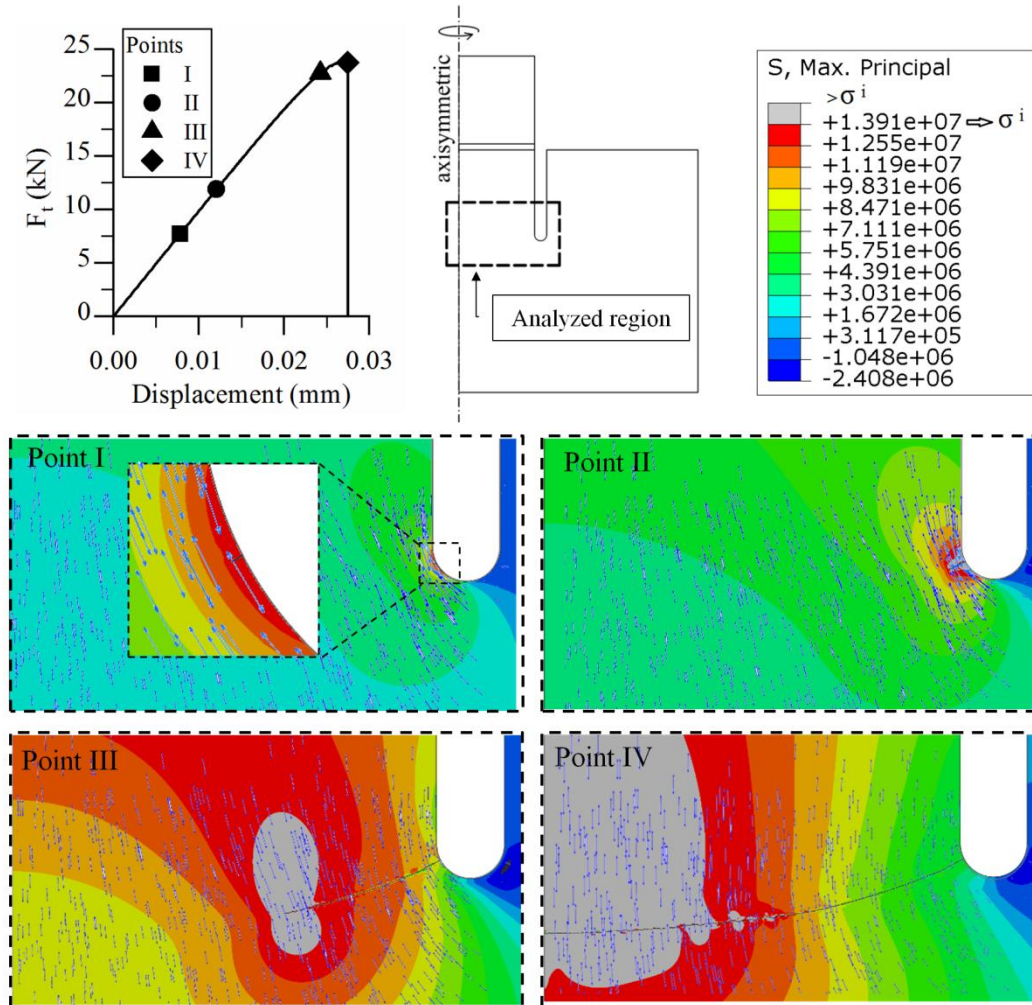
Fig. 4.8a shows the σ_t^{POT} values at different partial core depths, and a comparison is made with the experimental data from CACCIARI; FUTAI (2018). Note that σ_t^{POT} varies until $D = 1.0$ cm, and after this value, there is no significant variation. These results agree with the experimental data, indicating the good representativeness of the numerical model, but

the results differ somewhat from those of BUNGEY; MADANDOUST (1992), who observed no variation beyond 2.0 cm. Fig. 4.8b shows the σ_t^{POT} values for different partial core widths. Note the decreasing variation in σ_t^{POT} between $T = 0.80$ and 0.40 cm and no significant variation between $T = 0.40$ and 0.20 cm.



Upon analyzing the fracturing process of each model, the same mechanism of fracture initiation and propagation was observed in all of them. Fig. 4.9 shows a typical result (model F of Table 4.4) of the POT fracture mechanism (the force versus displacement curve and the maximum principal stresses on the rock). The fracture initiated at approximately $1/3$ of the rupture force (F_{rup}) at the base of the partial core in the direction orthogonal to the maximum principal tensile stress (point I in Fig. 4.9). At $1/2$ of F_{rup} (point II in Fig. 4.9), the fracture propagation was stable. Thereafter, the fracture propagation became unstable, reaching point III (Fig. 4.9). At this point, the TS ruptured (point IV in Fig. 4.9), forming a concave fracture shape.

Fig. 4.9. Typical POT fracture mechanism (axisymmetric view).

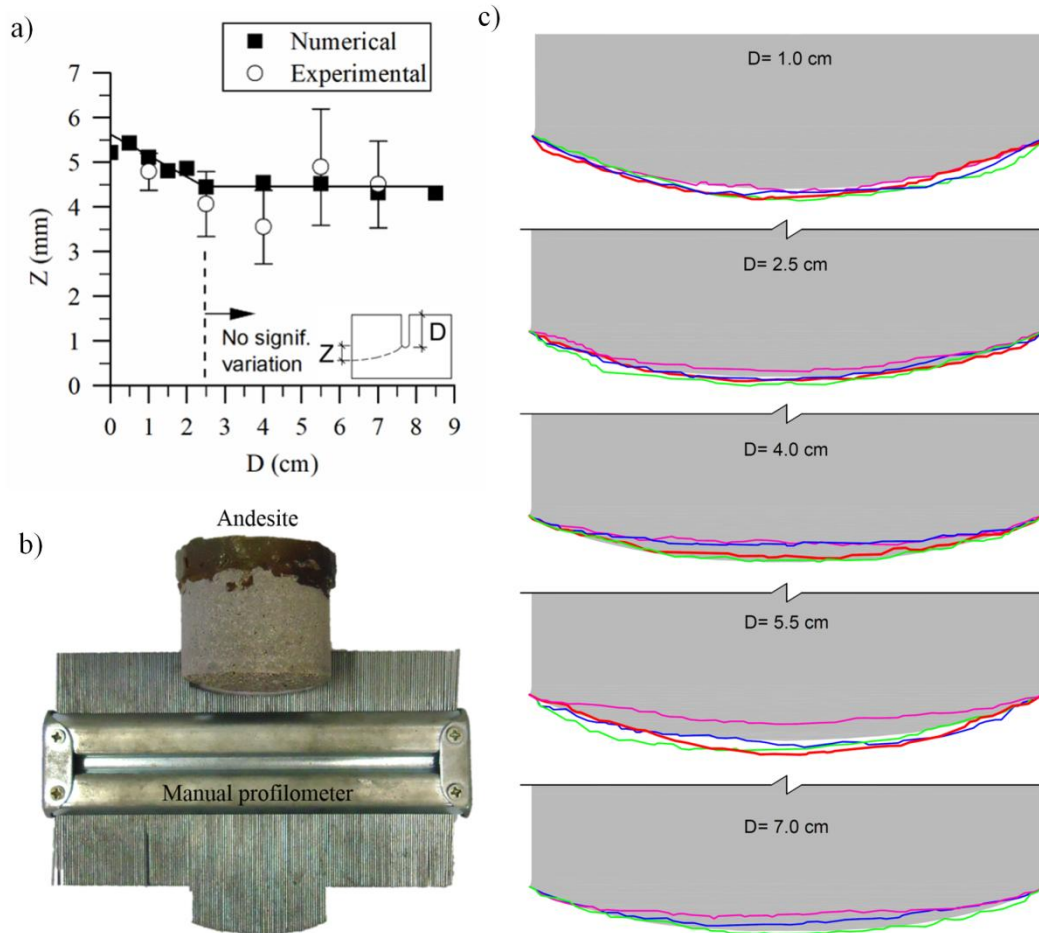


The concave fractures occurring in models A through J (Table 4.4) exhibited the same shape and appearance but differed in depth (Z). The numerical and experimental variations in Z with core depths (D) are presented in Fig. 4.10a. The experimental concave shape was obtained through a manual roughness profilometer (Fig. 4.10b) at different values of D , with four tests for each depth. Fig. 4.10c shows a visual comparison of the numerical results (gray shading) with the experimental results (lines).

Note that Z decreases as D increases up to 2.5 cm, beyond which Z assumes a constant value. The fractures obtained numerically have a fracture pattern that is very similar to the experimental fractures at the different depths, thereby highlighting the excellent representativeness of the numerical model. The concave shape of the fractures in the POT can be explained by the theory of the numerical method (XFEM-CZM) and the fracture initiation criterion used. Due to the existence of the partial core and the application of the force to the center of the TS, the tensile stresses at the base of the partial core are not vertical; rather, they are inclined (see point I in Fig. 4.9). The direction of fracture initiation is created

perpendicular to these inclined tensile stresses, forming a concave shape. The tendency of Z to decrease until $D = 2.5$ cm is due to the spreading of stresses (due to the force applied at the center of the TS) with the depth, causing the tensile stress to become less inclined and consequently reducing Z .

Fig. 4.10. a) Numerical and experimental variations in Z with D , b) manual roughness profilometer and c) visual comparison between the numerical and experimental POT fracture patterns.



4.5 MECHANICAL PROPERTIES PARAMETRIC STUDY

The POT is inherently accompanied by boundary condition problems, and thus, the tensile strength of the TS with a rupture at its base must be corrected. Assuming that the DTT is an ideal test method without boundary condition problems, the tensile strength of rock obtained in the DTT is considered correct, and the fracture initiation stress (σ^i) is considered equal to the tensile strength obtained in the DTT (σ_t^{DTT}). Accordingly, a parametric study was carried out on the mechanical properties by varying the values of σ^i , G_F and E to obtain a relationship between σ_t^{POT} and σ_t^{DTT} . Table 4.5 shows the mechanical properties used in this

study. The range of usual E values for rocks was used. The G_F is taken to be equal to the mode I fracture energy (G_{Ic}), which was calculated using Eq. 4.6, as proposed by Griffith (1920), and the mode I fracture toughness (K_{Ic}) is calculated based on E using Eq. 4.7, as proposed by WHITTAKER; SINGH; SUN (1992) for application in rocks. Different combinations of the values of G_F and σ^i were generated, resulting in 324 numerical models. The geometry of the numerical model used in this parametric study is relative to model F in Table 4.4, because, as observed previously, there is no significant variation in σ_t^{POT} for $D = 2.5$ cm and $T = 0.4$ cm.

Table 4.5. Mechanical properties of the parametric study

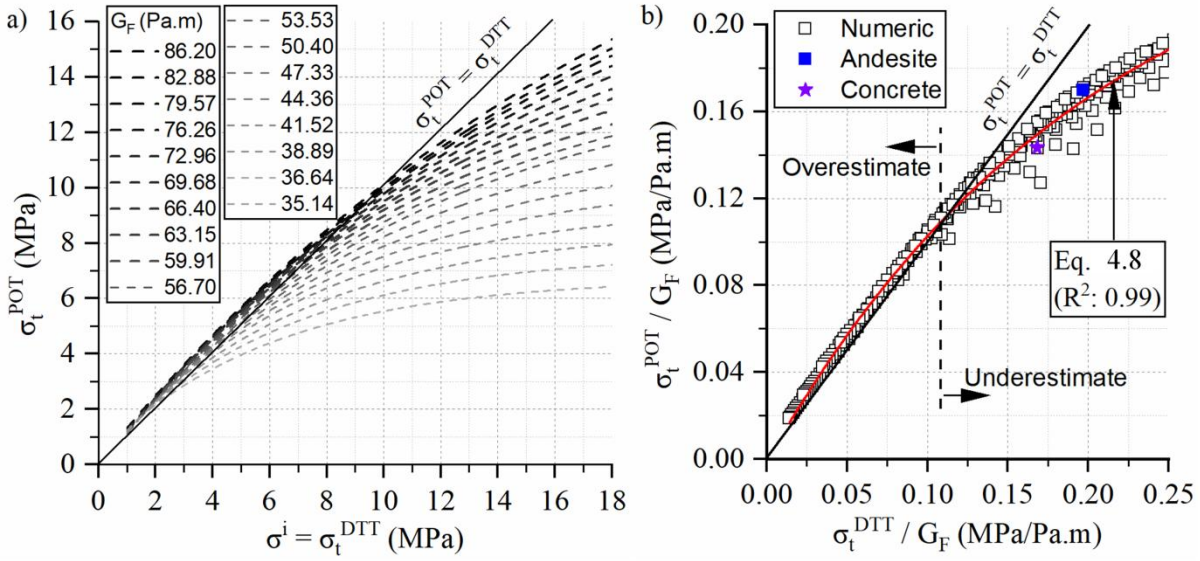
E (GPa)	K_{Ic} (MPa.m ^{0.5})	G_F (Pa.m)	σ^i (MPa)	E (GPa)	K_{Ic} (MPa.m ^{0.5})	G_F (Pa.m)	σ^i (MPa)
15.00	0.73	35.14	1.00	60.00	1.90	59.91	10.00
20.00	0.86	36.64	2.00	65.00	2.03	63.15	11.00
25.00	0.99	38.89	3.00	70.00	2.16	66.40	12.00
30.00	1.12	41.52	4.00	75.00	2.29	69.68	13.00
35.00	1.25	44.36	5.00	80.00	2.42	72.96	14.00
40.00	1.38	47.33	6.00	85.00	2.55	76.26	15.00
45.00	1.51	50.40	7.00	90.00	2.68	79.57	16.00
50.00	1.64	53.53	8.00	95.00	2.81	82.88	17.00
55.00	1.77	56.70	9.00	100.00	2.94	86.20	18.00

$$G_{Ic} = \frac{K_{Ic}^2}{E} \quad (4.6)$$

$$K_{Ic} = 0.336 + 0.026 E \quad (4.7)$$

Fig. 4.11a shows the variations in σ_t^{POT} with the mechanical properties. The relationship between σ_t^{POT} and σ_t^{DTT} is a function of G_F . By normalizing the values of σ_t^{POT} and σ_t^{DTT} with G_F (Fig. 4.11b), a relationship between the POT and the DTT is proposed through Eq. 4.8. Note that the POT can overestimate or underestimate the tensile strength, depending on G_F . Only two materials are available in the literature to verify Eq. 4.8: one is andesite, and the other is the concrete tested by COURARD et al. (2014), where: $\sigma_t^{POT} = 3.13$ MPa and $\sigma_t^{DTT} = 3.67$ MPa. The G_F value for this concrete was estimated from the Bascoul G_{Ic} data (SHAH; SWARTZ; OUYANG, 1995), based on the concrete properties described by the author, at the average value of 21.82 Pa.m. The andesite and concrete results are plotted in Fig. 4.11b, thereby demonstrating good agreement with Eq. 4.8. Thus, the tensile strength of homogeneous rocks and concrete can be obtained using Eq. 4.8 by correcting σ_t^{POT} to the $\sigma_t^{POT}(\text{corrected})$ for the range of values of $\sigma_t^{POT}(\text{corrected}) / G_F \leq 0.25$.

Fig. 4.11. a) Relationship between σ_t^{POT} and σ_t^{DTT} as a function of G_F and b) σ_t^{POT} and σ_t^{DTT} normalized with G_F .



$$\sigma_t^{POT}(\text{corrected}) = \sigma_t^{DTT} = -\frac{G_F}{4.86} \cdot \ln \left| \frac{-\frac{\sigma_t^{POT}}{G_F} + 0.269}{0.270} \right| \quad (4.8)$$

where σ_t^{POT} and $\sigma_t^{POT}(\text{corrected})$ are in MPa and G_F is in Pa.m.

4.6 PRACTICAL EXAMPLE

A practical example for correcting σ_t^{POT} was performed on three other rocks: sandstone, fine-grained granite and mylonite (rocks shown in Fig. 4.1). Table 4.6 shows the average σ_t^{POT} values obtained experimentally. G_F is taken to be equal to G_{Ic} , which was calculated using Eq. 4.6, and K_{Ic} is calculated using Eq. 4.7, based on the E value estimated for each specific rock. The corrected σ_t^{POT} value is calculated using Eq. 4.8, and the results are also presented in Table 4.6. For all cases, including the case of andesite and concrete already presented in Fig. 4.11b, the $\sigma_t^{POT}(\text{corrected})$ was superior to the σ_t^{POT} ; that is, the POT underestimated the tensile strength. When the POT underestimates the tensile strength and the adopted G_F value is based on rough estimates (i.e., it is not confirmed by specific laboratory tests), it is not prudent to consider the correction. If the POT overestimates the tensile strength, it is prudent to consider the correction, even if G_F is obtained by estimates.

Table 4.6. POT tensile strength correction for rocks

Rocks	σ_t^{POT} (MPa)	E (GPa)	K_{Ic} (MPa.m ^{0.5})	G_F (Pa.m)	σ_t^{POT} (corrected) (MPa)	σ_t^{POT} (corrected) / $G_F \leq 0.25$
Sandstone	6.67	15.00	0.73	35.14	8.87	0.25 (ok)
Fine-grained granite	9.60	50.00	1.64	53.53	12.14	0.23 (ok)
Mylonite	12.30	85.00	2.55	76.26	14.42	0.21 (ok)

4.7 CONCLUSIONS

It was possible to analyze the POT fracture mechanism under different test conditions and to identify the factors influencing the tensile strength. The numerical results were consistent with the experimental data and led to the following conclusions and recommendations:

- a) the fracture initiates at the base of the partial core and propagates in the direction orthogonal to the maximum principal tensile stress, and the concave shape of the fracture is caused by the inclination of the maximum tensile stress;
- b) σ_t^{POT} and Z decrease as D increases up to approximately 1.0 cm and 2.5 cm, respectively, and then assume practically constant values. Therefore, it is recommended to perform the POT with $D > 2.5$ cm;
- c) there is no variation in σ_t^{POT} between $T = 0.4$ cm and $T = 0.2$ cm; thus, it is recommended to use a drill bit with a thickness of approximately 0.4 cm so that its wear will not influence σ_t^{POT} ;
- d) the POT can overestimate or underestimate the tensile strength of the rock, depending on G_F ; therefore, a correction using Eq. 4.8 is recommended. The correction may increasingly be used as more G_F data for rocks are available in the literature.

The POT is a practical alternative for estimating tensile strength, especially in the field, and this study proposed an ideal geometry and a tensile strength correction equation for visually homogeneous rocks and concrete.

5 MODE I FRACTURE TOUGHNESS DETERMINATION OF ROCK AND CONCRETE VIA PULL-OFF TEST

Abstract: The Pull-Off Test (POT) was proposed as a new method for determining K_{Ic} of rock and concrete. POT can be performed in the laboratory, but its great advantage is the possibility of in field execution. This study was carried out by numerical analysis and it allowed concluding that the POT is suitable for K_{Ic} testing, since mode I prevails in the test, and an equation was proposed for determining K_{Ic} . A practical example of the method application was provided and K_{Ic} was determined for some visually homogeneous rocks. A similar result was achieved between POT and Semi-Circular Bend test.

Keywords: Mode I fracture toughness. Pull-Off Test. Rock. Concrete.

5.1 INTRODUCTION

Rock and concrete are brittle or quasibrittle materials that almost always show fractures (SHAH; SWARTZ, 1989). These fractures may have been generated in the formation process or developed during the material life by mechanical, thermal and chemical actions (WHITTAKER; SINGH; SUN, 1992). Fracture Mechanics is a versatile tool that provides a quantitative treatment based on the applied mechanics and the macroscopic properties of materials, usually relating stress analysis and fractures strength (IRWIN; WIT, 1983).

The Linear Elastic Fracture Mechanics (LEFM) is usually applied to predict the fracture propagation in brittle materials. The stress, strain and displacement are calculated at the fracture tip and the unique parameter that characterizes the magnitude of the fracture tip stress field is the stress intensity factor (SIF) (GRIFFITH, 1920; IRWIN, 1958). SIF is separated in three particular modes of loading at the fracture tip: I (tensile), II (shear-sliding) and III (shear-tearing), which are identified as K_I , K_{II} and K_{III} . Fracture toughness is the critical SIF in a particular mode (K_{Ic} , K_{IIc} and K_{IIIc}), representing the fracture resistance of the material. It depends on the material type, geometry, displacement constraints and external load applications. When SIF reaches the fracture toughness of the material, fracture propagates unstably (ATKINSON, 1987).

Mode I fractures have been widely investigated due to their greater occurrence and simplicity when compared to the other fracture modes. There are many test methods proposed in the literature for determining K_{Ic} of rock and concrete. Most of them are for laboratory application and there are only two test methods for in situ application: the Burst Test Method and the Indentation Method (WHITTAKER; SINGH; SUN, 1992).

A promising method for determining tensile strength of the materials is the Pull-Off Test (POT). POT is widely used in concrete (BUNGEY; MADANDOUST, 1992; COURARD et al., 2014), building material interfaces (AUSTIN; ROBINS; PAN, 1995; BONALDO; BARROS; LOURENÇO, 2005; RAMOS et al., 2012; CUI et al., 2016; SZEMEREY-KISS; TÖRÖK, 2017) and it was recently introduced into rock mechanics (WENG et al., 2018; CACCIARI; FUTAI, 2018; VIZINI; CACCIARI; FUTAI, 2020). Although it can be performed in the laboratory, its great advantage is the possibility of in field execution.

POT execution is easy: i) a partial core (notch) is created using a circular drill bit; ii) a metal disk is attached to the top of the sample with epoxy adhesive; iii) the pull-off tester is positioned and the tensile force is applied until rupture (Fig. 5.1a and 5.1b).

In homogeneous rock and concrete, most surface fractures occur at the base of the partial core (due to tensile stress concentration) (BUNGEY; MADANDOUST, 1992) with a concave shape (due to the inclination of the maximum tensile stresses) (VIZINI; CACCIARI; FUTAI, 2020). Fine-grained materials present fractures with more pronounced concave shape and coarse-grained materials present fractures with irregular and more planar shape (Fig. 1c). In a few cases, however, the fracture occurs near or away from the base of the partial core, due to the possible existence of invisible fractures, heterogeneities or weakness plans (CACCIARI; FUTAI, 2018).

In this research, the POT is proposed as a new method for determining K_{Ic} of visually homogeneous rock and concrete, where its great advantage is the possibility of in field execution. As could be seen in VIZINI; CACCIARI; FUTAI (2020), the POT has a heterogeneous stress state, causing fracture initiation and propagation in the test, which is suitable for K_{Ic} determination.

This study used numerical method for computing SIFs of the POT. The structure and overview of the paper is as follows (Fig. 5.2): i) the numerical methods and models are presented; ii) the POT geometry is analyzed to meet the literature recommendations and the LEFM requirements; iii) a fracture analysis of the POT is performed to analyze the typical SIFs and fracture pattern of the test; iv) a mechanical property parametric study is carried out to evaluate the effects of the parameters on K_{Ic} determination; v) a simple way to determine K_{Ic} via POT is proposed through an equation and vi) a practical example of the method application is provided and K_{Ic} is determined for some rocks and compared with Semi-Circular Bend test.

Fig. 5.1. Pull-off test: a) execution steps; b) geometry and materials and c) typical fracture pattern of homogeneous rock and concrete.

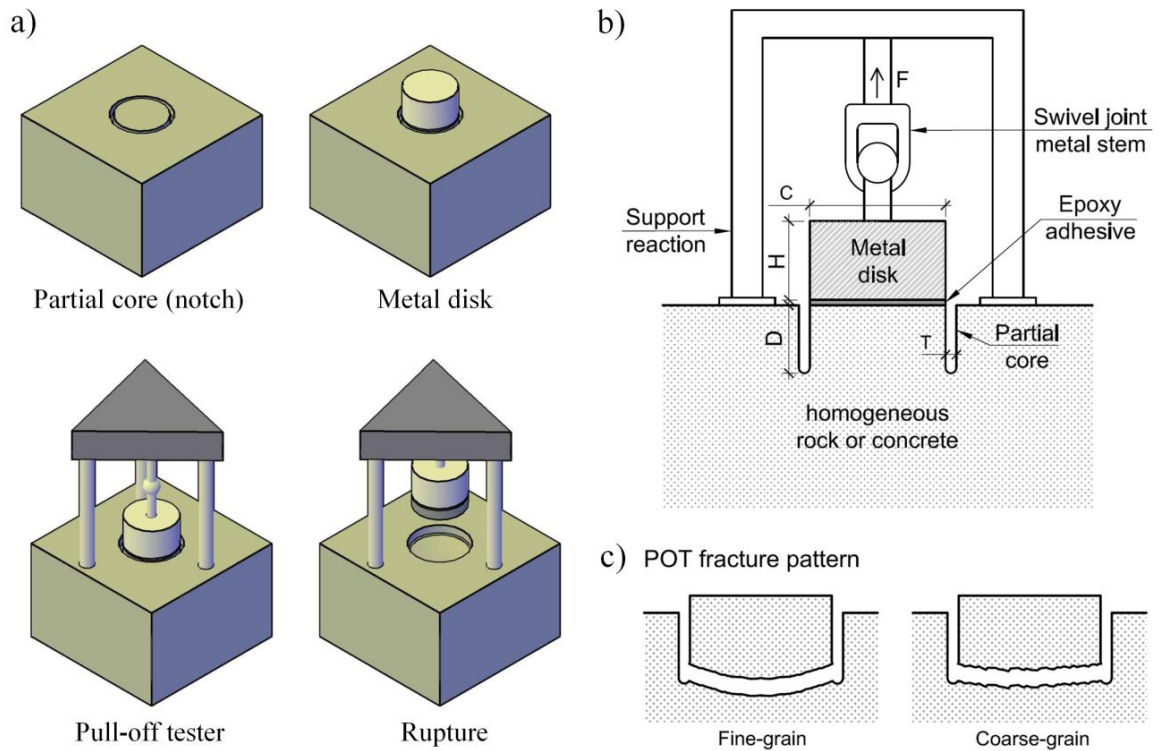
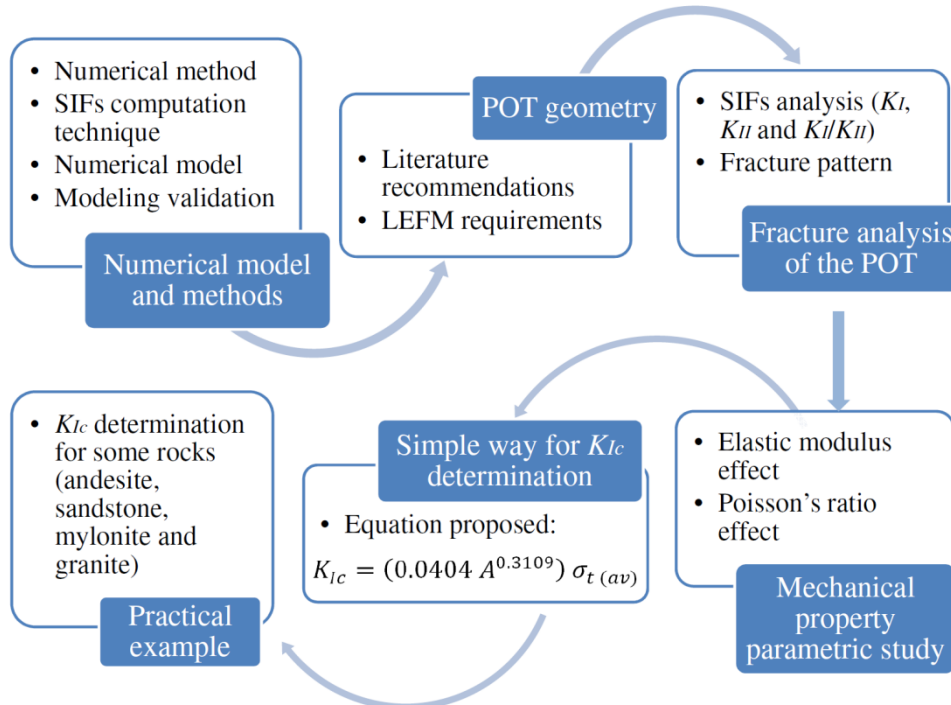


Fig. 5.2. Structure and overview of the paper.



5.2 NUMERICAL METHODS, MODEL AND SIFs COMPUTATION TECHNIQUE

The numerical methods, model and SIFs computation technique used in this research are presented in this section. A brief validation of these methods and model was performed to check our modeling.

5.2.1 NUMERICAL METHOD

The numerical analysis was performed through the Finite Element Method using the FRANC2D program, developed by the Cornell Fracture Group at Cornell University. FRANC2D uses the LEFM approach to determine the SIFs and uses the re-meshing technique to propagate the fracture.

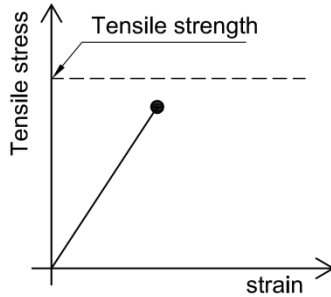
The LEFM is ideally formulated to describe the ideal brittle fracture, where the stress, strain and displacement can be uniquely characterized by SIFs (K_I in this example), as shown in Fig. 5.3a. However, it can be applied to brittle fracture (Fig. 5.3b), when the nonlinear behavior of the material is limited to a zone near to the mesofracture tip, which can be considered small compared to specimen size (often referred to as a small-scale yielding), whereby there is negligible error in ignoring any nonlinear behavior and assuming that the materials behavior is linear elastic. There is an analytical criterion in the literature to check the small-scale yielding to guarantee the validity of the LEFM for a specific material (Eq. 5.1). This equation is based on the tensile strength, mode I fracture toughness and specimen size (ATKINSON, 1987; WHITTAKER; SINGH; SUN, 1992).

$$2.7 \left(\frac{K_{Ic}}{\sigma_t} \right)^2 \leq \left\{ \begin{array}{l} D \\ C \end{array} \right. \quad (5.1)$$

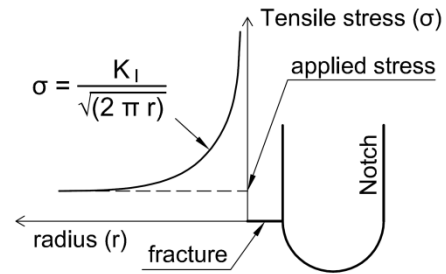
where, D is the partial core depth, C is the specimen diameter and σ_t is the tensile strength.

Fig. 5.3. Applicability of the LEFM: a) ideal brittle and b) brittle behavior. Schematic illustration of tensile stress versus strain curves of the test (POT) and tensile stress acting ahead ($\theta = 0^\circ$) the fracture tip for mode I.

a) Ideal brittle

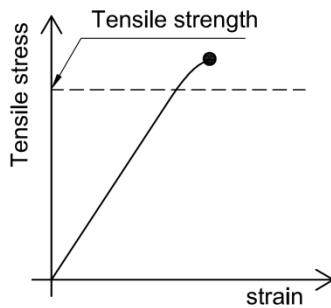


Tensile stress versus strain curve of the test

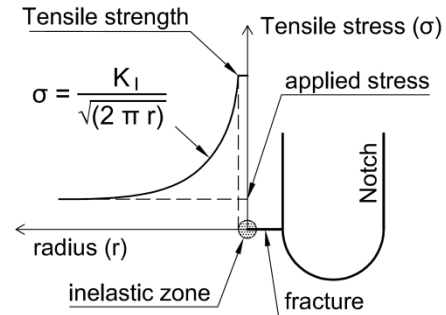


Tensile stress acting ahead of the fracture tip

b) Brittle



Tensile stress versus strain curve of the test

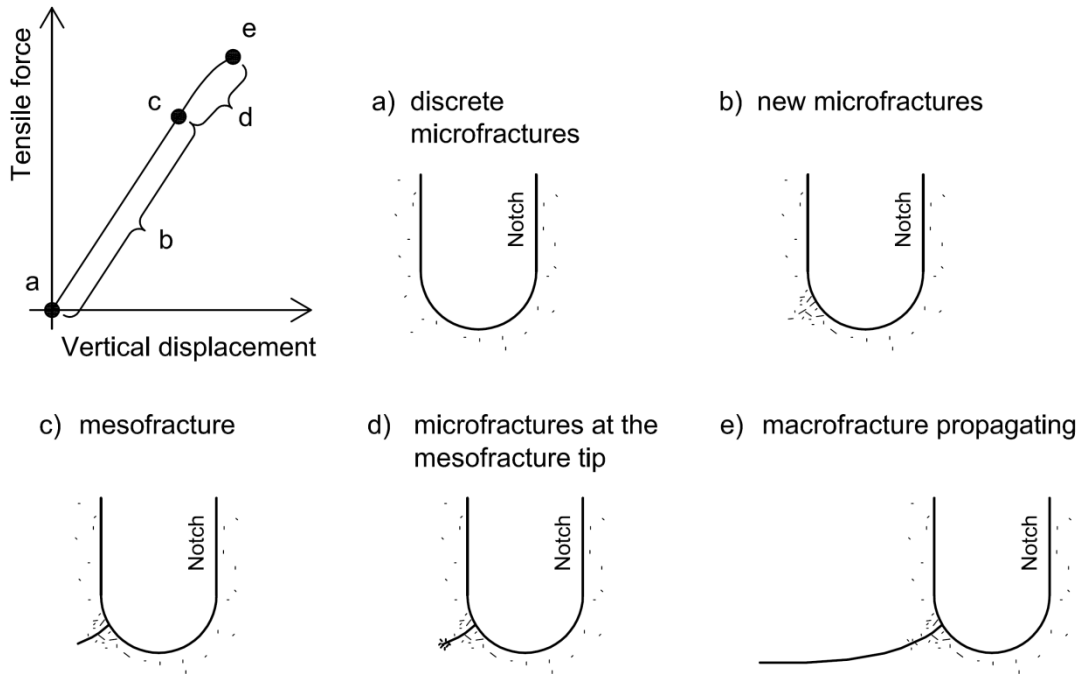


Tensile stress acting ahead of the fracture tip

The fracture formation process occurring in the POT can be inferred based on previous studies in the literature with different mode I test methods and for different rocks and concretes (HOAGLAND; HAHN; ROSENFELD, 1973; LABUZ; SHAH; DOWDING, 1987; LIN; LABUZ, 2013; MOAZZAMI; AYATOLLAHI; AKHAVAN-SAFAR, 2020; KIM et al., 2020; and others). Initially, the material contains discrete microfractures (about 10^{-6} m), naturally formed or caused by the notch cutting process (Fig. 5.4a). The specimen is loaded and new microfractures are formed, starting the fracture process zone (FPZ) (Fig. 5.4b). At a high load level, reaching the materials strength, microfractures extend and link to the other adjacent microfractures, forming a mesofracture (about 10^{-3} m) (Fig. 5.4c). The LEFM can be applied at this stage, when there is a stable mesofracture formed and the SIFs can be computed. Increasing the load, new microfractures are formed at the mesofracture tip (in a very small region), that can be ignored (Fig. 5.4d). The mesofracture is stable until the SIFs reach the fracture toughness of the material; after this, the mesofracture propagates in an unstable manner (abrupt rupture) forming a macrofracture (about 10^{-1} m) (Fig. 5.4e). The fracture toughness of the material is the SIFs computed at the moment of the transition from

the stable to the unstable condition (usually occurring at the peak of the force versus displacement curve, approximately).

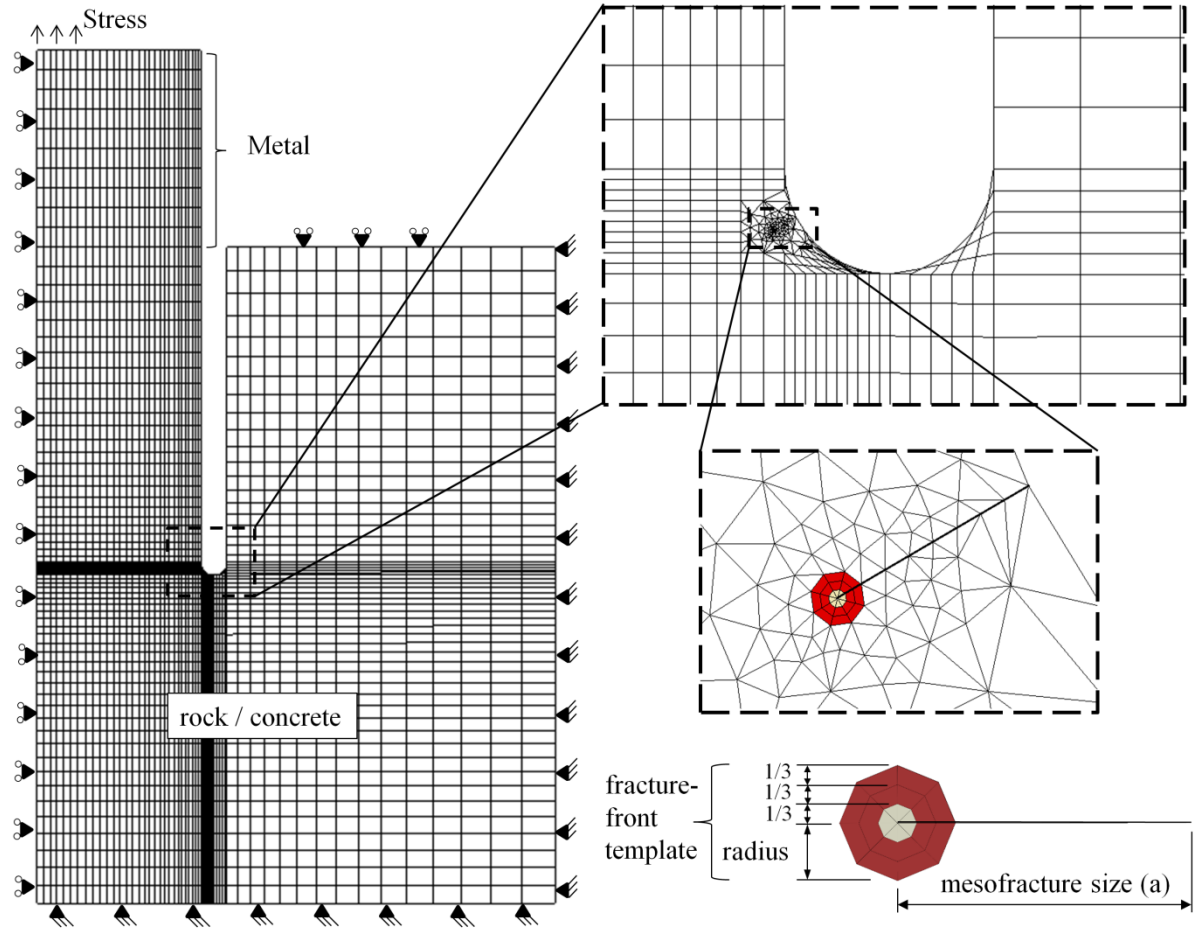
Fig. 5.4. Schematic illustration of the fracture formation process in brittle materials applied to the POT.



5.2.2 NUMERICAL MODEL

The numerical models of the POT were created with axisymmetric geometry and with the load and boundary conditions presented in Fig. 5.5. The mesh was created with bilinear axisymmetric quadrilateral 8-node and triangular 6-node elements. One mesofracture was inserted at the base of the partial core to simulate the FPZ (in this place, the maximum tensile stress concentrate and fracture occurs, as reported in several studies in the literature already mentioned). The FPZ is dependent on the geometry of the TS and the material, so it is a difficult phenomenon to predict in new tests (BROOKS, 2013; MOAZZAMI; AYATOLLAHI; AKHAVAN-SAFAR, 2020). In this study, the mesofracture size (a) was adopted consistently with the size of the model and it will be informed later. The fracture-front template radius was 10 % of the mesofracture size. The analysis was static.

Fig. 5.5. Schematic geometry, load, boundary conditions and mesh of the POT.



5.2.3 SIFs COMPUTATION TECHNIQUE

The J-integral method was chosen to compute the SIFs. The concept of the method was originally developed by ESHELBY (1956) and applied to Fracture Mechanics by RICE (1968). The approach identifies a line integral which has the same value for all integration paths (Γ_1 , Γ_2 , and any other) surrounding a class of fracture tip in two-dimensional deformation fields of linear or nonlinear elastic materials (Fig. 5.6). The J-integral is defined by:

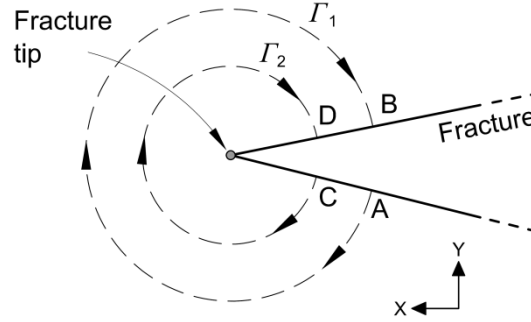
$$J = \int_{\Gamma_\epsilon}^\epsilon \left(W d_y - T \frac{\partial u}{\partial x} d_s \right) \quad (5.2)$$

and

$$W = W(x, y) = \int_0^\epsilon \sigma_{ij} d_{\epsilon ij} \quad (5.3)$$

where ε is the strain, W is the strain-energy density, σ_{ij} is all stress, $d_{\varepsilon ij}$ is the infinitesimal strain tensor, $T = \sigma_{ij} n_j$ is the traction vector defined according to the outward normal along Γ , u is the displacement vector and d_s is an element of arc length along Γ .

Fig. 5.6. J-integral contours (paths) around a fracture tip.



In an elastic material, with a monotonic load applied, J is equivalent to the energy release rate (G), proposed by IRWIN (1958), based on the GRIFFITH (1920) studies, and the SIFs for each mode can be obtained by the relationship:

$$K_I = \sqrt{G_I E^*} \quad (5.4)$$

$$K_{II} = \sqrt{G_{II} E^*} \quad (5.5)$$

where $E^* = E$ for plane stress and $E^* = E/(1-\nu^2)$ for plane strain. E is the elastic modulus and ν is the Poisson's ratio.

The kink angle of fracture propagation follows the direction orthogonal to the maximum principal tensile stress.

5.2.4 VALIDATION OF THE NUMERICAL MODEL AND METHODS

In order to validate the modeling made in this research, some numerical models of the Semi-Circular Bend Test (CHONG; KURUPPU, 1984; KURUPPU et al., 2014), with is the experimental test method recommended by the International Society of Rock Mechanics and Rock Engineering (ISRM), were modeled in FRANC2D program and the K_{Ic} obtained numerically was compared with Eq. 5.6 proposed by KARFAKIS; CHONG; KURUPPU (1986).

$$K_{Ic} = \frac{Y_I F_Q \sqrt{\pi a}}{2 r t} \quad (5.6)$$

where F_Q being the critical load (which is approximately 95 % of the rupture force), Y_I is the form factor, a is the notch length, r is the radius and t is the specimen thickness. Fig. 5.7 shows the SCB geometry and parameters.

The form factor was proposed by KURUPPU et al. (2014), Eq. 5.7. The notch length should be such that $0.4 \leq a / r \leq 0.6$ and the notch thickness (d), 1.5 mm. The minimum specimen thickness should be larger than $0.8r$ or 30 mm. The span length (S) should be $1.0 \leq S / r \leq 1.6$ (KURUPPU et al., 2014).

$$Y_I = -1.297 + 9.516 \left(\frac{S}{2r} \right) - \left[0.47 + 16.457 \left(\frac{S}{2r} \right) \right] \left(\frac{a}{r} \right) + \left[1.071 + 34.401 \left(\frac{S}{2r} \right) \right] \left(\frac{a}{r} \right)^2 \quad (5.7)$$

Fig. 5.7. SCB geometry and parameters.

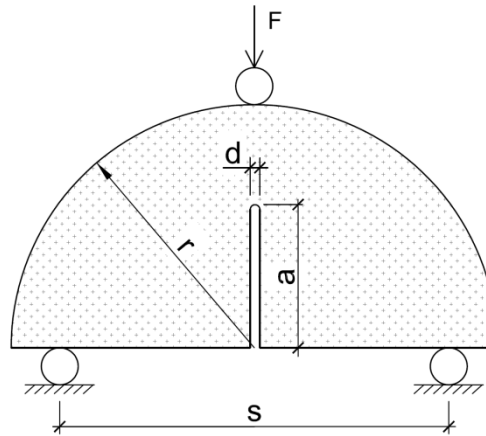


Table 1 shows the SCB models. The mechanical properties adopted were: elastic modulus (E) equal to 50 GPa and Poisson's ratio (ν) equal to 0.2. A mesofracture was inserted at the fracture tip with 1 mm. The results are shown in Table 5.1 and the relative error is calculated for each model. Note that the relative error was very small (maximum 6 %), indicating that the modeling carried out here is valid.

Table 5.1 - SCB models

Models	F_Q (kN)	a (cm)	t (cm)	S (cm)	d (cm)	r (cm)	a/r	t/r	S/r	K_{Ic} (MPa.m ^{0.5})		Relative error
										Equations 6 and 7	FRANC2D / J-integral	
1	1.0	2.5	4.5	7.0	1.5	5.0	0.5	0.9	1.4	0.35	0.35	0%
2	3.0	2.5	4.5	7.0	1.5	5.0	0.5	0.9	1.4	1.06	1.11	4%
3	5.0	2.5	4.5	7.0	1.5	5.0	0.5	0.9	1.4	1.76	1.84	5%
4	3.0	2.0	4.5	7.0	1.5	5.0	0.4	0.9	1.4	0.77	0.82	6%
5	3.0	3.0	4.5	7.0	1.5	5.0	0.6	0.9	1.4	1.48	1.50	1%
6	3.0	2.5	4.0	7.0	1.5	5.0	0.5	0.8	1.4	1.19	1.24	4%
7	3.0	2.5	5.0	7.0	1.5	5.0	0.5	1.0	1.4	0.95	1.00	5%
8	3.0	2.5	4.5	8.0	1.5	5.0	0.5	0.9	1.6	1.24	1.29	4%
9	3.0	2.5	4.5	6.0	1.5	5.0	0.5	0.9	1.2	0.87	0.92	6%

5.3 POT GEOMETRY

The geometric parameters of the POT must meet the recommendations of the specific literature of the POT and the requirements of the LEFM.

The recommendations of the literature are based on experimental and numerical studies, where the POT dimensions do not generate significant influences in the tensile strength determination. BUNGEY; MADANDOUST (1992) recommended the disc with a thickness (H) greater than 20 mm and 50 mm diameter. The standard diameter of the POT has been 50 mm, as recommended by (ASTM, 2004) and it was used in all studies published in the literature. VIZINI; CACCIARI; FUTAI (2020) recommended the partial core depth (D) greater than or equal to 2.5 cm and partial core width (T) less than or equal to 0.4 cm (Fig. 5.1b). The specimen diameter (C) and D must be checked to ensure the validity of the LEFM (Eq. 5.1). It should be noted that D must be equal or greater than C , for both to ensure the LEFM validity. Therefore, a ratio between the POT dimensions is proposed ($H / C \geq 0.4$, $D \geq C$ and $T / C \leq 0.08$) and only C must be checked.

A previous study was conducted to know the typical specimen diameters required ($C_{required}$) for the POT. Using the correlation between K_{Ic} and tensile strength (σ_t) (Eq. 5.8), proposed by WHITTAKER; SINGH; SUN (1992) for many rocks and using standard test methods, $C_{required}$ was calculated using Eq. 5.1 for some typical rock materials (Table 5.2). In this particular study, rocks with $\sigma_t \geq 10$ MPa can be tested with $C = 5$ cm (as recommended in the literature for tensile strength tests). Rocks with $\sigma_t < 10$ MPa need to be tested with large sizes. Therefore, $C_{required}$ must be evaluated before the test, estimating σ_t and K_{Ic} and checked after the test. Many rocks or concretes will need diameters larger than the conventional ($C = 5$ cm).

$$K_{Ic} = 0.27 + 0.107 \sigma_t \quad (5.8)$$

where K_{Ic} is in $\text{MPa}\cdot\text{m}^{0.5}$ and σ_t is in MPa.

Table 5.2 - Required specimen diameter for some materials

Materials	σ_t (MPa)	K_{Ic} ($\text{MPa}\cdot\text{m}^{0.5}$)	$C_{required}$ (cm)
1	2.00	0.48	15.81
2	4.00	0.70	8.22
3	6.00	0.91	6.24
4	8.00	1.13	5.35
5	10.00	1.34	4.85
6	12.00	1.55	4.53

5.4 FRACTURE ANALYSIS OF THE POT

The fractures analysis of the POT comprises a first understanding of the typical stress intensity factors, fracture pattern, stresses and displacements of the test.

Some numerical models are generated with typical stress state and mechanical properties of rock and concrete. Two sizes of the POT ($C = 5$ and 10 cm) were used, considering the dimensions ratio proposed in the previous section (Table 5.3). The mesofracture sizes for each model are presented in Table 5.3. Three average tensile stresses at the rupture were used: $\sigma_{t(av)} = 1, 5$ and 10 MPa (calculated as the ratio between the rupture force and the cross-sectional area of the TS). The elastic properties were: $E = 50$ GPa and $\nu = 0.20$ (for rock) and $E = 193$ GPa and $\nu = 0.27$ (for metal disk).

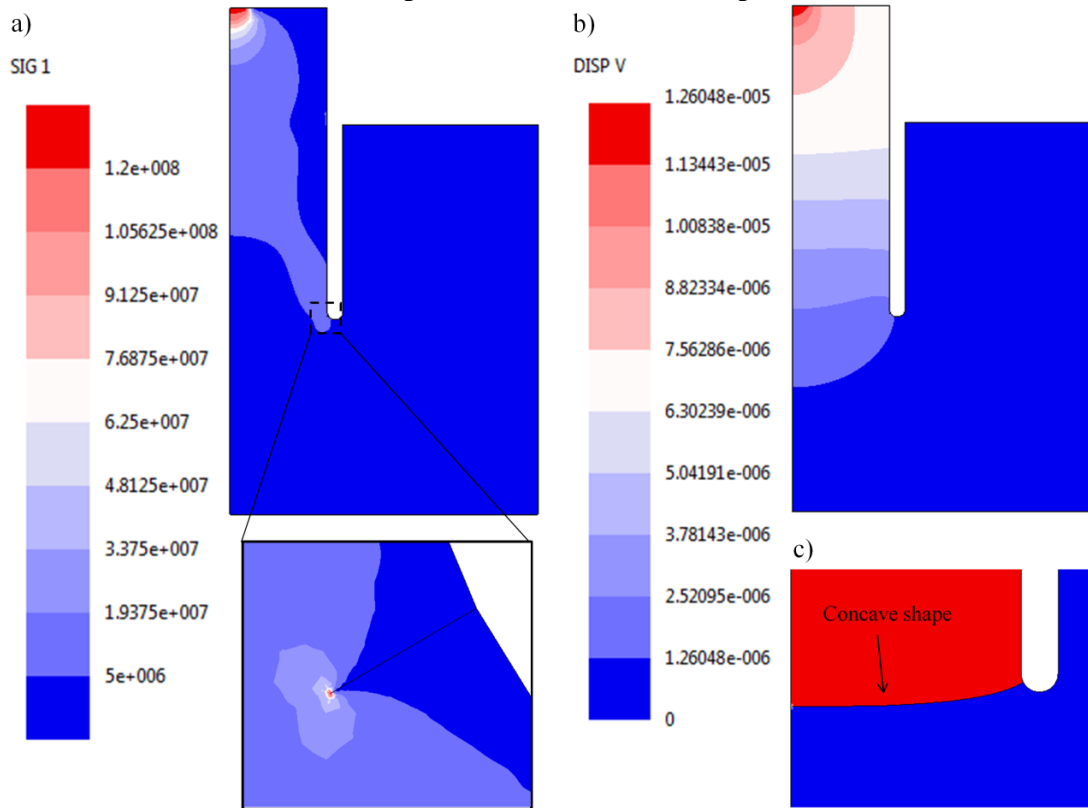
Table 5.3 - POT geometry

Models	C (cm)	H (cm)	D (cm)	T (cm)	A (cm ²)	a (mm)
1	5.0	2.5	5.0	0.4	19.6	1.0
2	10.0	5.0	10.0	0.8	78.5	2.0

The maximum principal tensile stress, vertical displacement and fracture pattern of the models are shown in Fig. 5.8 ($C = 5$ cm) and Fig. 9 ($C = 10$ cm) for $\sigma_{t(av)} = 5$ MPa (for example). The models show the same stresses, but the vertical displacement for $C = 10$ cm was twice as that for $C = 5$ cm. This difference between displacements is due to the difference between the specimen sizes. The fracture pattern of the models was the same observed in experimental tests (concave shape), as it is known in the literature.

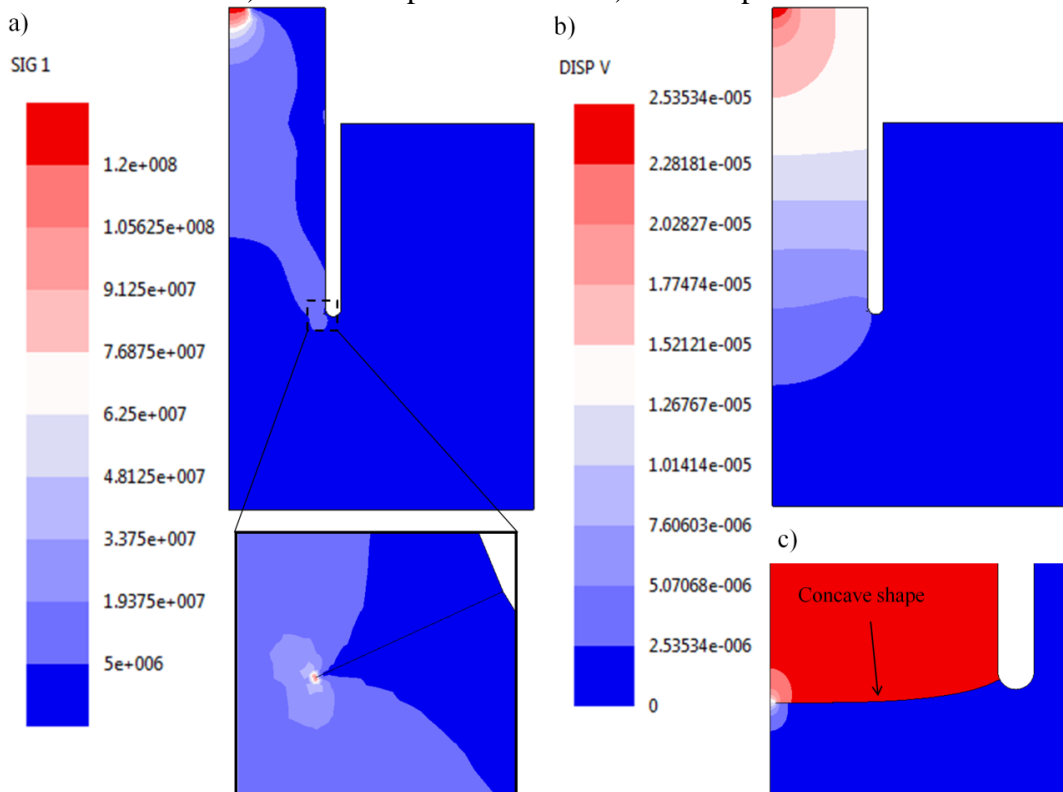
The SIFs results of all models are shown in Table 5.4. Comparing K_I with K_{II} , it can be seen that K_I was greater than K_{II} , being 17 times greater for $C = 5$ cm and 118 times for $C = 10$ cm; therefore, mode I prevails in the test, and the POT is suitable for K_{Ic} test. Comparing K_I obtained with the two POT sizes, it can be seen that K_{Ic} for $C = 10$ cm was greater than for $C = 5$ cm (1.6 times). This happens because the same $\sigma_{t(av)}$ was applied for both sizes and $C = 10$ cm presents greater displacement at the base of the partial core, resulting in a larger K_I . It does not mean that larger POT sizes result in larger K_{Ic} . LEFM assumes that, in both sizes, the failure occurs at the same K_{Ic} value and $\sigma_{t(av)}$ which is inversely proportional to the square root of the TS size (BAŽANT, 2000).

Fig. 5.8. POT results for $C = 5$ cm and $\sigma_{t(av)} = 5$ MPa: a) maximum principal tensile stress; b) vertical displacement and c) fracture pattern.



Obs.: positive signs refer to tensile or displacement up.

Fig. 5.9. POT results for $C = 10$ cm and $\sigma_{t(av)} = 5$ MPa: a) maximum principal tensile stress; b) vertical displacement and c) fracture pattern.



Obs.: positive signs refer to tensile or displacement up.

Table 5.4 - Typical SIFs of the POT

C (cm)	$\sigma_{t(av)}$ (MPa)	K_I (MPa.m ^{0.5})	K_{II} (MPa.m ^{0.5})	K_I/K_{II}
	1	0.098	0.006	17.30
5	5	0.492	0.028	17.35
	10	0.983	0.057	17.37
	1	0.159	0.001	118.46
10	5	0.792	0.007	118.40
	10	1.585	0.013	118.37

5.5 MECHANICAL PROPERTY PARAMETRIC STUDY

The elastic properties of the material (E and ν) may generate significant influence on K_{Ic} determination via POT, thus, a mechanical property parametric study was carried out. It was used one size of POT ($C = 5$ cm) and the $\sigma_{t(av)} = 5$ MPa. Table 5.5 shows the variables considered and the results. In this particular study, there is no influence of the elastic modulus and there is a little influence of Poisson's ratio. For this reason, mechanical properties were not considered in the next study for K_{Ic} determination via POT.

Table 5.5 - Mechanical property parametric study

Studies	E (GPa)	ν	K_{Ic} (MPa.m ^{0.5})
Elastic modulus effect	10	0.20	0.491
	30	0.20	0.491
	50	0.20	0.492
	70	0.20	0.492
	90	0.20	0.492
Poisson's ratio effect	50	0.10	0.477
	50	0.15	0.485
	50	0.20	0.492
	50	0.25	0.498
	50	0.30	0.505

5.6 A SIMPLE WAY FOR K_{Ic} DETERMINATION VIA POT

In this section, a simple way was proposed for determining K_{Ic} of homogeneous rock and concrete through an equation based on numerical analysis.

To encompass typical rupture stresses and mechanical properties of rock and concrete, some variables were selected. Five average tensile stresses at the rupture were used ($\sigma_{t(av)} = 1, 5, 10, 15$ and 20 MPa) and four POT sizes (using the dimensions ratio proposed) were adopted (Table 5.6). The elastic properties of the material were considered equal to $E =$

50 GPa and $\nu = 0.20$. A combination was made with these variables and the results are shown in Fig. 5.10a.

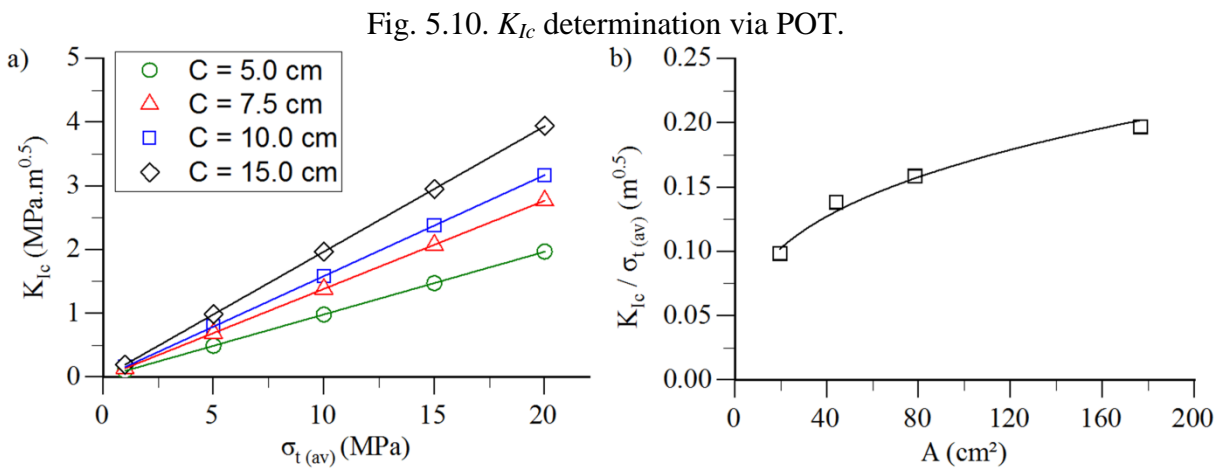
The results showed that K_{Ic} varies linearly with $\sigma_{t(av)}$ and with different proportions for each POT size. Plotting $K_{Ic} / \sigma_{t(av)}$ in function of the cross-sectional area (A) (Fig. 5.10b), a power function represents very well the interpolation. $K_{Ic} / \sigma_{t(av)}$ is constant for each C , for this reason only 4 points appear on the graph. Eq. 5.9 ($R^2 = 0.98$) is proposed for determining K_{Ic} of rocks and concretes via POT. The equation is valid only for $C = 5$ to 15 cm.

Table 5.6 - POT geometry

Models	C (cm)	H (cm)	D (cm)	T (cm)	A (cm ²)	a (mm)
1	5.0	2.5	5.0	0.4	19.6	1.0
2	7.5	3.8	7.5	0.6	44.2	1.5
3	10.0	5.0	10.0	0.8	78.5	2.0
4	15.0	7.5	15.0	1.2	176.7	3.0

$$K_{Ic} = (0.0404 A^{0.3109}) \sigma_{t(av)} \tag{5.9}$$

where K_{Ic} is in MPa.m^{0.5}, $\sigma_{t(av)}$ is in MPa and A is in cm².



5.7 PRACTICAL EXAMPLE

Two practical examples were provided to exemplify the application of the method.

The first example was a hypothetical case of basalt K_{Ic} determination via POT. The elastic modulus was adopted through the literature and the mode I fracture toughness and tensile strength were estimated through Eq. 5.10 and 5.8 (respectively), proposed by WHITTAKER; SINGH; SUN (1992). The $C_{required}$ was determined by Eq. 5.1 based on these

estimated parameters (Table 5.7). The specimen diameter was adopted ($C_{adopted}$) (a larger diameter than required and considering the circular saw cut available and the Pull-off tester). The POT was performed with $C = 7.5$ cm and the other dimensions follow the proposed ratio ($H / C \geq 0.4$, $D \geq C$ and $T / C \leq 0.08$). The average tensile stress at the rupture was obtained in the test and the cross-sectional area of the TS. The average tensile stress at the rupture was obtained in the test and, using Eq. 5.9, mode I fracture toughness of the basalt was calculated (Table 5.7).

$$K_{Ic} = 0.336 + 0.026 E \quad (5.10)$$

where K_{Ic} is in $\text{MPa}\cdot\text{m}^{0.5}$ and E is in GPa.

Table 5.7 - Example of K_{Ic} determination via POT

Material	Estimation				Test			
	E (GPa)	σ_t (MPa)	K_{Ic} ($\text{MPa}\cdot\text{m}^{0.5}$)	$C_{required}$ (cm)	$C_{adopted}$ (cm)	A (cm^2)	$\sigma_t(av)$ (MPa)	K_{Ic} ($\text{MPa}\cdot\text{m}^{0.5}$)
Basalt	50.00	12.77	1.64	4.43	7.50	44.18	10.30	1.35

The second example was an application with real data from the literature. Table 5.8 shows some homogeneous rocks and concrete, the C_{used} in the experimental test and its σ_t . The K_{Ic} was estimated for each material by Eq. 5.8 (proposed by WHITTAKER; SINGH; SUN (1992)). $C_{required}$ was determined by Eq. 1 and compared with the C_{used} in the tests. Only the C_{used} in andesite, mylonite and fine-grained granite tests were greater than the $C_{required}$. Thus, only the tests performed with these rocks met the LEFM validity criteria and had a confinable K_{Ic} value. The silicified sandstone presented a very close limit, which can be considered a valid value, since the constant 2.7 of Eq. 5.1 is an empirical and high value, in comparison with other references in rocks mechanics. The other rocks and concrete should have been tested with C major in order to be used for K_{Ic} determination. Therefore, K_{Ic} was calculated by Eq. 5.9 for the andesite, silicified sandstone, mylonite and fine-grained granite, using the cross-sectional area of the TS and the average tensile stress at the rupture (Table 5.9).

Table 5.8 - Required specimen diameters for rocks and concrete

Material	C_{used} (cm)	σ_t (MPa)	K_{Ic} (MPa.m ^{0.5})	$C_{required}$ (cm)	Verification
Andesite ¹	5.00	13.91	1.76	4.31	Ok
Marble ¹	5.00	1.70	0.45	19.08	No
White granite ¹	5.00	4.92	0.80	7.08	No
Red granite ¹	5.00	6.66	0.98	5.88	No
Silicified sandstone ²	5.00	8.87	1.22	5.10	No
Mylonite ²	5.00	14.42	1.81	4.27	Ok
Fine-grained granite ²	5.00	12.14	1.57	4.51	Ok
Concrete ³	5.00	3.67	0.66	8.80	No

¹ CACCIARI; FUTAI (2018); ² VIZINI; CACCIARI; FUTAI (2020); ³ COURARD et al., (2014).

Table 5.9 - K_{Ic} determination for rocks and concrete

Material	C_{used} (cm)	A (cm ²)	$\sigma_{t(av)}$ (MPa)	K_{Ic} (MPa.m ^{0.5})
Andesite ¹	5.00	19.63	12.00	1.22
Silicified sandstone ²	5.00	19.63	6.67	0.68
Mylonite ²	5.00	19.63	12.30	1.25
Fine-grained granite ²	5.00	19.63	9.60	0.98

¹ CACCIARI; FUTAI (2018); ² VIZINI; CACCIARI; FUTAI (2020).

5.8 COMPARISON BETWEEN POT AND SCB

There are POT and SCB results for the same andesite in CACCIARI; FUTAI (2018) and VIZINI; CACCIARI; FUTAI (2020), respectively. Hence, a comparison between POT and SCB can be made in order to validate the POT and to obtain a first correlation. Table 5.10 shows the geometrical parameters and results of the SCB test. Through Eq. 5.6 and 5.7, K_{Ic} for each test was obtained, resulting in an average of 1.54 MPa.m^{0.5}. As shown in Table 5.9, K_{Ic} obtained for andesite by POT was 1.22 MPa.m^{0.5}. Therefore, K_{Ic} obtained by POT is 79 % of the SCB for the andesite tested. The result of the POT is close to the SCB and it can be considered a first validation and correlation of the method.

Table 5.10 - K_{Ic} determination of the andesite via SCB tests¹

Test	Geometric parameters					Results	
	r (cm)	t (cm)	a (cm)	d (cm)	s (cm)	F_{rup} (kN)	K_{Ic} (MPa.m ^{0.5})
1	5.00	2.43	2.90	0.20	8.00	1.73	1.64
2	5.00	2.37	2.80	0.20	8.00	1.83	1.66
3	5.00	2.33	2.70	0.20	8.00	1.68	1.45
4	5.00	2.33	2.50	0.20	8.00	1.85	1.40
Average:							1.54

¹ VIZINI; CACCIARI; FUTAI (2020).

5.9 CONCLUSION

In this research, the POT was proposed as a new method for determining K_{Ic} of visually homogeneous rock and concrete. POT can be performed in the laboratory, but its great advantage is the possibility of in field execution. POT execution is easy and replicable, being an attractive alternative to determine K_{Ic} . The main conclusions of this work are presented below:

- a) a ratio between the dimensions of the POT was proposed to meet the LEFM requirements and the literature recommendations: $H / C \geq 0.4$, $D \geq C$ and $T / C \leq 0.08$;
- b) the most suitable C must be evaluated before the test, estimating σ_t and K_{Ic} of the specific material and checked after the test. The specimen diameter of the test must be adopted with a larger diameter than required, considering the circular saw cut and the Pull-off tester available;
- c) the Pull-off tester currently available in the market is designed to apply low forces. An improvement in this technology must be developed to apply high forces;
- d) POT is suitable for K_{Ic} test, since mode I prevails in the test;
- e) an equation was proposed for determining K_{Ic} via POT, where the parameters of the equation are the average tensile stress at the rupture and the cross-sectional area of the TS. The elastic properties of the material were not considered due to their little influence on the K_{Ic} determination;
- f) two practical examples of the method application were provided. One was a hypothetical example and other was the K_{Ic} determination of andesite, silicified sandstone, mylonite and fine-grained granite, using experimental data from the literature;
- g) POT and SCB presented similar results for andesite, which indicates the first validation and correlation of the method.

This method is intended for testing visually homogeneous material with rupture at the base of the partial core and not for materials with plans of weakness or discontinuities.

6 GENERAL CONCLUSION OF THIS DISSERTATION

This research addressed two new experimental test methods for determining strength and fracture toughness of rock and concrete: Modified Direct Shear Test (MDST) and Pull-Off Test (POT). The objectives of this research were achieved and the main conclusions are scored below.

The MDST presented good results, where tensile fracture occurred only for very low normal stress and, for low normal stresses, undesirable tensile fractures did not develop and a single horizontal shear fracture propagated. The force versus displacement curve showed an approximately linear behavior with abrupt rupture and the striated surface was observed in much of the sheared area (whitish appearance). An ideal geometry of the MDST was proposed. A better shear strength test method was achieved.

A simple way for K_{IIc} determination via MDST was proposed, using peak and residual shear strength and elastic modulus of the homogeneous rock or concrete. The MDST is a promising method because mode II prevails in the test (as observed experimentally and proved numerically) and uses the direct shear. A new method was proposed.

The fracture mechanism of the POT was investigated and it was possible to understand the factors that influence the tensile strength, allowing the proposal of an ideal geometry and a correction equation for homogeneous rocks and concrete with concave fracture shape. This study contributed to the application of POT in rock mechanics and structural engineering.

A simple way for K_{Ic} determination via POT was proposed for homogeneous rock or concrete in field and laboratory application. The POT is suitable for K_{Ic} determination, because mode I prevails in the test. A geometric ratio was proposed to guarantee the LEFM requirements and literature recommendations. A new method was proposed.

REFERENCES

- ASTM. Standard Test Method for Direct Tensile Strength of Intact Rock Core Specimens. D2936-95. **ASTM International**, p. 1–2, 1995.
- ASTM. Standard Test Method for Tensile Strength of Concrete Surfaces and the Bond Strength or Tensile Strength of Concrete Repair and Overlay Materials by Direct Tension (Pull-off Method). C1583-04. **ASTM International**, p. 1–5, 2004.
- ASTM. Standard Test Method for Performing Laboratory Direct Shear Strength Tests of Rock Specimens Under Constant Normal Force. ASTM D5607-16. **ASTM International**, p. 1–9, 2016.
- ATKINSON, B. K. **Fracture Mechanics of Rocks**. 2. ed. London: Academic Press Geology Series, 1987.
- ATKINSON, B. K.; MEREDITH, P. G. Experimental Fracture Mechanics Data for Rocks and Minerals. In: ATKINSON, B. K. (Ed.). **Fracture Mechanics of Rocks**. 2. ed. London: Academic Press Geology Series, 1987. 1p. 477–525.
- AUSTIN, S.; ROBINS, P.; PAN, Y. Tensile bond testing of concrete repairs. **Materials and Structures**, v. 28, p. 249–259, 1995.
- BACKERS, T. Fracture Toughness Determination and Micromechanics of Rock Under Mode I and Mode II Loading. n. August, 2004.
- BACKERS, T. et al. New data on mode ii fracture toughness of rock from the punch- through shear test. In: SINOROCK2004 Symposium, 3, **Anais...**2004.
- BACKERS, T.; STEPHANSSON, O. ISRM suggested method for the determination of mode II fracture toughness. **Rock Mechanics and Rock Engineering**, v. 45, n. 6, p. 1011–1022, 2012.
- BACKERS, T.; STEPHANSSON, O.; RYBACKI, E. Rock fracture toughness testing in Mode II—punch-through shear test. **International Journal of Rock Mechanics and Mining Sciences**, v. 39, n. 6, p. 755–769, 2002.
- BARENBLATT, G. I. The formation of equilibrium cracks during brittle fracture. General ideas and hypotheses. Axially-symmetric cracks. **Journal of Applied Mathematics and Mechanics**, v. 23, n. 3, p. 622–636, 1959. Disponível em: <<http://linkinghub.elsevier.com/retrieve/pii/0021892859901571>>.
- BARENBLATT, G. I. The Mathematical Theory of Equilibrium Cracks in Brittle Fracture. **Advances in Applied Mechanics**, v. 7, p. 55–129, 1962. Disponível em: <<http://www.sciencedirect.com/science/article/pii/S0065215600800058>>.
- BAŽANT, Z. P. Size effect. **Solids and Structures**, v. 37, p. 69–80, 2000.
- BAŽANT, Z. P.; PFEIFFER, P. A. Shear fracture tests of concrete. **Materials and Structures**, v. 19, n. 2, p. 111–121, 1986.
- BELYTSCHKO, T.; BLACK, T. Elastic Crack Growth in Finite Elements With Minimal Remeshing. **International Journal for Numerical Methods in Engineering**, v. 45, n. 5, p. 601–620, 1999.

- BEWICK, R. P. et al. DEM simulation of direct shear: 1. Rupture under constant normal stress boundary conditions. **Rock Mechanics and Rock Engineering**, v. 47, n. 5, p. 1647–1671, 2014.
- BOBET, A. et al. Numerical Models in Discontinuous Media: Review of Advances for Rock Mechanics Applications. **Journal of Geotechnical and Geoenvironmental Engineering**, v. 135, n. 11, p. 1547–1561, 2009.
- BOBET, A.; EINSTEIN, H. H. Fracture coalescence in rock-type materials under uniaxial and biaxial compression. **International Journal of Rock Mechanics and Mining Sciences**, v. 35, n. 7, p. 863–888, 1998.
- BONALDO, E.; BARROS, J. A. O.; LOURENÇO, P. B. Bond characterization between concrete substrate and repairing SFRC using pull-off testing. **International Journal of Adhesion and Adhesives**, v. 25, n. 6, p. 463–474, 2005.
- BROBERG, B. **Cracks and fracture**. Cambridge: Academic Press, 1999.
- BROOKS, Z. **Fracture Process Zone: Microstructure and Nanomechanics in Quasi-Brittle Materials**. 2013. University of Southern California and Massachusetts Institute of Technology, 2013.
- BUNGEY, J. H.; MADANDOUST, R. Factor influencing pull-off tests on concrete. **Magazine of Concrete Research**, v. 44, n. 158, p. 21–30, 1992.
- CACCIARI, P. P.; FUTAI, M. M. Assessing the tensile strength of rocks and geological discontinuities via pull-off tests. **International Journal of Rock Mechanics and Mining Sciences**, v. 105, n. 380, p. 44–52, 2018.
- CHO, N.; MARTIN, C. D.; SEGO, D. C. Development of a shear zone in brittle rock subjected to direct shear. **International Journal of Rock Mechanics and Mining Sciences**, v. 45, n. 8, p. 1335–1346, 2008.
- CHONG, K. P.; KURUPPU, M. D. New specimen for fracture toughness determination for rock and other materials. **International Journal of Fracture**, v. 26, n. 2, p. 59–62, 1984.
- COURARD, L. et al. Effect of Misalignment on Pull-off Test Results: Numerical and Experimental Assessments. **ACI Materials Journal**, v. 111, n. 2, p. 153–162, 2014.
- CRESSWELL, A. W.; BARTON, M. E. Direct shear tests on an uncemented, and a very slightly cemented, locked sand. **Quarterly Journal of Engineering Geology and Hydrogeology**, v. 36, n. 2, p. 119–132, 2003.
- CUI, S. et al. Experimental study on bond performance between shotcrete and rock in a hot and humid tunnel environment. **KSCE Journal of Civil Engineering**, v. 20, n. 4, p. 1385–1391, 2016.
- DEB, D.; GUJJALA, Y. K. Extended finite element procedures for analysis of bolt crossing multiple intersecting rock joints. **International Journal of Rock Mechanics and Mining Sciences**, v. 107, p. 249–260, 2018. Disponível em: <<https://doi.org/10.1016/j.ijrmms.2018.04.052>>.

- DIEDERICHS, M. S.; KAISER, P. K. Tensile strength and abutment relaxation as failure control mechanisms in underground excavations. **International Journal of Rock Mechancics and Mining Sciences**, v. 36, p. 69–96, 1999.
- DIRGELIENĖ, N.; SKUODIS, Š.; GRIGUSEVIČIUS, A. Experimental and Numerical Analysis of Direct Shear Test. **Procedia Engineering**, v. 172, p. 218–225, 2017. Disponível em: <<http://dx.doi.org/10.1016/j.proeng.2017.02.052>>.
- DUGDALE, D. S. Yielding of steel sheets containing clits. **Journal of the Mechanics and Physics of Solids**, n. 8, p. 100–104, 1960.
- ELICES, M. et al. The cohesive zone model: advantages, limitations and challenges. **Engineering Fracture Mechanics**, v. 69, n. 2, p. 137–163, 2002.
- ENGELDER, T. Joints and Shear Fractures in Rocks. In: ATKINSON, B. K. (Ed.). **Fracture Mechanics of Rock**. 2. ed. London: Academic Press Geology Series, 1987. 1p. 27–69.
- ESHELBY, J. D. The Continuum Theory of Lattice Defects. **Solid State Physics**, v. 3, p. 79–144, 1956.
- FERESTADE, I.; HOSSEINI TEHRANI, P.; HEIDARY, R. Fracture toughness estimation of ballast stone used in Iranian railway. **Journal of Rock Mechanics and Geotechnical Engineering**, v. 9, n. 5, p. 892–899, 2017. Disponível em: <<https://doi.org/10.1016/j.jrmge.2017.03.017>>.
- FRACTURE ANALYSIS INC. FRANC3D Theory Manual. p. 51, 2015.
- FU, J. et al. Cracking Performance of an Operational Tunnel Lining Due to Local Construction Defects. **International Journal of Geomechanics**, v. 19, n. 4, p. 13, 2019.
- GONG, F. et al. Evaluation of Shear Strength Parameters of Rocks by Preset Angle Shear, Direct Shear and Triaxial Compression Tests. **Rock Mechanics and Rock Engineering**, v. 53, n. 5, p. 2505–2519, 2020. Disponível em: <<https://doi.org/10.1007/s00603-020-02050-1>>.
- GRIFFITH, A. A. The Phenomena of Rupture and Flow in Solids. **Philosophical Transactions of the Royal Society of London**, n. A 221, p. 163–198, 1920.
- HIBBELER, R. **Engineering Mechanics Statics**. Twelfth Ed ed. Upper Saddle River: Pearson Education, Inc., 2012.
- HOAGLAND, R. G.; HAHN, G. T.; ROSENFELD, A. R. Influence of microstructure on fracture propagation in rock. **Rock Mechanics by Springer-Verlag**, v. 5, n. 2, p. 77–106, 1973.
- HOBBS, D. W. The tensile strength of Rocks. **International Journal of Rock Mechanics and Mining Sciences & Geomechanics Abstracts**, v. 1, p. 385–396, 1964. Disponível em: <<http://www.sciencedirect.com/science/article/pii/0009250968890517>>.
- INGLIS, C. E. Stresses in a plate due to the presnce of cracks and sharp corners. **Trans. Inst. Naval Arch.**, v. 55, p. 219–239, 1913.
- IRWIN, G. R. Elasticity and Plasticity. In: FLUGGE, S. (Ed.). **Handbuch der Physik**. Berlim: Springer, 1958. p. 551–590.

- IRWIN, G.; WIT, R. de. A Summary of Fracture Mechanics Concepts. v. 1, n. 1, p. 240, 1983.
- ISRM. Suggested methods for determining the strength of rock materials in triaxial compression: Revised version. **International Journal of Rock Mechanics and Mining Sciences & Geomechanics Abstracts**, v. 20, n. 6, p. 285–290, 1983.
- JING, L. A review of techniques, advances and outstanding issues in numerical modelling for rock mechanics and rock engineering. **International Journal of Rock Mechanics & Mining Sciences**, v. 40, p. 283–353, 2003.
- JING, L.; HUDSON, J. A. Numerical methods in rock mechanics. **International Journal of Rock Mechanics & Mining Sciences**, v. 39, p. 409–427, 2002.
- KARFAKIS, M. G.; CHONG, K. P.; KURUPPU, M. D. A Critical Review of Fracture Toughness Testing of Rocks. In: **Rock Fracture Mechanics**. Laramie: University of Wyoming, 1986.
- KIM, S. K. et al. Determining the fracture process zone length and mode I stress intensity factor in concrete structures via mechanoluminescent technology. **Sensors (Switzerland)**, v. 20, n. 5, 2020.
- KURUPPU, M. D. et al. ISRM-Suggested Method for Determining the Mode I Static Fracture Toughness Using Semi-Circular Bend Specimen. **Rock Mechanics and Rock Engineering**, v. 47, n. 1, p. 267–274, 2014.
- LABUZ, J. F.; SHAH, S. P.; DOWDING, C. H. The fracture process zone in granite: evidence and effect. **International Journal of Rock Mechanics and Mining Sciences and Geomechanics Abstracts**, v. 24, n. 4, p. 235–246, 1987.
- LAJTAI, E. Z. Mechanics of Second Order Faults and Tension Gashes. **Geological Society of America Bulletin**, v. 80, p. 2253–2272, 1969.
- LAQUECHE, H.; ROUSSEAU, A.; VALENTIN, G. Crack propagation under mode I and II loading in slate schist. **International Journal of Rock Mechanics and Mining Sciences and Geomechanics Abstracts**, v. 23, n. 5, p. 347–354, 1986.
- LAWN, B. **Fracture of Brittle Solids**. 2. ed. Cambridge: Cambridge University Press, 1993.
- LEE, J. S. **Time-Dependent Crack Growth in Brittle Rocks and Field Applications to Geologic Hazards**. 2007. The University of Arizona, 2007. Disponível em: <<http://web.archive.org/web/20201026154752/https://repository.arizona.edu/handle/10150/193784>>.
- LI, G.; REN, Z.; YU, J. Mixed-mode I-II fracture process zone characteristic of the four-point shearing concrete beam. **Materials**, v. 13, n. 14, 2020.
- LI, V. C. Mechanics of Shear Rupture Applied to Earthquake Zones. In: ATKINSON, B. K. (Ed.). **Fracture Mechanics of Rocks**. 2. ed. London: Academic Press Geology Series, 1987. 1p. 351–428.
- LIN, Q. et al. The influences of mode II loading on fracture process in rock using acoustic emission energy. **Engineering Fracture Mechanics**, v. 194, n. March, p. 136–144, 2018. Disponível em: <<https://doi.org/10.1016/j.engfracmech.2018.03.001>>.

- LIN, Q.; LABUZ, J. F. Fracture of sandstone characterized by digital image correlation. **International Journal of Rock Mechanics and Mining Sciences**, v. 60, p. 235–245, 2013. Disponível em: <<http://dx.doi.org/10.1016/j.ijrmms.2012.12.043>>.
- MELLENK, J. M.; BABUŠKA, I. The partition of unity finite element method: Basic theory and applications. **Computer Methods in Applied Mechanics and Engineering**, v. 139, n. 1–4, p. 289–314, 1996.
- MELIN, S. When does a crack grow under mode II conditions? **International Journal of Fracture**, v. 30, n. 2, p. 103–114, 1986.
- MOAZZAMI, M.; AYATOLLAHI, M. R.; AKHAVAN-SAFAR, A. Assessment of the fracture process zone in rocks using digital image correlation technique: The role of mode-mixity, size, geometry and material. **International Journal of Damage Mechanics**, v. 29, n. 4, p. 646–666, 2020.
- MOËS, N.; DOLBOW, J.; BELYTSCSKO, T. A finite element method for crack growth without remeshing. **International Journal for Numerical Methods in Engineering**, v. 46, n. 1, p. 131–150, 1999.
- MOHAMMADNEJAD, M. et al. An overview on advances in computational fracture mechanics of rock. **Geosystem Engineering**, p. 1–24, 2018. Disponível em: <<https://doi.org/10.1080/12269328.2018.1448006>>.
- NIKOLIĆ, M.; ROJE-BONACCI, T.; IBRAHIMBEGOVIĆ, A. Overview of the numerical methods for the modeling of rock mechanics problems. **Tehnicki Vjesnik**, v. 23, n. 2, p. 627–637, 2016.
- PEERLINGS, R. et al. Mathematical and numerical aspects of an elasticity-based local approach to fracture. **Revue Europeenne des Elements Finis**, v. 10, p. 209–226, 2001.
- PERRAS, M. A.; DIEDERICHS, M. S. A Review of the Tensile Strength of Rock: Concepts and Testing. **Geotechnical and Geological Engineering**, v. 32, n. 2, p. 525–546, 2014.
- PETIT, J. P. Criteria for the sense of movement on fault surfaces in brittle rocks. **Journal of Structural Geology**, v. 9, n. 5–6, p. 597–608, 1987.
- PETIT, J. P. Normal stress dependent rupture morphology in direct shear tests on sandstone with applications to some natural fault surface features. **International Journal of Rock Mechanics and Mining Sciences & Geomechanics Abstracts**, v. 25, n. 6, p. 411–419, 1988.
- PETROVIC, J. J. Mixed-Mode Fracture of Hot-Pressed Si₃N₄. **Journal of the American Ceramic Society**, v. 68, n. 6, p. 348–355, 1985.
- RABCZUK, T. et al. A new crack tip element for the phantom-node method with arbitrary cohesive cracks. **International Journal for Numerical Methods in Engineering**, v. 75, p. 577–599, 2008.
- RABCZUK, T. Computational Methods for Fracture in Brittle and Quasi-Brittle Solids: State-of-the-Art Review and Future Perspectives. **ISRN Applied Mathematics**, v. 2013, p. 1–38, 2013.

- RAMOS, N. M. M. et al. Reliability of the pull-off test for in situ evaluation of adhesion strength. **Construction and Building Materials**, v. 31, p. 86–93, 2012. Disponível em: <<http://dx.doi.org/10.1016/j.conbuildmat.2011.12.097>>.
- RAO, Q. H. et al. Size effect of the mode II fracture toughness of rock. In: *Rock Mechanics for Industry*, Balkema, Rotterdam. **Anais...** Balkema, Rotterdam: Rock Mechanics for Industry, 1999.
- RICE, J. R. A Path Independent Integral and the Approximate Analysis of Strain Concentration by Notches and Cracks. **Journal of Applied Mechanics**, v. 35, n. 2, p. 379–386, 1968.
- RYBICKI, E. F.; KANNINEN, M. F. A finite element calculation of stress intensity factors by a modified crack closure integral. **Engineering Fracture Mechanics**, v. 9, n. 4, p. 931–938, 1977.
- SCHULTZ, R. A. Limits on strength and deformation properties of jointed basaltic rock masses. **Rock Mechanics and Rock Engineering**, v. 28, n. 1, p. 1–15, 1995.
- SHAH, S. P.; SWARTZ, S. E. **Fracture of Concrete and Rock**. New York: Springer-Verlag, 1989.
- SHAH, S.; SWARTZ, S. E.; OUYANG, C. **Fracture mechanics of concrete: applications of fracture mechanics to concrete, rock and other quasi-brittle materials**. [s.l.: s.n.]
- SUN, G. X.; WHITTAKER, B. N.; SINGH, R. N. Use of the Brazilian disk test for determining the mixed mode I-II fracture toughness envelope of rock. In: *International conference on mechanics of jointed and faulted rock*, Vienna, Austria. **Anais...** Vienna, Austria: 1990.
- SYSTÈMES, D. Modeling discontinuities as an enriched feature using the extended finite element method. In: **Analysis User's manual**. 6.12 ed. Rhode Island: Dassault Systèmes, 2012. p. 1–26.
- SZEMEREY-KISS, B.; TÖRÖK, Á. Failure mechanisms of repair mortar stone interface assessed by pull-off strength tests. **Bulletin of Engineering Geology and the Environment**, v. 76, n. 1, p. 159–167, 2017.
- VIZINI, V. O. S.; CACCIARI, P. P.; FUTAI, M. M. Numerical assessment of factors influencing the tensile strength of rocks via pull-off test. **International Journal of Geomechanics**, v. 20, n. 7, p. 1–9, 2020.
- WANG, X. et al. Simulated Crack and Slip Plane Propagation in Soil Slopes with Embedded Discontinuities Using XFEM. **International Journal of Geomechanics**, v. 18, n. 12, p. 17, 2018.
- WENG, M.-C. et al. Measuring Foliation Tensile Strength of Metamorphic Rock by Using Pull-Off Test. **Geotechnical Testing Journal**, v. 41, n. 1, p. 132–140, 2018. Disponível em: <<http://www.astm.org/doiLink.cgi?GTJ20170078>>.
- WHITTAKER, B. N.; SINGH, R. N. .; SUN, G. **Rock fracture mechanics: principles, design and applications**. Amsterdam: Elsevier, 1992.

- WONG, R. C. K. et al. Shear strength components of concrete under direct shearing. **Cement and Concrete Research**, v. 37, n. 8, p. 1248–1256, 2007.
- WU, H.; KEMENY, J.; WU, S. Experimental and numerical investigation of the punch-through shear test for mode II fracture toughness determination in rock. **Engineering Fracture Mechanics**, v. 184, p. 59–74, 2017. Disponível em: <<https://doi.org/10.1016/j.engfracmech.2017.08.006>>.
- XIE, Y. et al. Mixed mode fracture analysis of semi-circular bend (SCB) specimen: A numerical study based on extended finite element method. **Computers and Geotechnics**, v. 82, p. 157–172, 2017. Disponível em: <<http://dx.doi.org/10.1016/j.compgeo.2016.10.012>>.
- XU, X. et al. Review of the Relationships between Crack Initiation Stress, Mode I Fracture Toughness and Tensile Strength of Geo-Materials. **International Journal of Geomechanics**, v. 18, n. 10, p. 20, 2018.
- YAO, W. et al. A dynamic punch-through shear method for determining dynamic Mode II fracture toughness of rocks. **Engineering Fracture Mechanics**, v. 176, p. 161–177, 2017. Disponível em: <<http://dx.doi.org/10.1016/j.engfracmech.2017.03.012>>.